Technische Universität München
Institut für Energietechnik

Lehrstuhl für Thermodynamik

NO_X-Formation in Reacting Premixed Jets in Hot Cross Flow

Denise Ahrens

Vollständiger Abdruck der von der Fakultät für Maschinenwesen der Technischen Universität München zur Erlangung des akademischen Grades eines

DOKTOR – INGENIEURS

genehmigten Dissertation.

Vorsitzender:
Univ.-Prof. Dr.-Ing. Harald Klein

Prüfer der Dissertation:
1. Univ.-Prof. Dr.-Ing. Thomas Sattelmayer
2. Univ.-Prof. Dr.-Ing. Franz Joos,
Universität der Bundeswehr Hamburg

Die Dissertation wurde am 18.03.2015 bei der Technischen Universität München eingereicht und durch die Fakultät für Maschinenwesen am 27.07.2015 angenommen.

Vorwort

Die hier vorliegende Arbeit entstand während meiner Tätigkeit als Wissenschaftliche Mitarbeiterin am Lehrstuhl für Thermodynamik der Technischen Universität München. Mein besonderer Dank gilt meinem Doktorvater Herrn Professor Sattelmayer, sowie Herrn Professor Joos (Universität der Bundeswehr Hamburg) für die Begutachtung meiner Arbeit. Danken möchte ich auch Herrn Professor Klein für die Übernahme des Vorsitz während der mündlichen Prüfung.

Am Lehrstuhl möchte ich den Damen Bassett, Schulz-Reichwald und Hirsch für die Hilfe und Unterstützung bei organisatorischen Fragen danken, sowie allen Mitarbeitern in den Werkstätten für die Hilfe beim Aufbau und Inbetriebnahme der Anlage.

Bei GE, Power & Water bedanke ich mich für die Finanzierung unseres Projekts, insbesondere den Herren Hasan Karim und Mark Hadley möchte ich für die fachliche, technische Unterstützung danken.

Mein besonderer Dank gehört meinen Projektkollegen Michael Kolb und Johannes Weinzierl. Ich finde wir hatten nicht nur eine sehr arbeitssame und erfolgreiche Zeit miteinander, sondern hatten auch sehr viel Spaß. Zusammen durften wir gemeinsame Höhen feiern und Tiefen überstehen. Für fachliche und freundschaftliche Gespräche sowie gemeinsames Musizieren möchte ich Herrn Oberingenieur Christoph Hirsch danken. Für das Korrekturlesen der Arbeit danke ich Vera Hoferichter und Christoph Jörg und für die Hilfe beim Einreichen der Dissertation Balbina Hampel. Für die Freundschaften und gegenseitige Hilfe am Lehrstuhl danke ich besonders der "Brotzeitgruppe", aber auch allen anderen ehemaligen Kolleginnen und Kollegen.

Zahlreiche Studenten und Studentinnen haben am erfolgreichen Gelingen des Forschungsprojekts Anteil gehabt, aus dem heraus ich dann meine Arbeit erstellen konnte. An dieser Stelle möchte ich einige studentische Arbeiten hervorheben, die unter meiner Betreuung abgeschlossen wurden, und den Beteiligten nochmals meinen Dank aussprechen (in chronologischer Reihenfolge): Peter Müller, Vera Hoferichter, Michael Baur und Michael Steinmetz.

Zum Abschluss noch der wichtigste Dank an meine Familie, die mich immer unterstützt hat auf meinem nicht immer geradlinigen Lebensweg. Meinem Mann Alexander gilt mein besonderer Dank für die psychologische Unterstützung und auch das Korrekturlesen der Arbeit.

Danke euch allen!

Berlin, im August 2015 Denise Ahrens

Zusammenfassung

Stickoxidemissionen (NO_x) verursachen sauren Regen, Smog und tragen indirekt zur globalen Erwärmung der Atmosphäre bei. Der Großteil der NO_x-Emissionen wird bei der Verbrennung von fossilen Brennstoffen freigesetzt. Aufgrund der Festsetzung strengerer gesetzlicher Grenzwerte müssen bestehende Brennkammerkonzepte grundlegend überdacht werden. Die gestufte Verbrennung mit einer konventionellen ersten Stufe, in deren heißes Abgas ein Luft-Brennstoff-Gemisch eingedüst wird, kann hierzu einen Beitrag liefern. Die hier vorliegende Arbeit untersucht, unter welchen Umständen diese Anordnung zur Stickoxidreduzierung in stationären Gasturbinen führen kann. Das Reduktionspotential wird für atmosphärischen Versuchsbedingungen und mithilfe chemischer Netzwerkmodelle für Maschinenbedingung (bei 20bar) untersucht.

Abstract

Emissions of nitrogen oxides (NO_x) are one main precursor of acid rain, smog and contribute indirectly to global warming. A large fraction of the global NO_x-emissions originate from combustion of fossil fuels. Legal compulsion to further reduce maximum NO_x-emissions force gas turbine designers to rethink state of the art combustion chamber design. In this context, axially staged combustion with conventional burners in the first stage and jets injected into the hot cross flow in the second stage is of particular interest. The study at hand contributes to the research on if and how axially staged combustion can lead to a reduction of overall NO_x-emissions in stationary gas turbines. A combined approach of experiment and chemical reactor network simulations is used to reveal the NO_x reduction potential at atmospheric and high pressure engine conditions (at 20bar).

TABLE OF CONTENTS

NOMENCLATURE

Latin Letters

A	$[m^2]$	Area
BG	[counts]	Background intensity in x-z-measurement plane
c_p	$\left[\frac{J}{kg\,K}\right]$	Mixture averaged heat capacity at constant pressure
c_{pk}	$\left[\frac{J}{kg\,K}\right]$	Heat capacity at constant pressure of the k^{th} species
c	$\left[\frac{m}{s}\right]$	Velocity magnitude in the x-z-measurement plane
D	[m]	Jet diameter
E_A	$\left[\frac{kJ}{mol}\right]$	Activation energy
f_{MP}	[-]	Mixture fraction at MP
f_{pf}	[-]	Mixture fraction at ignition
f_{ideal}	[-]	Ideal global mean mixture fraction
f'	[-]	Local temporal fluctuation of mixture fraction
f*	[-]	Instantaneous local mixture fraction in x-z-measurement plane
f	[-]	Local mean mixture fraction
h_k	$\left[\frac{J}{kg}\right]$	Specific enthalpy of the k^{th} species
h_{in}	$\left[\frac{J}{kg}\right]$	Specific enthalpy of the incoming flow
h	$\left[\frac{J}{kg}\right]$	Mixture averaged specific enthalpy

H	[m]	Channel height of the cross flow section
I_{ref}	[counts]	Actual intensity at reference point
i	[-]	Exponent
I	[counts]	Actual intensity in x-z-measurement plane
J_{cold}	[-]	Momentum ratio with the cold inlet conditions of the jet
J_{react}	[-]	Momentum ratio with the burnt jet conditions
J	[-]	Momentum ratio jet to cross flow
j	[-]	Exponent
k	[-]	k^{th} species
l_{min}	[-]	Stoichiometric molar air requirement per mole fuel, l_{min}=9.64 for natural gas [141]
$l_{turb,D}$	[m]	Turbulent macro length scale
$l_{turb,K}$	[m]	Turbulent micro (Kolmogorov) length scale
LS	[-]	Laser sheet correction matrix in x-z-measurement plane
$\dot{m}$	$\left[\frac{kg}{s}\right]$	Mass flow
$\dot{m}_{in}$	$\left[\frac{kg}{s}\right]$	Mass flow of the incoming flow
$\dot{m}_J$	$\left[\frac{kg}{s}\right]$	Jet mass flow
$\dot{m}_X$	$\left[\frac{kg}{s}\right]$	Cross flow mass flow
m_J	[kg]	Mass of the jet
M_k	$\left[\frac{kg}{mol}\right]$	Molar mass of the k^{th} species
m_X	[kg]	Mass of the cross flow
M	$\left[\frac{kg}{mol}\right]$	Mixture averaged molar mass
m	[kg]	Mass

msr	[%]	Mass split ratio of mass flow of the jet to overall mass flow
n	[-]	Reaction order
NO_x	[ppm]	NO_x-concentration normalized to 15% O_2
$NO_{x,raw}$	[ppm]	Raw NO_x-concentration
p	[bar]	Pressure
$\dot{Q}$	[W]	Rate of heat flow
$\overline{RMS_T}$	[-]	Spatial mean RMS value of temporal fluctuations
r	[-]	Blowing ratio, r=$\sqrt{J}$
RMS_c	$\left[\frac{m}{s}\right]$	RMS value of the velocity components u and w
RMS_S	[-]	RMS value of the local mixture variance
RMS_T	[-]	Local RMS value of temporal fluctuations
S_l	$\left[\frac{m}{s}\right]$	Laminar flame speed
T_J	[K]	Temperature of the jet
T_X	[K]	Temperature of the cross flow
T_{ad}	[K]	Adiabatic flame temperature
T_{in}	[K]	Preheating temperature of the air flow
T_{MP}	[K]	Temperature at MP
T	[K]	Temperature
t	[s]	Time
Tu	[-]	Turbulence intensity, RMS_c normalized by jet velocity U_J
U_S	[-]	Unmixedness due to spatial inhomogeneities
U_T	[-]	Unmixedness due to temporal inhomogeneities
$U_{J,b}$	$\left[\frac{m}{s}\right]$	Jet velocity of the burnt flow
$U_{J,u}$	$\left[\frac{m}{s}\right]$	Jet velocity of the unburnt flow

U_J	$\left[\frac{m}{s}\right]$	Jet velocity
U_X	$\left[\frac{m}{s}\right]$	Cross flow velocity
u'	$\left[\frac{m}{s}\right]$	Velocity fluctuations in x-direction
u	$\left[\frac{m}{s}\right]$	Velocity in x-direction
U	[J]	Internal energy
$v_{min,dry}$	[-]	Molar amount of dry exhaust gas per mole fuel at stoichiometric conditions, $v_{min,dry}$=8.65 for natural gas [141]
v_{min}	[-]	Molar amount of exhaust gas per mole fuel at stoichiometric conditions, v_{min}=10.66 for natural gas [141]
V_k	$\left[\frac{m}{s}\right]$	Diffusion velocity of the k^{th} species
v'	$\left[\frac{m}{s}\right]$	Velocity fluctuations in y-direction
v	$\left[\frac{m}{s}\right]$	Velocity in y-direction
V	[-]	Velocity ratio jet to cross flow
V	[m^3]	Volume
w'	$\left[\frac{m}{s}\right]$	Velocity fluctuations in z-direction
w	$\left[\frac{m}{s}\right]$	Velocity in z-direction
[X]	$\left[\frac{mol}{m^3}\right]$	Molar concentration of species X
X	[-]	Notation for a certain species
x	[m]	Coordinate in cross flow direction
Y_k	[-]	Mass fraction of the k^{th} species
$Y_{k,in}$	[-]	Mass fraction of the k^{th} species of the incoming flow
y	[m]	Coordinate over the channel width
z_f	[m]	Penetration of mixture trajectory
z_v	[m]	Penetration of velocity trajectory
z	[m]	Coordinate over the channel height

Greek Letters

α	$\left[\frac{m^2}{s}\right]$	Thermal diffusivity
$\gamma_{O_2,air}$	[%]	Oxygen volume fraction in air, $\gamma_{O_2,air}$=20.942
γ_{O_2}	[%]	Dry measured oxygen molar fraction at MP
Δ	$\left[\frac{m^2}{s}\right]$	Mass diffusivity
δ_f	[m]	Flame thickness
ϵ	$\left[\frac{m^2}{s^3}\right]$	Eddy dissipation rate
λ	$\left[\frac{W}{mK}\right]$	Thermal conductivity
ν	$\left[\frac{m^2}{s}\right]$	Kinematic viscosity
ξ	[m]	Coordinate along the jet trajectory
ϕ	[-]	(Fuel-air) equivalence ratio
ϕ_J	[-]	Equivalence ratio in the jet
ϕ_{tot}	[-]	Overall equivalence ratio of jet and cross flow
ϕ_X	[-]	Equivalence ratio in the cross flow
ϕ_{15}	[-]	Equivalence ratio at 15% O_2 standard condition, ϕ_{15}=0.306 for natural gas [141]
ϕ_{MP}	[-]	Calculated local equivalence ratio at MP
ρ	$\left[\frac{kg}{m^3}\right]$	Fluid density
$\rho_{J,b}$	$\left[\frac{kg}{m^3}\right]$	Fluid density of the burnt jet
$\rho_{J,u}$	$\left[\frac{kg}{m^3}\right]$	Fluid density of the unburnt jet
ρ_J	$\left[\frac{kg}{m^3}\right]$	Fluid density of the jet
ρ_X	$\left[\frac{kg}{m^3}\right]$	Fluid density of the cross flow
ρ_{ref}	$\left[\frac{kg}{m^3}\right]$	Fluid density at reference point

τ	[s]	Residence time
τ_{chem}	[s]	Characteristic chemical time scale, residence time in flame
τ_{ign}	[s]	Ignition delay time
$\tau_{\text{turb,D}}$	[s]	Time scale of the macro length scale
$\tau_{\text{turb,K}}$	[s]	Time scale of the micro (Kolmogorov) length scale
τ_{cc}	[-]	Total, normalized residence time in the combustor
τ_{post}	[s]	Post-flame residence time
$\dot{\omega}$	$\left[\frac{\text{mol}}{\text{m}^3\text{s}}\right]$	Molar rate of production

Dimensionless Numbers

Da_{ign}	Ignition delay Damköhler number, ratio of integral turbulent time scale to ignition delay time
Da_{t}	Turbulent Damköhler number, ratio of integral turbulent to chemical time scale
Ka	Karlovitz number, ratio of chemical time scale to turbulent micro time scale
Le	Lewis number, ratio of thermal to mass diffusivity
Pr	Prandtl number, ratio of kinematic viscosity to thermal diffusivity
Re	Reynolds number, ratio of inertial forces to viscous forces
Re_{t}	Turbulent Reynolds number
Sc	Schmidt number, ratio of kinematic viscosity to mass diffusivity

Acronyms

1DFF	One Dimensional Free Flame
CPR	Constant Pressure Reactor
CVP	Counter-Rotating Vortex Pair

DLN	Dry Low NO_x
FLOX	Flameless Oxidation
JIC	Jet in Cross Flow
LBO	Lean Blow Out
MixPIV	Mixture Particle Image Velocimetry
MP	Measurement Point
NO_x	Nitrogen Oxides NO and NO_2
OP	Operating Point
PDF	Probability Density Function
PIV	Particle Image Velocimetry
ppm	Parts per Million
RMS	Root Mean Square
RQL	Rich-Quench-Lean
RR	Reaction Rate
SCR	Selective Catalytic Reduction
TC	Thermocouple

LIST OF TABLES

LIST OF FIGURES

1 Introduction to Jets in Cross Flow in Stationary Gas Turbines

In the last decade the increasing generating capacity of volatile power from solar and wind has driven the development of fossil power plant technology towards increasing operational flexibility while maintaining low emission and high efficiency standards. To make ends meet, gas turbine designers have to find ways to increase the power turn down capacity of their engine at low NO_x-emission and to further improve overall efficiency at high power. While mass flow rate control using variable inlet guide vanes in the first compressor stages has provided a substantial extension of the operational window for lean premixed combustion, the required range still needs alternative combustion concepts. In this context, axially staged combustion with conventional premix burners in the first stage and jets injected into the hot cross flow (JIC) in the second stage is of particular interest. In this work, the NO_x reduction potential of this concept is studied with an upscaled generic test rig and simplified chemical modeling.

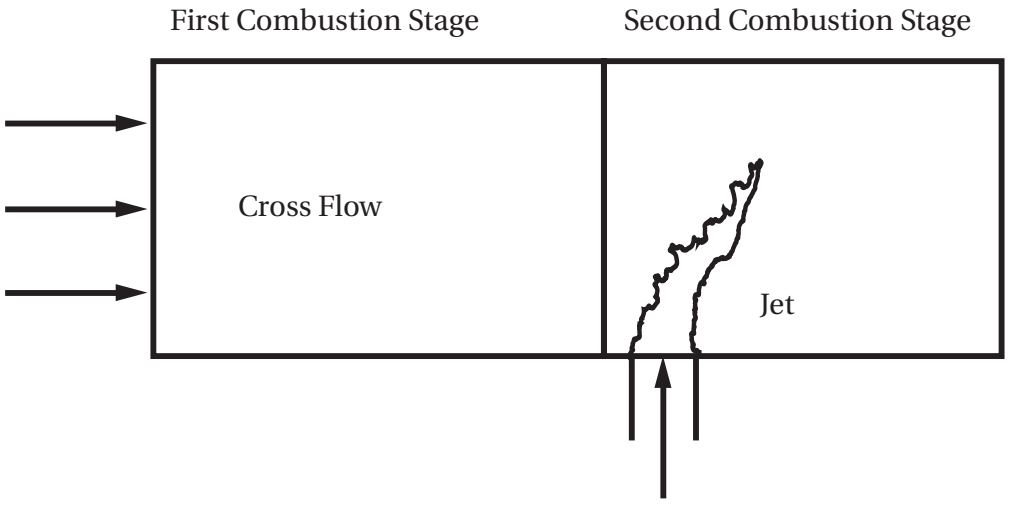

Figure 1.1: Outline of the reacting jet in hot cross flow experiment.

The outline of the reacting jet in hot cross flow experiment is shown in figure 1.1. A premixed secondary jet is injected perpendicular to the cross flow channel into the fully burnt hot exhaust gas of the first combustion zone. This configuration is theoretically promising for low NO_x-emissions and increased flexibility based on two aspects: The first stage can be fired at an optimized lean operating point for low power operation that keeps NO_x-emissions low even for the relatively long residence time of the products in the hot region. At full load the jet can be fired at slightly higher equivalence ratio than the first stage in order to increase the overall thermal efficiency. Due to the fast burnout and mixing with the colder cross flow the residence time of the jet products in hot regions is short, which results in low overall NO_x-emissions. A higher mass split ratio, i.e. a higher mass flow through the second stage, can increase those effects. Accordingly, the case with higher equivalence ratio of the second stage with respect to the first stage is most interesting for research with technical relevance. In this configuration, mixing is of crucial importance for NO_x-formation in the second stage.
In addition to the NO_x reduction potential which originates from perfectly premixed calculation, a second potentially beneficial effect is caused by the limited mixing quality of state of the art combustors and the inevitable air addition (seals, dampers, etc.) in between the combustion zone and the turbine inlet. Both effects cause a significant increase of the effective combustion temperature above the turbine inlet temperature. With axial staging, the first stage can be fired at an optimized operating point, by which NO_x-emissions are kept low. Due to the lower residence time in the second stage, the NO_x minimum is reached, if the secondary stage is fired at slightly higher equivalence ratio than the first stage. With regard to this, more realistic assumptions taking into account the limitations of currently available combustor technology must be taken into consideration. The potential benefit of staging might be higher under this conditions.
In summary, the introduction of axial staging leads to an evolution of current combustion technology, which has benefits regarding NO_x-formation in addition to the well known positive effects on part load burnout.

1.1 Low NO_x Combustion Technologies

Nitrogen Oxides (NO_x) are, beside sulphur dioxide (SO_2), the main precursor of acid rain which causes acidification of lakes, rivers or forests [95, 98]. Although NO_x is not a direct greenhouse gas, its further reaction to HNO_3 produces secondary pollutants such as particles, ozone or peroxyacetylnitrate [67], which contribute to global warming and have an impact on human health. Since pollution causes damage and costs, e.g. [93], NO_x-emissions are under strict legal regulations nowadays. A large fraction of the global NO_x-emissions originate from combustion of fossil fuel and biomass. Using natural gas as a fuel and air as an oxidizer, the only source of NO_x is due to oxidation of the N_2 in the air.
Measures to reduce NO_x-emissions in stationary gas turbines either take directly action in the combustor or further downstream as after treatment. Examples of direct reduction strategies are water or steam injection, a high degree of fuel and air premixing at a low equivalence ratio as in dry low NO_x (DLN) combustion, and parallel or serial staged combustion (as for example in rich-quench-lean burning (RQL)). An example of after treatment NO_x-reduction is the selective catalytic reduction (SCR) [124, 128].
Today, premixed lean combustion is state of the art in heavy-duty stationary gas turbines. Due to fuel and air premixing, combustion temperature peaks are avoided, which primarily contribute to the overall NO_x-emissions. In order to reach low load levels, most DLN combustors, [27, 145] (GE gas turbines) and [59, 140] (Siemens HR3 burner), use staging concepts where the fuel to groups of premixers can be switched off. To maintain stable ignition the remaining groups often need to be piloted that is typically done with non-premixed diffusion flames, because of their robustness against lean blow out (LBO) and thermoacoustic instability [86, 96].
A different approach to achieve a higher turn-down ratio with low NO_x-emissions is sequential reheat combustion used by Alstom for the GT24/GT26 gas turbines, e.g. [31, 46]. In this kind of combustor, the first lean premixed combustion stage is followed by the high pressure turbine before the partially expanded gas enters the second combustor at temperatures around 1000-1300K. In the second combustor additional fuel is injected and mixed until auto ignition occurs. Recent studies fo-

cus on the application of hydrogen blends as an alternative fuel (see for a numerical analysis e.g. [68, 120] and experimental studies on a high pressure test rig [39, 40]).
Another possibility of an axially staged combustion system is the Rich-Quench-Lean (RQL) combustor design, as used in Rolls-Royce [126, 128] and GE [36] aero gas turbines. In this combustor design, the first stage is operated at rich conditions with equivalence ratios between 1.2 and 1.6. In the adjacent mixer, the combustion products are quenched with air. The quick quenching in the combustor leads to a lean equivalence ratio of 0.5-0.7 and full burn out in the second stage. As the formation of NO_x is highly sensitive to the residence time in the hot environment between the two stages, quick mixing and dilution with air is crucial for low emissions. While RQL combustion has favorable characteristics in the context of aero application, the NO_x-levels achieved are by a factor 2-3 higher than those required for power generation with stationary gas turbines.
At high preheating temperatures, as in recuperated micro gas turbines, lean premixed combustion may not be applicable due to the risk of self ignition. Thus, alternative approaches for NO_x-reduction are used in micro gas turbines. The so-called flameless oxidation (FLOX) [152], is characterized by a high recirculation rate of exhaust gas in the combustion chamber of 30 to 50%. This fact leads to a temperature increase in the combustion process of only a few hundred Kelvin with an invisible flame. In this combustion mode, at firing temperatures in the range around 1500-1600K and high preheating temperature of up to 1200-1300K, NO_x-emissions in the single digit ppm range are achievable, as shown in [2, 18]. A successful application of flameless combustion in a multiple-staged configuration has been reported by the University of Tokyo, see [2, 4, 5, 54, 55, 153]. However, regarding the high turbine inlet temperatures required in modern stationary gas turbines for power generation this concept cannot be applied.
With state of the art combustion technologies, NO_x-emissions in the range of 10ppm can be achieved in stationary gas turbines that still is twice to three times higher compared to the theoretical minimum achievable for the given turbine inlet temperature. This is a result of unmixedness in the flame zone and air addition along the combustor length. With conventional technology a higher turbine inlet tempera-

ture is hard to achieve with NO_x-levels below 10ppm. In contrast, the staged combustion concept with a reacting premixed jet in the second stage can combine the state of the art DLN combustion with the need of a higher turbine inlet temperature without NO_x penalty.

1.2 Recent Research on Reacting Jet in Cross Flow

The potential of staged combustion for NO_x reduction has been discussed in literature [22, 132]. Although the absolute reduction potential is assumed to be small [132], decreasing NO_x-emission limits below 10ppm require staging strategies to be reconsidered. In this context, axially staged combustion with injection of a premixed jet into a hot cross flow has been proposed. This novel combustor technology might be able to meet the demand of a higher turbine inlet temperature without an increase in NO_x- and CO-emissions.
The configuration of a non-reacting jet in cross flow (JIC) is a common research topic in fluiddynamics (see [63,69,70,109,123]). However, so far little is known about the details of flame stabilization, heat release, and pollutant formation in premixed jets injected into hot cross flow. Further research is needed on how this configuration of staged combustion can be applied to achieve lower NO_x-emissions.
Most recently, numerical and experimental research on reacting and non-reacting jets in cross flow has been conducted at the Karlsruhe Institute of Technology. Jet flames of pure methane and premixed methane air mixtures in the second stage were studied using a test rig at elevated pressure (2-5bar) [43,118]. The configuration was numerically analyzed [20, 29] and validated against experimental results [21, 43]. Furthermore, swirling jets are numerically studied in non-reacting LES simulation [30]. The research focused on numerical code development and experimental data are mainly needed for validation. As a result, the simulations were able to predict flame shapes and positions.
A second research group with ongoing research in this field is situated at Purdue University. Experiments with fuel and fuel-air jets are conducted at elevated pressure (up to 5.5bar). The group experimentally investigates operating points beneficial in terms of CO- and NO_x-reduction below 10ppm [83, 84]. However, the ongoing research lacks results of the

combustion experiments concerning details on the mixture field and its influence on NO_x-formation.

1.3 Motivation of the Present Study

The present work contributes to fundamental research on reacting jets in hot cross flow as well as to its application in a novel combustion concept as a second stage of an axially staged combustor for stationary gas turbines. Certain points arise, concerning the technical feasibility of this concept with respect to modern stationary gas turbine combustors:

- Axially staged combustion as in a jet in cross flow configuration can be beneficial in terms of NO_x-reduction due to the shorter residence time in the hot environment of the second stage. In case of a higher equivalence ratio in the second stage, mixing of the jet with the exhaust gas of the cross flow is needed in order to avoid temperature peaks and high NO_x-formation rate. The technically feasible degree of (pre-)mixing and the connected NO_x-levels require further investigation.
- Lifting the flame off the jet outlet increases pre-flame mixing and will affect local flame temperature and NO_x-formation. The impact of this effect on combustion in an atmospheric test rig and differences at high pressure conditions are studied.
- Experimental data are analyzed in order to reveal connections between the mixture field and NO_x-formation in the mean and instantaneous mixture field. The influence of fluctuations and unmixedness on NO_x-formation in a reacting jet in hot cross flow is further analyzed.

In conclusion, evaluating the NO_x-formation in a JIC configuration requires a detailed study of the mixing field in order to identify the location of dominating NO_x-formation zones. This study primarily focuses on two points:

1. Description and characterization of the flow and mixture field of a plain round jet in cross flow by comparison of the reacting with the non-reacting case.

2. Further assessment of if and how a jet in cross flow configuration can contribute to reduction of NO_x-emissions from stationary gas turbines. This includes – besides the theoretically discussed perfectly premixed case – the realistic case of higher NO_x-levels in state of the art gas turbine combustors due to unmixedness.

As a starting point, the theoretical background needed for the study is discussed in chapter 2. This includes the fluiddynamics of jets in cross flow and fundamentals on turbulent reacting flows as well as chemical reactions, chemical modeling and NO_x-formation. In the following chapter 3, the atmospheric experiment is presented. The two different scaling laws applying ignition delay Damköhler number and Karlovitz number are discussed. Two different types of injectors are characterized which are further investigated in this study. The test rig provides good optical access which enables laser-optical measurements. The applied measurement techniques, described in chapter 4, include state of the art analysis on the basis of OH* chemiluminescence and with particle image velocimetry. Point-wise exhaust gas measurements are taken with a suction probe. A focus of the study lies on the experimental analysis of the relation between the turbulent velocity and mixture field and NO_x-formation. Therefore, a new detection method using Mie scattering was developed which allows for detection of the instantaneous mixture field of the reacting flow. In chapter 5, the theoretical NO_x reduction potential of axially staged combustion is studied numerically using simplified chemical models. The results from this study are taken as reference case for the following experimental and numerical analysis. Chapter 6 first presents the results of the anchored flames of a large diameter of 100mm. This stabilization mode was chosen to study details of the reacting flow and mixture field on a large scale. Relations between the mean and instantaneous mixture field and NO_x-concentrations are studied. In addition, a highly lifted flame of a small diameter of 15mm is investigated in order to extract the data needed for an estimation of NO_x-concentrations at high pressure gas turbine like conditions using a chemical network model. The network model analysis is presented in chapter 7. A sensitivity study reveals differences in NO_x-formation routes at atmospheric and 20bar conditions. Further analysis, using the experimental data of the lifted flame, includes more realistic gas tur-

bine conditions of higher NO_x-formations due to unmixedness in the first stage and air addition along the combustor liner.
In summary, the study combines experimental data with chemical network model simulations to specify conditions of beneficial application of axially staged combustion employing a jet in cross flow configuration in terms of NO_x-reduction.

2 Theoretical Background

In this chapter, an overview of the fluid dynamic phenomenon of jet in cross flow is given. Then, characteristic time and length scales of reacting flows are identified. Dimensionless numbers are determined to classify combustion regimes of turbulent flow. Following that, chemical reactions and kinetics are discussed with special focus on methane combustion and NO_x-formation. The basics of chemical reactor simulations using zero- (0D) and one-dimensional (1D) models are introduced. Finally, the influence of unmixedness as found in technical premixers of real gas turbine combustors is discussed in terms of NO_x-formation.

2.1 Jet in Cross Flow

A large body of literature on non-reacting jets in cross flow exists. A good summary is given by two recent review articles [72, 92]. In addition, the proceeding volume of the conference on jet in cross held in 1993 [94] provides a good overview of the different fields of research. While both compressible and incompressible JIC have been studied, only incompressible flows are considered in the following.
The jet in cross flow configuration is often used for premixing of fuel and air in burners, e.g. [6, 149]. The configuration is chosen because of enhanced mixing compared to a free jet. The good mixing performance is also of importance for reacting jet in cross flow applications. In the following sections the focus is on the non-reactive velocity and vorticity field.

2.1.1 Calculations and Parameters in a Jet in Cross Flow

The general coordinate system used throughout this study is exemplified in figure 2.1. The x-axis is parallel to the cross flow, the y-axis is the lateral coordinate and the z-coordinate follows the height of the channel. The corresponding velocities are u, v and w, respectively. Addition-

ally, in the x-z center plane the velocity magnitude c is calculated by the two velocity components u and w as $c=\sqrt{u^2+w^2}$. A secondary coordinate system with ξ, η and ζ will be used, which is bound to the trajectory of the jet: The ξ-coordinate points along the trajectory whereas η- and ζ-axes define the plane normal to the jet trajectory.

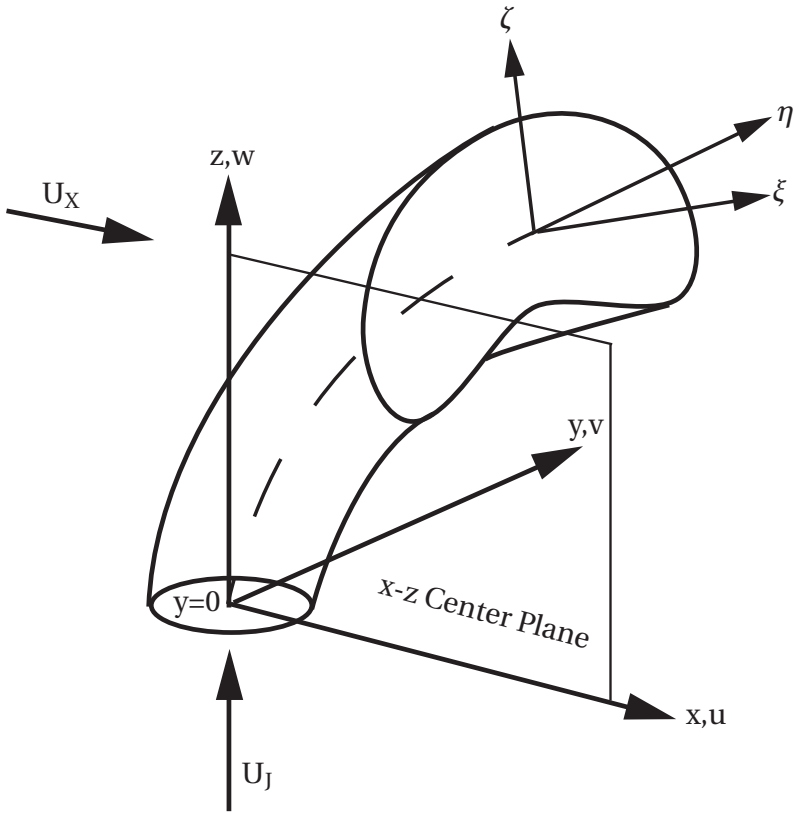

Figure 2.1: Introduction of the coordinate system.

The most important parameter of the isothermal jet in cross flow configuration is the velocity ratio $V = U_J/U_X$, with the jet velocity U_J and the velocity of the cross flow U_X. However, in the case of different densities of the two flows, it is more useful to employ the momentum (flux) ratio J according to equation 2.1 instead. The momentum ratio is expressed by the density and velocity ρ_X and U_X of the cross flow, and of the jet, ρ_J and U_J respectively, with

$$J = \frac{\rho_J U_J^2}{\rho_X U_X^2}. \tag{2.1}$$

Also widely used in literature is the blowing ratio r calculated with equation 2.2. In the case of isodensity flows, the blowing ratio r is equal to the velocity ratio V, which is the square root of J:

$$r = \sqrt{\frac{\rho_J U_J^2}{\rho_X U_X^2}} = \sqrt{J}. \tag{2.2}$$

2.1.2 Trajectory and Mixture Properties

A characterization of the overall flow and mixture field of jets in cross flow is made by the penetration depth of the jet. The trajectory analysis is conducted in the x-z center plane at y=0, where the deepest penetration is expected. Numerous correlations of these trajectories can be found in literature. There are three different procedures how trajectories are determined, e.g. [49, 51, 63, 69–71, 94, 123]:

1. The mixture trajectory is the sum of the loci with the poorest mixing, i.e. in the center of the jet core. As it is experimentally determined by temperature measurements of a heated jet, it is also referred to as the temperature trajectory, e.g. [63, 69, 70, 109, 123]. In this case, the trajectory follows the highest temperature.

2. In a similar way, the loci of the highest velocities can be used to determine the velocity trajectory, e.g. [63, 69, 70, 123].

3. The third option for extracting the jet trajectory from data is to trace the center streamline originating from the center of the injector exit, e.g. [155].

Following [155] and [29], the velocity trajectory coincides with the center streamline, at least near the jet outlet at small x-coordinates. Further downstream, the velocity trajectory penetrates deeper into the cross flow compared to the mixture trajectory. Published correlations for jet in cross flow trajectories are of the general form of equation 2.3 with normalized coordinates x/D and z/D:

$$\frac{z}{rD} = A\left(\frac{x}{rD}\right)^{B}. \tag{2.3}$$

The analysis of [17, 119, 136] indicate scaling with the blowing ratio r and the jet diameter D. Literature reviews [51, 94] reveal a wide scatter of the coefficients A (1.2<A<2.6) and B (0.28<B<0.34), depending on the characteristics of the investigated configuration and the applied experimental method. The wide spread of the trajectories illustrates that the penetration of jets in cross flow is very sensitive to boundary conditions. These can be wall boundary layer thickness, turbulence of the jet and the cross flow [21, 121], velocity inlet conditions [108], etc. Also, a minimum channel height H, depending on momentum ratio and jet diameter, must be given to eliminate the influence of the opposite wall [70]. Hasselbrink and Mungal [52] proposed to designate jets as not confined if rD<0.2H. In addition, rows of multiple jets can influence the pathway of the trajectories, e.g. [64, 65, 89]. A strong influence on the trajectory and the mixture field is exercised by different jet outlet geometries, e.g. [47, 53, 81, 90, 91, 107, 131], or by a swirling jet, e.g. [30, 154]. The numerical analysis in [20] shows an influence of jet Reynolds number on the trajectory and mixing field of the jet and cross flow for two studied laminar flow conditions. However, [136] showed that fully turbulent jets at higher momentum ratios are invariant to changes in Reynolds number.

Hasselbrink and Mungal showed in [51] that the correlation following equation 2.3 is only valid for high blowing or momentum ratios. For lower blowing ratios, the factor A becomes a function of the momentum or blowing ratio [136]. Following [51], the self-similarity indicates that in the region near the jet injection the trajectory is depending on the momentum ratio J exclusively. This dependency holds true if the jet velocity is much higher than the cross flow velocity, i.e. momentum ratios around 100 and higher. In conclusion, at a high blowing or momentum ratio the near-field region is similar to the one of a free jet.

A second correlation, that differs from equation 2.3 is proposed for lower momentum ratios in the range between 15≤J≤60 [63, 69]. In equation 2.4 and 2.5 the velocity and temperature trajectories are described by

two different correlations, depending on density ratio $\frac{\rho_J}{\rho_X}$ and momentum ratio J, in addition.

$$\text{Velocity}: \frac{z}{D} = 0.89\, J^{0.47} \left(\frac{x}{D}\right)^{0.36} \tag{2.4}$$

$$\text{Temperature}: \frac{z}{D} = 0.76 \left(\frac{\rho_J}{\rho_X}\right)^{0.15} J^{0.52} \left(\frac{x}{D}\right)^{0.27} \tag{2.5}$$

Compared to free jets, the entrainment of surrounding material in a jet in cross flow configuration is enhanced, e.g. [102]. The concentration decay of jet material along the center line of a turbulent free jet was studied by [125] and was found to be scalable by an exponent of -1. The works of [51, 52] and [136] compared the mixing behavior of a free jet to the mixing performance of a jet in cross flow.
First, in [136], a core region with no decay is distinguished from a near field region with enhanced mixing. In the far field region the entrainment of surrounding cross flow material is similar to the free jet. The beginning of the far field region depends on the diameter D and the momentum ratio J, i.e. z/JD=0.3 determines the beginning of the far field or wake-like region. In [136] the exponent of decay along jet trajectory coordinate ξ is specified with -1.3 in the near field. However, the decay in the far field follows $\xi^{-2/3}$. Similarly to the far field, [52] reports an exponent of $-2/3$ for the decay along the trajectory. In addition, the same enhanced mixing in the near field as in [136] was shown in the direct numerical simulation of a jet with Reynolds number of 5000 by Muppidi and Mahesh [104]. In this study, the authors revealed a higher contribution of mixing in the lee side shear layer compared to the windward shear layer. In conclusion, the mixing along the trajectory, which is often taken as reference, of a JIC is only enhanced compared to a free jet in the near field. However, the whole planar mixture field must be considered for comparison. In this respect, the JIC configuration shows better mixing also in the far field [104].
Concerning reacting jets in cross flow, Hasselbrink and Mungal [52] show that jet flames have a slightly deeper penetration than non-reacting counterparts. This lower penetration is accounted to a reduced mass entrainment rate (up to a factor of two) for the reacting cases. This reduced entrainment is explained by the fact that a burning layer covers

the jet. The trajectory correlations of non-reacting cases are not directly applicable to reacting jets, as the jet is accelerated by the chemical reaction and its expansion which results in additional momentum. This additional momentum leads to an overall deeper penetration of the jet into the cross flow.
In case of reacting premixed jets, the momentum ratio can either be calculated by the (unburnt) inlet conditions of density $\rho_{J,u}$ and velocity $U_{J,u}$, or, as proposed in the following, using the corresponding velocity $U_{J,b}$ and density $\rho_{J,b}$ of the burnt jet. According to continuity, the unburnt and the burnt state follow equation 2.6 if constant flow cross-sectional areas for the reactants and the combustion products are assumed:

$$\rho_{J,b} U_{J,b} = \rho_{J,u} U_{J,u}. \tag{2.6}$$

If we further assume that the densities of the cross flow ρ_X and of the burnt jet $\rho_{J,b}$ are equal, we obtain equation 2.7, which provides the relationship between the momentum ratio calculated with the properties of the combustion products J_{react} and the momentum ratio J based on jet inlet conditions. With this modified expression of the reacting momentum ratio J_{react}, correlation for non-reacting jets can be used for prediction of trajectories, if reaction is present.

$$J_{react} = \left(\frac{\rho_{J,u}}{\rho_X}\right)^2 \frac{U_{J,u}^2}{U_X^2} = J\frac{\rho_{J,u}}{\rho_X} \tag{2.7}$$

2.1.3 The Vortex System

The steady and unsteady vorticity and velocity fields of non-reacting jet in cross flow have been extensively studied. A comprehensive investigation on the vortical structures is given in [42] (see additionally an experimental study in [75] and a numerical simulation in [156]). The four main vortex systems in a jet in cross flow (see figure 2.2) are determined as:

- the counter-rotating vortex pair (CVP),
- shear layer vortices,

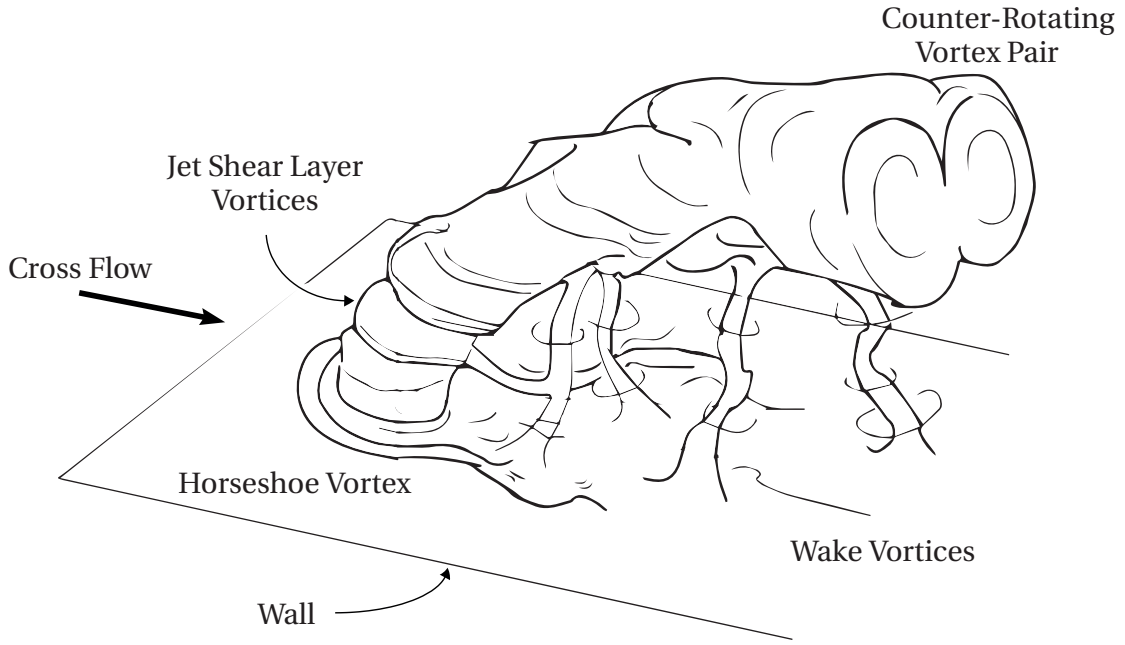

Figure 2.2: Vortex system in a jet in cross flow, adapted from [42].

- the horseshoe vortex, and
- wake vortices.

The most prominent vortex system is the counter-rotating vortex pair in the plane normal to the jet trajectory. Early works on the vorticity field of jet in cross flow already described these two vortices to be characteristic of the flow in the far field [35, 71, 102]. However, for low momentum ratios of J≈1, [100] reports the shear layer vortices to be characteristic. The initiation and formation of the CVP is experimentally studied in detail in [88] using a water channel, and numerically in [24]. The origin of the characteristic vortex pair is interconnected with the rolling and shedding of the shear layer vortices. In a free jet the shear layer vortices have the shapes of rings around the jet. In the vicinity of the jet exit, this holds also true in a jet in cross flow configuration. However, the shear layer vortices are distorted by the cross flow. The jet gains additional momentum in x-direction immediately upon entering the cross flow. In figure 2.3 the point at the side is indicated as the initiation of the counter-rotating vortex pair. Further downstream, the shear layer vortices are disturbed on the lee side, whereas, the windward shear layer vortices keep their ring-like shape. The disturbance of the cross flow, initially at

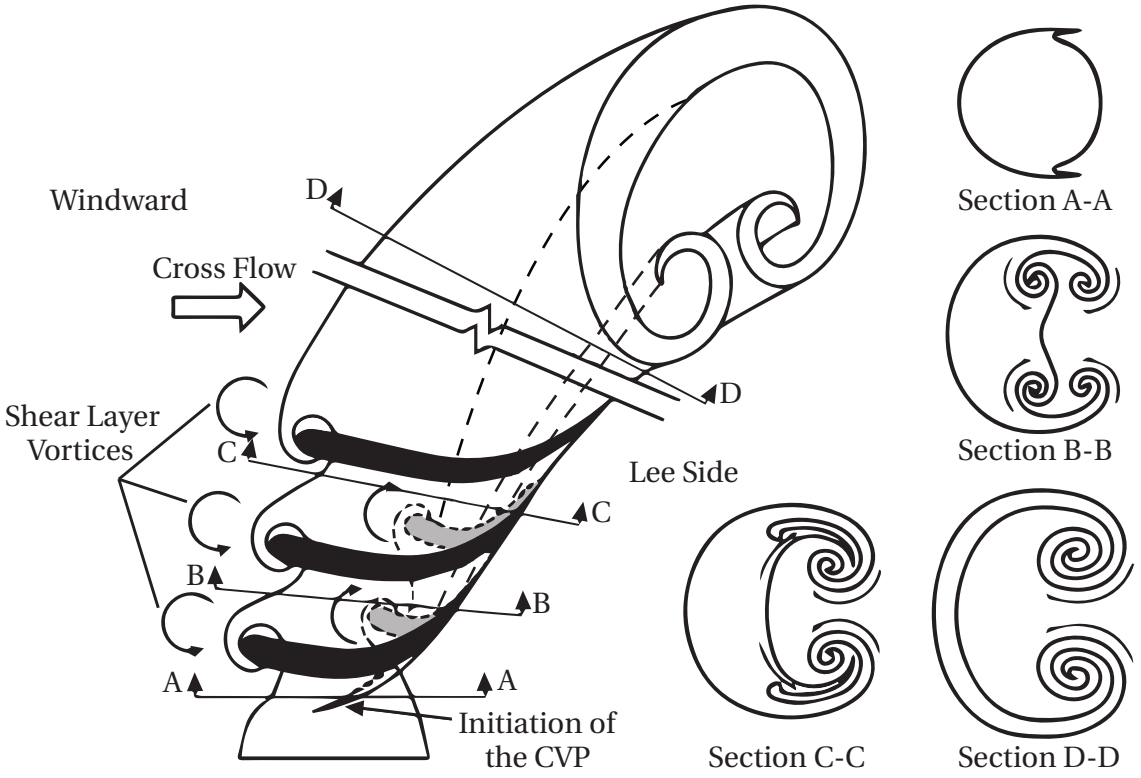

Figure 2.3: Interaction of shear-layer vortices and the initiation of the CVP, adapted from [88].

the side, is transported with the jet downstream where the jet is bent in direction of the cross flow. In the far field, this disturbance results in the formation of the counter rotating vortex pair.

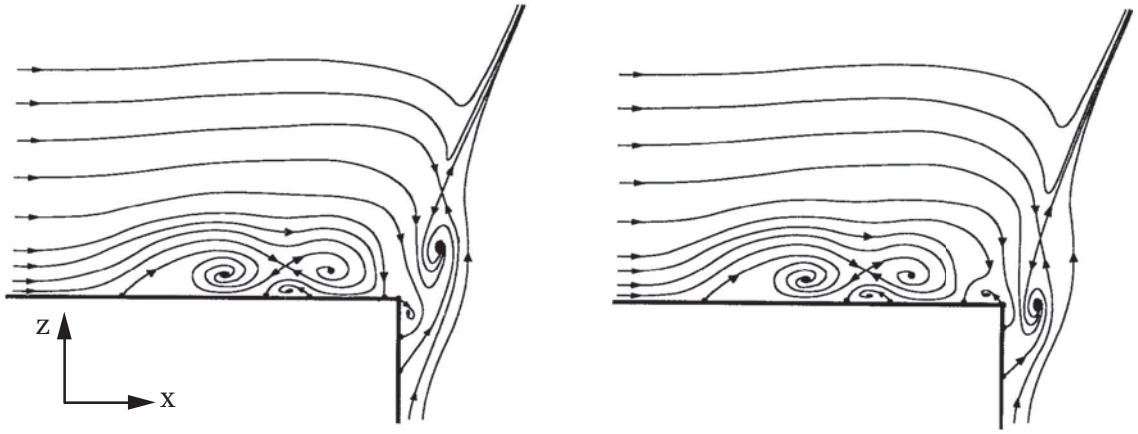

Figure 2.4: Horseshoe vortex system and the interaction with the jet shear layers at two oscillating stages, adapted from [76].

The horseshoe vortex system is formed in the boundary layer upstream of the jet injection. In order to understand the interaction between the horseshoe vortex and the jet shear layers, it is interesting to have a closer look at the region of the jet injection. Figure 2.4 shows the streamlines of a vertical cut in the x-z center plane, adapted from [76]. In [76], an oscillating interaction between the horseshoe vortex system and the jet shear layers is described in the region near the outlet. Due to this oscillation, the streamlines of the cross flow penetrate into the jet pipe (see scheme on the left side of figure 2.4).

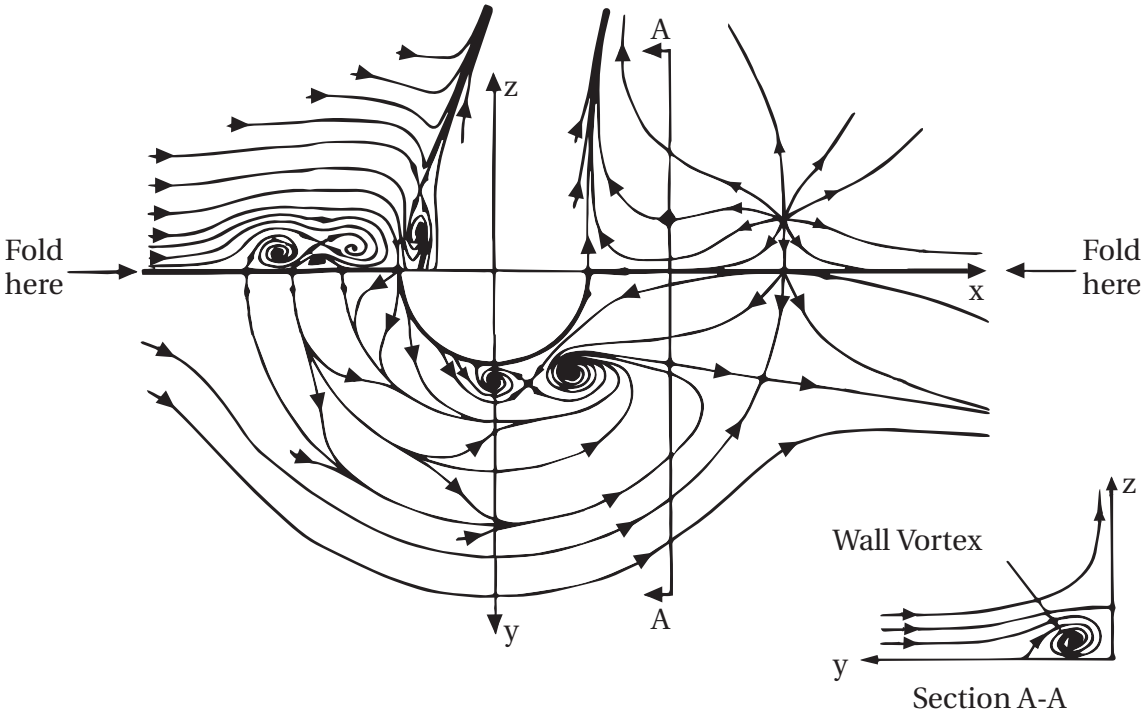

Figure 2.5: Vortex system at jet inlet, adapted from [75].

The characterization of jet in cross flow following [42] distinguishes between three different regimes, depending on the velocity ratio. For velocity ratios below J≈2, the jet does not clearly separate from the lower wall of the channel. At a velocity ratio of V>4, the wake region consists of upward streamlines, see the wake vortices in figure 2.2. The Strouhal number of wake vortices in this regime is mostly independent of both, the Reynolds number and the momentum ratio, and is around 0.13 [42]. With higher velocity ratios, the wake vortices are stretched as the jet penetrates deeper into the cross flow and display the shape of thin strains.

By this effect, most of the cross flow fluid in the wake region near the wall is unaffected by the jet. For higher momentum ratios the influence of the lower wall on the velocity and vorticity field decreases.
An overview of the flow field around the jet outlet is given in figure 2.5 [75]. The horseshoe vortex system is located around the jet detached in the wake region behind the jet. The shear layer vortices are perturbed at the sides of the jet where the CVP is initiated.
It has to be kept in mind that this characterization of the flow field is a result of experiments and simulations of non-reacting jets. However, non-reacting case studies can help to understand flame flow interactions and the stabilization of the flame in the flow field. Influences of the flame on the velocity field indeed need to be studied and analyzed in more detail.

2.2 Time Scales and Dimensionless Numbers in Turbulent Reacting Flows

In turbulent reacting flows, dimensionless numbers are frequently used to characterize the interaction between turbulence and chemical reaction. Expressions of characteristic time scales for turbulent flow and reaction are discussed in the following.

2.2.1 Characterization of Turbulent Flows

The Reynolds number (see equation 2.8) indicates the ratio of the molecular diffusive transport and convective transport of specific momentum. For pipe flows, the transition from laminar to turbulent flow is around a Reynolds number of 2000 [143]. However, the point of transition depends on the type of flow as well as boundary conditions.
In a jet in cross flow the Reynolds number is calculated using the conditions of the jet flow, with the mean velocity U_J, the jet diameter D, and the kinematic viscosity of the fluid ν:

$$\mathrm{Re} = \frac{U_J D}{\nu}. \tag{2.8}$$

High Reynolds number turbulent flows are characterized by fluctuations in pressure and velocity around a steady mean value in case of a stationary flow, see figure 2.6. Velocity fluctuates in all three dimensions u, v and w independently [117, 151]. The highest fluctuation is measured for the main velocity component u. The values of the velocity fluctuations in v- and w-direction perpendicular to the main flow are in the same order of magnitude. In the experimental results of chapter 6, the Root Mean Square value (RMS_c) and the turbulence intensity Tu in the x-z center plane are calculated with

$$Tu = \frac{RMS_c}{U_J}, \text{ where} \tag{2.9}$$

$$RMS_c = \sqrt{\frac{1}{2}\left(\overline{u'^2} + \overline{w'^2}\right)}. \tag{2.10}$$

In equation 2.9, the turbulence intensity Tu is normalized by the mean velocity in the jet U_J. The RMS_c value combines the absolute velocity fluctuation in x- and z-direction. The turbulence intensity is an indicator for velocity fluctuations in the turbulent flow and is given in percentage. The turbulence intensity Tu is a local indicator for turbulence and is used in the following to characterize shear layer turbulence in the investigated jet in cross flows.
The statistical analysis with the RMS value cannot provide a description of how often a certain turbulence fluctuation occurs. A Probability Density Function (PDF) analysis can be used to determine the probability of a certain event, e.g. [117]. With this method, the number of occurrences are plotted for each event. Figure 2.6 illustrates the turbulent fluctuation of velocity around a steady mean value and the resulting PDF function. In general, this analysis can be applied to every quantity within the flow field. In the case of two mixing flows, as in a jet in cross flow configuration, the distribution of the local mixture fraction can also be analyzed by PDF distribution.

2.2.2 Turbulent Length and Time Scales

Turbulence is a three-dimensional unsteady phenomenon and can be described and characterized by the statistical approaches above. The

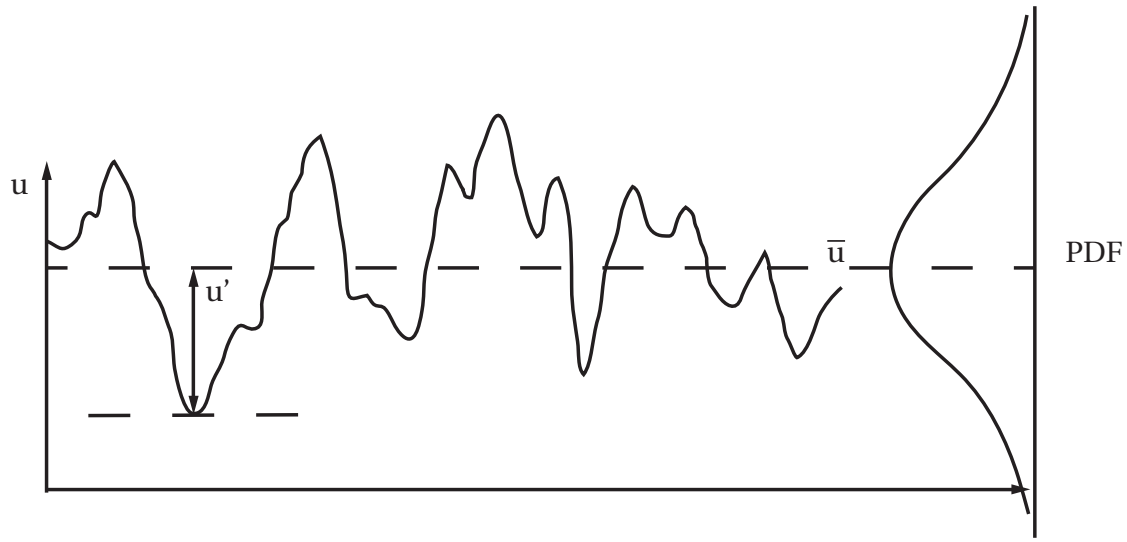

Figure 2.6: Turbulent fluctuations and probability density in a stationary turbulent flow, adapted from [143].

global mixing behavior of a turbulent flow is invariant to Reynolds number, however, not the turbulent small scale structures. This means that the size and the amount of the smallest structures (eddies) in the turbulent flow depend on Reynolds number. Mixing processes take place on the small scale of turbulent eddies. In general, turbulence enhances diffusivity and mixture as with an increasing Reynolds number more and smaller eddies appear. These eddies lead to steeper gradients and increased contact areas. The spatial structures of typical length scales can be described by the so-called eddy dissipation model. The model based on Kolmogorov's theory from 1941 is valid for homogeneous isotropic turbulence. Details can be found in textbooks, e.g. [44, 114, 117, 127, 143, 144]. In the following, the discussion is restricted to statements needed to describe different flame regimes, mainly corresponding to [44, 114].
Turbulent length and time scales are characteristic of the flow and depend on boundary conditions. The major length scales are: the macroscale (or characteristic width of the flow D), the integral length scale (or turbulent macroscale) and the smallest eddies also called Kolmogorov length scale. The largest turbulent length scales are of the order of the main geometrical dimension of the flow. The integral length scale is the length scale of the mean size of the largest eddies and contains the highest turbulent kinetic energy [144]. The smallest eddies cover

the length scale where turbulent dissipation takes place. Kinetic energy is exchanged between eddies. On statistical average following Kolmogorov's hypothesis, turbulent kinetic energy is transported along the eddy cascade from integral length scale to the microscale. Only in the viscous subrange the energy is consumed by dissipation. The vortex size where dissipation starts to play a role is determined by the Kolmogorov length scale $l_{turb,K}$.
Connected to the macro length scale $l_{turb,D}$ is the turbulent macro time scale $\tau_{turb,D}$. Equation 2.11 expresses the turbulent macro time scale $\tau_{turb,D}$ with the temporal velocity fluctuation u' and the size of the largest eddies $l_{turb,D}$.

$$\tau_{turb,D} = \frac{l_{turb,D}}{u'} \tag{2.11}$$

The size of the integral scale $l_{turb,D}$ is in the same order of magnitude as the overall (burner) geometry, i.e. diameter D. The size of the smallest eddies where dissipation takes place can be expressed by the kinematic viscosity ν and the eddy dissipation rate ϵ to

$$l_{turb,K} = \left(\frac{\nu^3}{\epsilon}\right)^{\frac{1}{4}}. \tag{2.12}$$

Similarly, the time scale of the Kolmogorov micro length scale is expressed as

$$\tau_{turb,K} = \left(\frac{\nu}{\epsilon}\right)^{\frac{1}{2}}. \tag{2.13}$$

Following Kolmogorov' hypothesis, the dissipation of energy on microscale equals the energy transferred by the eddies of the integral length scale. The eddy dissipation rate ϵ is expressed with the global turbulence of the flow with the velocity fluctuation u' and the macro length scale of the geometry by

$$\epsilon = \frac{u'^3}{l_{turb,D}}. \tag{2.14}$$

Using the main characteristic length $l_{turb,D}$ and the velocity fluctuation u', the turbulent Reynolds number Re_t is determined by

$$Re_t = \frac{u' l_{turb,D}}{\nu}. \tag{2.15}$$

2.2.3 Chemical Time Scales and Flame Thickness

In addition to the time scales of the turbulent flow, characteristic chemical time scales are introduced. As discussed in [48], two mechanisms of flame stabilization exist in premixed jet in cross flows. First, the flame is stabilized due to flame deflagration. Second, in high temperature regions, autoignition effects play an important role. Both mechanisms must be considered in determining the position of the premixed flame within the mixture field (see the modeling of lift-off height in [78]). The chemical time scale τ_{chem} depends on the laminar burning velocity S_l and flame thickness δ_f and is expressed by

$$\tau_{chem} = \frac{\delta_f}{S_l}. \tag{2.16}$$

This timescale is also called "flame time" as it refers to the residence time in the flame front [114]. In figure 2.7, the concepts of laminar flame speed S_l and flame thickness δ_f are illustrated. The freely propagating laminar flame is stabilized at the position where the velocity of the incoming fresh gas equals the propagation speed of the laminar flame, i.e. laminar flame speed or burning velocity S_l. In the flame front, heat is released due to chemical reaction. This results in a temperature gradient over the flame front. If no heat losses are present, the temperature of the burnt gas reaches the adiabatic flame temperature T_{ad}. In the following, the end of the flame is determined as the point where 99.5% of the adiabatic flame temperature is reached. The regions upstream and downstream of the flame front are called pre- or post-flame zone respectively, the area of the flame front is also referred to as in-flame zone. This division of pre-, in- and post-flame zone is used in the remainder of this study.

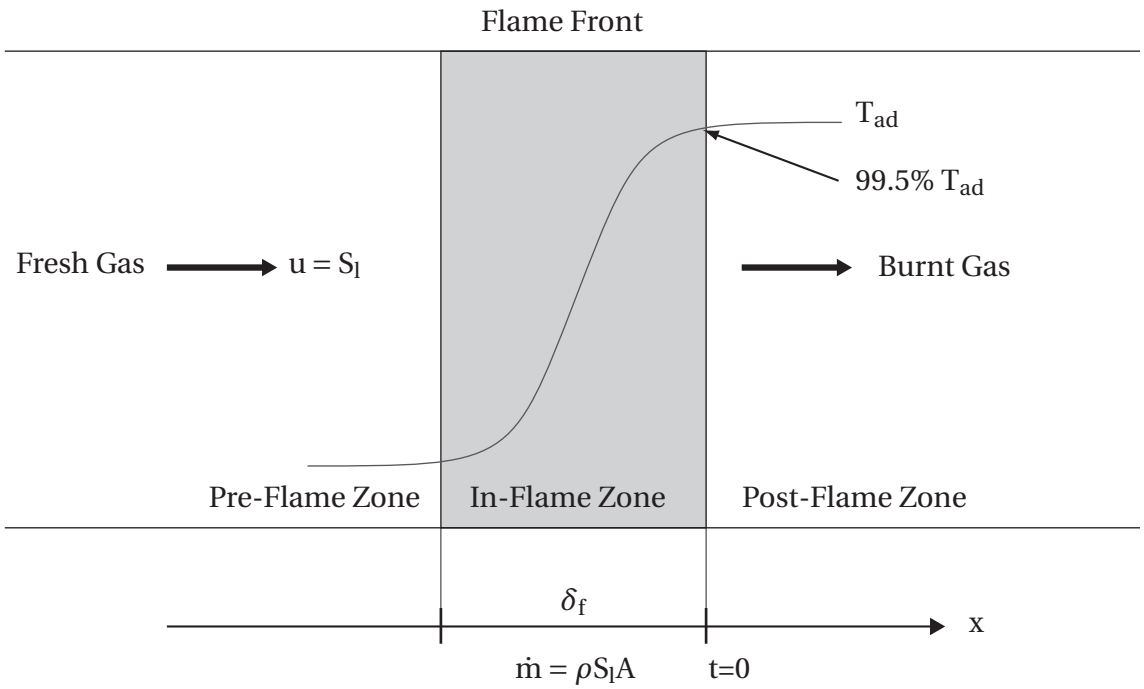

Figure 2.7: Scheme of the temperature distribution over the flame front of a stabilized freely propagating flame, after [38].

The flame thickness δ_f is expressed by the ratio of mass diffusivity Δ and laminar flame speed (equation 2.17) [114]. There are additional expressions of the flame thickness as e.g. by the gradient of the temperature profile or via the burning rate [58].

$$\delta_f = \frac{\Delta}{S_l} \tag{2.17}$$

The laminar free flame model (details in section 2.3.2.1) is used to calculate laminar flame speeds under varying conditions. A correlation for laminar flame speed including dependency on pressure and equivalence ratio is given in [112].
A second chemical time scale is the so called ignition delay time τ_{ign}. In literature, the ignition delay time is experimentally determined by shock-tube tests, e.g. [66, 137, 148]. In contrast to flame propagation, the reaction is initiated by spontaneous autoignition of the combustible mixture, at high temperature ([157] reports autoignition not to occur below 810K for atmospheric methane mixtures). The dependencies of

ignition delay time τ_{ign} can be described by an Arrhenius-type correlation as

$$\tau_{ign} \propto \exp\left(\frac{E_A}{RT}\right) [O_2]^i [CH_4]^j, \tag{2.18}$$

with the activation energy E_A and the temperature of the mixture T. The influence of the mixture, i.e. the molar concentration of O_2 $[O_2]$ and methane $[CH_4]$, depends on the exponents i and j. Following [137], the ignition delay time of a stoichiometric methane air flame strongly depends on temperature T, hardly on methane concentration (whether a higher methane concentration leads to a shorter or longer ignition delay time also depends on the temperature range) and is almost proportional to pressure. The pressure dependency of equation 2.18 is given by the molar concentrations which are directly proportional to the density of the mixture.

2.2.4 Characterization of Flame Regimes

With the time and length scales for the turbulent flow and the chemical reaction, dimensionless numbers are introduced. With these numbers different regions can be distinguished which characterize the flame regimes [7, 12, 25, 111].
In the following, the influences of turbulence on flame structure are discussed referring to textbooks [44, 114, 144]. In this context, the ratio of convection to thermal and mass diffusion is characterized by dimensionless numbers. The Prandtl number compares the viscous diffusion rate of the velocity field (with the kinematic viscosity ν) to the thermal diffusion rate of the temperature field (with the thermal diffusivity α). For gases, typical values for the Prandtl number lie between 0.7 and 1 depending on temperature, pressure and fluid. The Schmidt number compares momentum diffusivity (with the viscosity ν) to diffusive mass transport (with the mass diffusivity Δ). For gases the Schmidt number is around 1. Only for highly diffusive gases as hydrogen the Schmidt number is smaller than one. Finally, the Lewis number compares the Schmidt number to the Prandtl number, describing the ratio of thermal to mass diffusion. An appropriate assumption for methane combustion is made

by setting the Prandtl and Schmidt numbers to one, also resulting in a Lewis number of unity, see equation 2.20.

$$\mathrm{Pr} = \frac{\nu}{\alpha} = \mathrm{Sc} = \frac{\nu}{\Delta} = 1 \tag{2.19}$$

$$\Rightarrow \mathrm{Le} = \frac{\mathrm{Sc}}{\mathrm{Pr}} = \frac{\alpha}{\Delta} = 1 \tag{2.20}$$

With these assumptions and the flame thickness δ_f of equation 2.17, the turbulent Reynolds number of equation 2.15 can be rewritten as

$$\mathrm{Re_t} = \frac{\mathrm{u'l_{turb,D}}}{\mathrm{S_l}\delta_f}. \tag{2.21}$$

The turbulent Reynolds number of reacting flows characterizes the effect of turbulence on the flame front. In the so-called Borghi diagram given in figure 2.8, the turbulent Reynolds number of unity distinguishes laminar flames of combustion regime (1) from flames where turbulence is able to interact with the flame front. If turbulence is in the same range as the flame speed or smaller, i.e. $\frac{u'}{S_l}<1$, and the turbulent Reynolds number $\mathrm{Re_t}$ is high, turbulence can wrinkle the flame front (flame regime (2)).
To further distinguish the flame regimes in the scheme of figure 2.8, the turbulent Damköhler and Karlovitz number are used. In general, the Damköhler number is expressed by the ratio of turbulent time scale to chemical time scale. The turbulent Damköhler number $\mathrm{Da_t}$ is expressed by

$$\mathrm{Da_t} = \frac{\tau_{\mathrm{turb,D}}}{\tau_{\mathrm{chem}}} = \frac{\frac{\mathrm{l_{turb,D}}}{\mathrm{u'}}}{\frac{\delta_f}{\mathrm{S_l}}} = \frac{\mathrm{S_l l_{turb,D}}}{\mathrm{u'}\delta_f}, \tag{2.22}$$

with the turbulent macro time scale, given by equation 2.11, and the chemical time scale calculated with the laminar burning velocity $\mathrm{S_l}$ in equation 2.16. The turbulent Damköhler number indicates to what extend the large-scale vortices $\mathrm{l_{turb,D}}$ of the turbulent flow field can interact

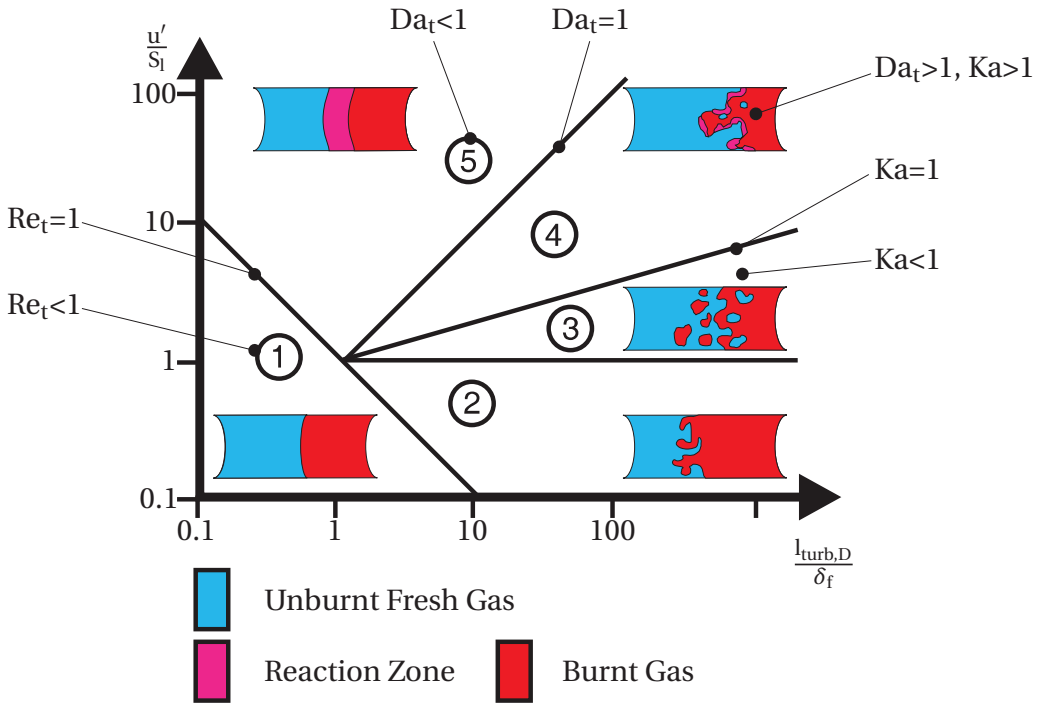

Figure 2.8: Borghi diagram, adapted from [80].

with the reaction zone. For the regime (5) with the turbulent Damköhler number Da_t smaller than unity, the chemical reaction is slow compared to the turbulent mixing resulting in a homogeneous reaction zone, similar to the combustion mode in well stirred reactors.
Further division of the turbulent flame regimes is made by the Karlovitz number Ka. The chemical time scale is compared to the time scale of the eddies on micro length scale:

$$Ka = \frac{\tau_{chem}}{\tau_{turb,K}} = \frac{u'^{\frac{3}{2}}\alpha^{\frac{1}{2}}}{S_l^2 l_{turb,D}^{\frac{1}{2}}} = \frac{u'^{\frac{3}{2}}\delta_f^{\frac{1}{2}}}{S_l^{\frac{3}{2}} l_{turb,D}^{\frac{1}{2}}} = \frac{\frac{\delta_f^{\frac{1}{2}}}{S_l^{\frac{3}{2}}}}{\frac{l_{turb,D}^{\frac{1}{2}}}{u'^{\frac{3}{2}}}}. \tag{2.23}$$

Equation 2.23 includes the expression of the eddy dissipation rate of equation 2.14 and the turbulent macro length scale $l_{turb,D}$. The last form of equation 2.23 shows that also the Karlovitz number compares the chemical time scales of the flame front with the global turbulence, however, weighted by different exponents.

For both flame regimes (3) and (4) in figure 2.8, the laminar flame speed is low compared to the turbulence intensity, i.e. $\frac{u'}{S_l}>1$. In contrast, the regime of the wrinkled flame (2) is characterized by a smaller turbulent velocity fluctuation u' compared to the laminar flame speed S_l. In the corrugated flame regime (3) the Karlovitz number is smaller than unity. Turbulence is high enough to distort the reaction zone and portions of unburnt material are separated from the main flame front. Following Peters [111], the two combustion regimes of the wrinkled (2) and the corrugated flame (3) are combined to the flamelet regime. The flame front of this regime is composed of flamelets and can be simulated with simplified laminar models. Regime (4), i.e. the so called thickened wrinkled flame, is characterized by a Karlovitz number higher than unity. In the regime of the thickened wrinkled flame, the smallest eddies can interact within the flame front, that leads to a turbulent thickened flame region where reaction takes place. This regime is of technical interest, as lean and highly turbulent high pressure combustion, as in industrial gas turbines, is characterized by this regime [23].
In contrast to the Borghi diagram of figure 2.8 with the thickened wrinkled flame regime (4) and the regime of a homogeneous reaction zone (5), Peters [113, 114] differentiate a turbulent combustion regime ($Re_t>1$,$Ka>1$) consisting of thin reaction zones. In this regime the smallest eddies of the Kolmogorov microscale are able to enter the chemically inert preheat zone of the flame. However, the inner layer of the reaction zone of the flame is not disturbed as the smallest eddies are larger than the reaction layer [113]. Peters combines the regime of thin reaction zones with the wrinkled and corrugated flame regime to the flamelet regime. In the flamelet regime reaction takes place in thin layers which can be modeled by laminar flamelets.
Similar to the turbulent Damköhler number Da_t, the ignition delay Damköhler number Da_{ign} is introduced using the ignition delay time τ_{ign} as the chemical time scale

$$Da_{ign} = \frac{\tau_{turb,D}}{\tau_{chem}} = \frac{l_{turb,D}}{u'\tau_{ign}}. \tag{2.24}$$

The application of the Damköhler ignition delay number Da_{ign} is appropriate when ignition delay plays a major role in the reacting field.

2.3 Chemical Reaction and Kinetics

Generally, a chemical elementary reaction converts reactants into products. The conversion time is related to the rate coefficient, which is given for the forward and backward reaction. A multistep reaction mechanism includes several elementary reactions and is described by the net production rate. Chemical formation rates depend on the condition of the system, as the concentration of reactants, the temperature, radiation effects, the presence of a catalyst or inhibitor [44], and also the pressure. In all chemical reactions, the reaction rate determines the kinetics, i.e. the time-dependent formation of products. Assuming sufficient residence time, the back- and forward reactions are in chemical equilibrium. However, when it comes to emission formation, reaction timescales play an important role. NO equilibrium state is usually not reached in the typical residence times of a combustor. Equilibrium thermal NO-values are far above acceptable levels for gas turbine combustion.

2.3.1 NO_x-Formation in Methane Combustion

In literature, different routes of NO_x-formation in methane combustion are described. An overview is given in [32, 44, 60, 144], based on the reviews [14, 101]. NO and NO_2 are the most important contributers to the formation of nitrogen oxides in combustion processes. In combustion, mainly NO is formed. Post processes in the atmosphere further oxidize NO to NO_2, which makes NO_2 the main precursor of acid rain and smog. In combustion processes NO_2 can be formed [144] via reaction 2.25. On the other hand, reactions 2.26 and 2.27 consume NO_2. The formation of NO_2 in equation 2.25 needs the HO_2 radical, which is only present in low temperature regions.

$$NO + HO_2 \rightleftharpoons NO_2 + OH \tag{2.25}$$

$$NO_2 + H \rightleftharpoons NO + OH \tag{2.26}$$

$$NO_2 + O \rightleftharpoons NO + O_2 \tag{2.27}$$

NO_x-formation can be allocated to different chemical pathways. However, in this study, a division between the NO_x formed in the flame (in the

following in-flame NO_x), and NO_x originating from the residence time in hot environment after the flame (referred to as post-flame NO_x) is made. The time stamp is set to zero once 99.5% of the adiabatic flame temperature is reached. The NO_x produced in advance is allocated to the in-flame NO_x. The post-flame NO_x-formation is evaluated according to the residence time. All NO_x-values in this study are normalized to 15% O_2 in order to make emission levels comparable with each other. Details on other methods of emission level normalization are discussed in [130].
The four main mechanisms of NO-formation in combustion of fuels not containing nitrogen compounds are introduced in the following.

2.3.1.1 Zeldovich or Thermal Mechanism

Thermal NO-formation is one of the main sources of nitrogen oxides in combustion contributing to post-flame NO_x. Equilibrium considerations, see equation 2.28, can be used to estimate the maximum contribution of the thermal NO-formation route. However, as the chemical equilibrium of the thermal mechanism is not reached during typical timescales of a combustion chamber, the formation of thermal NO strongly depends on kinetics and residence time.

$$N_2 + O_2 \rightleftharpoons 2NO \tag{2.28}$$

The thermal or Zeldovich mechanism, first postulated by Zeldovich in 1946 [158], consists of two chain reactions

$$O + N_2 \rightleftharpoons NO + N, \tag{2.29}$$

$$N + O_2 \rightleftharpoons NO + O. \tag{2.30}$$

The extended Zeldovich mechanism also includes reaction

$$N + OH \rightleftharpoons NO + H. \tag{2.31}$$

In order to form NO the triple bound between the two N atoms of the nitrogen molecule needs to be broken. Due to the high activation energy of reaction 2.29 (319.05 kJ/mol [144]), the formation of NO via the Zeldovich mechanism is strongly temperature dependent. Substantial

formation of thermal NO occurs at temperatures above 1600K [152] (details on reaction rates are given in [14, 101]). The rate at which NO is formed depends on the radical concentrations of O, N and OH. An accurate prediction of thermal NO-formation requires the correct prediction of the N and further also the O radical concentration. In combustion processes where the reaction of fuel conversion is fast compared to the reactions of the thermal NO-mechanism, it can be assumed that concentrations of N_2, O_2, O, and OH concentrations are at their equilibrium [144]. However, for slow combustion processes, as e.g. in non-premixed flames at high pressure, superequilibrium states of O- and also OH-concentrations can contribute to in-flame NO-formation via the extended Zeldovich mechanism [14, 105].

2.3.1.2 Fenimore or Prompt Mechanism

Fenimore [37] was the first to postulate the existence of a rapid formation of NO in hydrocarbon flames, i.e. prompt NO-formation later also referred to the Fenimore mechanism. The Fenimore mechanism is more dominant in rich flames as the mechanism is initiated by hydrocarbon radicals present in and near the reaction zone [13, 37, 44, 57, 150]. The highest level of prompt NO-formation is found at an equivalence ratio of 1.4 [37]. Initially, a hydrocarbon radical (e.g. CH,C) attacks a nitrogen molecule.

$$CH + N_2 \rightleftharpoons HCN + N \tag{2.32}$$

$$C + N_2 \rightleftharpoons CN + N \tag{2.33}$$

The starting reactions initiated by hydrocarbon radicals have a lower activation energy compared to the thermal NO-reaction. Prompt NO-formation is – in contrast to the Zeldovich mechanism – not strongly dependent on temperature. For equivalence ratios ϕ<1.2 the chemical reactions

$$HCN + O \rightleftharpoons NCO + H, \tag{2.34}$$

$$NCO + H \rightleftharpoons NH + CO, \tag{2.35}$$

$$NH + H \rightleftharpoons N + H_2, \tag{2.36}$$

and finally the reaction of the N radical to NO via equation 2.31 is the dominant path of the prompt NO-mechanism [57,144]. The prompt NO-mechanism is complex. The importance of different pathways depends on combustion conditions, e.g. equivalence ratio and pressure. A review of prompt NO-formation can be found e.g. in [14, 44].

2.3.1.3 N_2O-Intermediate Mechanism

A further contributor to in-flame NO-formation is the route via N_2O [14, 44]. The three-body recombination chain of reactions includes the following reactions:

$$O + N_2 + M \rightleftharpoons N_2O + M, \tag{2.37}$$

$$H + N_2O \rightleftharpoons NO + NH, \tag{2.38}$$

$$O + N_2O \rightleftharpoons NO + NO. \tag{2.39}$$

The N_2O mechanism is of interest when overall NO_x-levels are low, as in very lean, low temperature combustion, and also at increased pressure [14, 44, 105, 144].

2.3.1.4 Formation Route Via NNH

An additional formation route of NO via NNH radicals was first postulated by Bozelli and Dean [16]. The NO-formation of the NNH mechanism includes the following reactions:

$$N_2 + H \rightleftharpoons NNH, \tag{2.40}$$

$$NNH + O \rightleftharpoons NO + OH. \tag{2.41}$$

The intermediate formation of NNH and the further reaction to NO plays a role in premixed methane and hydrogen flames [50, 56]. The NO formed via the NNH route contributes to the in-flame NO_x-formation [44].

2.3.2 Reactor Models for Chemical Simulation

In the following, two types of chemical reactor models are applied using Cantera [45]. First, the laminar one-dimensional free flame (1DFF) is in-

troduced. This reactor is applied in order to study the flame front and the in-flame NO_x-formation in detail. For the post-flame zone where entrainment of cross flow material plays a major role, a zero-dimensional constant pressure reactor is used. Details on idealized chemical reactor modeling can be found e.g. in [73, 144].

2.3.2.1 1D Free Flame

Numerical simulations of a freely propagating adiabatic one-dimensional laminar flame, see figure 2.7, are conducted using the free flame code in Cantera (details are given in the documentation [19]). The flame is stabilized at the position where fresh gas velocity and the burning velocity of the flame are in equilibrium. The code accounts for multicomponent molecular transport in axial direction (1D assumption).
The inlet condition is specified by temperature and composition.[1] The mass flux of the system is a dependent variable which needs to be determined as part of the steady-state solution. Therefore, an additional condition is required. A fixed temperature at a given grid position is determined in order to stabilize the flame within the grid. This temperature, together with the starting grid, must be chosen thoughtfully in order to get convergence of the steady-state solution. For faster convergence, a starting solution is calculated on a coarse grid. The grid is then refined adaptively until the gradient at the inlet and outlet vanishes.[2]
The global mass flux and the composition at every grid point determines the axial velocity in each cell. This velocity is used together with the grid width to calculate post flame residence times.
The governing equations (following [74, 114]) are

$$\dot{m} = \rho u A \tag{2.42}$$

for continuity and

[1] The underlying concept is the one of a perfectly premixed flame. In chapter 7, the inlet composition is determined by the pre-flame mixture fraction.
[2] The settings of the maximum relative gradient and curvature of the solution vector are: slope=0.1, curvature=0.2.

$$\dot{m}\frac{dT}{dx} - \frac{1}{c_p}\frac{d}{dx}\left(\lambda A\frac{dT}{dx}\right) + \frac{A}{c_p}\sum_k\left(\rho Y_k V_k c_{pk}\right)\frac{dT}{dx} + \frac{A}{c_p}\sum_k\left(\dot{\omega}_k h_k M_k\right) = 0 \quad (2.43)$$

for energy conservation. Equation 2.43 contains (from left to right) the change of energy due to heat convection, heat conduction, and thermal diffusion, as well as heat release due to chemical reaction. Further, the conservation of species conversion (consumption and formation) for each species k due to convection, diffusion or chemical conversion is given by

$$\dot{m}\frac{dY_k}{dx} + \frac{d}{dx}\left(\rho A Y_k V_k\right) - A\dot{\omega}_k M_k = 0. \quad (2.44)$$

The governing equations are discretized by finite difference approximations in axial direction. The numerical solution technique is a hybrid Newton time-stepping algorithm (see details in [74]).

2.3.2.2 0D Reactor Model

In the network model of chapter 7 the post-flame region is modeled by a constant pressure reactor (CPR) [19]. A CPR consists of a perfect mixer and a chemical reactor, see figure 2.9. With this model the time dependent solution is calculated.
The reactor is advanced over a time step Δt.[3] Time stepping is continued until the desired residence time is reached. Further, flow data from the velocity and mixture field are needed to connect the results of the residence time to a position on the trajectory. The starting condition of the reactor is determined by the composition and temperature of the products of a free flame simulation. In order to model cross flow entrainment, an additional mass Δm_x per time step Δt flows from a reservoir into the reactor, see figure 2.9. The reservoir contains the products of a free flame calculation of the cross flow. The actual mixture fraction f is determined by the actual mass of cross flow m_X and jet m_J in the system:

[3] The settings of relative and absolute error tolerances over an integrating time step are: rtol=10^{-9} and atol=10^{-20}.

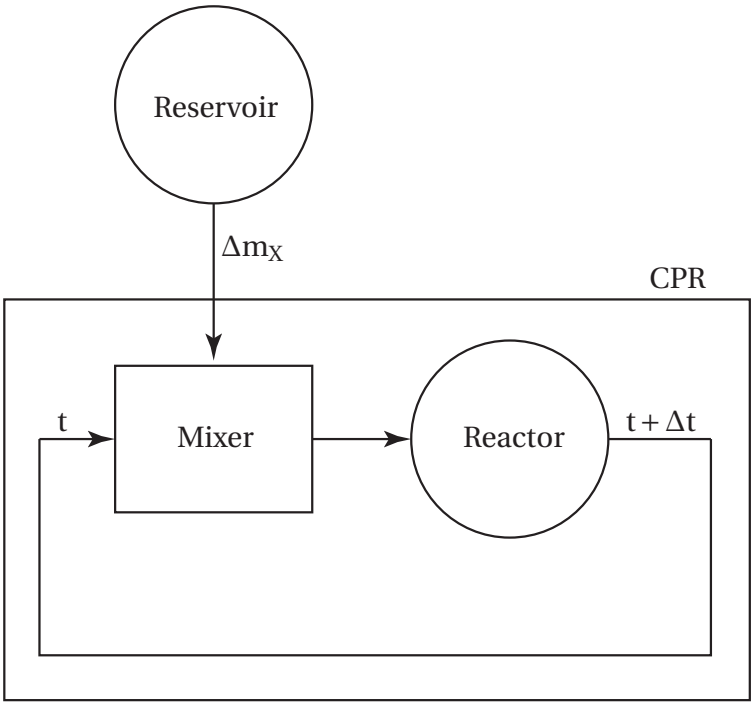

Figure 2.9: Scheme of the CPR model setup.

$$f = \frac{m_J}{m_J + m_X}. \tag{2.45}$$

The pressure in the reactor is constant. As additional mass is filled into the reactor, the (virtual) volume of the reactor grows. However, the absolute mass and volume of the reactor is not of interest as there is only one thermodynamic state in the reactor (0D assumption), i.e. temperature and composition. The important parameter is the actual mixture fraction of jet and cross flow in the reactor, which is controlled by the incoming mass flow of burnt cross flow material Δm_X.
The state variable in a CPR is the total enthalpy. As the coupled set of differential equations, presented in the following, are solved implicitly for every time step independently, mass diffusion between the two time steps, which would correspond to mixing in the flow direction, is neglected.

First of all, equation of continuity must be solved with

$$\frac{dm}{dt} = \dot{m}_{in}. \tag{2.46}$$

The species conservation for each species k is formulated in equation 2.47, accounting for the incoming mass flow of the species, as well as formation or consumption with the molar rate of production $\dot{\omega}_k$. The incoming flow may have a different mass fraction of the species $Y_{k,in}$ depending on supplying reservoir, than the actual mass fraction Y_k in the reactor at this time.

$$m\frac{dY_k}{dt} = \dot{m}_{in}(Y_{k,in} - Y_k) + V\dot{\omega}_k M_k \tag{2.47}$$

The general equation of total internal energy – being the first law of Thermodynamics – for an open system is given by

$$\frac{dU}{dt} = -p\frac{dV}{dt} - \dot{Q} + \dot{m}_{in}h_{in}. \tag{2.48}$$

Additionally, the enthalpy equation

$$H = U + pV \tag{2.49}$$

holds true. If constant pressure is given, this results (together with the energy equation 2.48) in

$$\frac{d(mh)}{dt} = -\dot{Q} + \dot{m}_{in}h_{in}. \tag{2.50}$$

Further, total enthalpy is replaced by state variable of temperature. This results in the final equation 2.51, which is solved in Cantera for a CPR.

$$mc_p \frac{dT}{dt} = -\dot{Q} - \sum_k h_k V \dot{\omega}_k M_k + \dot{m}_{in}(h_{in} - \sum_k h_k Y_{k,in}) \tag{2.51}$$

2.3.3 Evaluation of Reaction Mechanism for Methane Combustion

The combustion of hydrocarbons, especially of methane as the main component in natural gas, is extensively covered in literature. Among the most widely used mechanisms are the GRI2.11 [15] and GRI3.0 [135] mechanism of the Gas Research Institute, which are adjusted to experimental data of methane combustion (e.g. ignition delay, flame temperature and laminar flame speed, as well as NO_x-concentrations).
Specified mechanisms for the combustion of syngas including H_2 and CO [106] have been developed. Adaption is needed as different pathways of forming and consuming intermediate species become important, when fuels containing H_2, CO or higher hydrocarbons are burnt. Recently, more complex mechanisms were published: e.g. a mechanism including higher hydrocarbons (AramcoMech1.3 with 290 species) [99] and a mechanism with an adaption to high pressure application [115]. These mechanisms are very complex and consist of more than 1000 different elementary chemical reactions. However, most of them do not include NO_x-chemistry. It is advised by the authors not to add further reaction equations, as e.g. the ones including the NO_x-chemistry. As the mechanism is optimized as a whole, no substitution or further selective tuning should be done.
In the following, the GRI mechanism is chosen as it includes NO_x-chemistry. The GRI2.11 consists of 277 elementary chemical reactions of 49 species [15], the GRI3.0 includes 325 reactions of 53 species [135]. Simulations of an atmospheric free flame at equivalence ratio of 0.5 were run with both mechanisms. The results of the GRI3.0 mechanism showed overall lower NO_x-concentration which can be attributed to a lower in-flame NO_x-formation compared to the GRI2.11 mechanism. In comparison to experimental results, the simulation with the GRI2.11 mechanism is in better agreement with measurements taken at the end of the combustor (NO_x-concentrations ≈4ppm consistently). Therefore,

this mechanism was chosen for the detailed chemical modeling presented in chapter 5 and 7.

2.3.4 Emission Formation Under Gas Turbine Conditions

In the chemical model of the freely propagating one-dimensional flame (figure 2.7), it is assumed, that combustion takes place in laminar premixed flamelets. However, as it was stated already in section 2.2, the flame structure at gas turbine conditions is rather that of the thickened wrinkled flame. Following Peters [113], the thickened wrinkled flame regime is part of the thin reaction zone regime. This combustion regime can be modeled with the laminar 1D free flame as the smallest eddies can only enter the preheat zone of the flame whereas the reaction zone is kept undisturbed. Combustion in real gas turbines is characterized by high pressure (for stationary gas turbines around 20bar), high turbulence due to high velocities, and low residence times (typically in the range of 20ms) [10, 11, 23, 86, 87, 132]. Although the topology of flame fronts at high turbulence levels is complicated, zero-dimensional or one-dimensional laminar flame calculations with detailed chemistry are in acceptable agreement with experimental findings regarding NO_x-formation (as shown in [132]).
In state of the art can combustors, NO_x-emissions around 10-15ppm are achieved under imperfectly premixed conditions. This NO_x-level is twice to three times higher than the theoretically achievable emissions under perfectly premixed conditions [87]. This fact can be linked to two effects: First, technically premixed conditions in real gas turbines always include a certain degree of unmixedness of air and fuel prior to combustion due to incomplete mixing. Second, leakage and spent cooling air is added along the liner which does not participate in combustion. Therefore, a higher temperature in the flame zone is needed for a given turbine inlet temperature. The temperature difference can be in the range of 100K or more [23]. With the increased sensitivity of NO_x-formation to temperature at high pressure, both effects lead to twice to three times higher NO_x in real gas turbines compared to the theoretical level.
The influence of unmixedness on NO_x-formation, especially in high pressure combustion, is of utmost importance [11,28,41,82]. In the early work of Danckwerts [26], the basic characteristics of the "goodness of

mixing" are given. In [26] it is distinguish between the spatial and temporal homogeneity of a mixture. Thus, we express – similar to the velocities in section 2.2.1 – the temporal fluctuation f' of the instantaneous local mixture fraction f* related to the local mean value f as

$$f' = f^* - f. \tag{2.52}$$

With the temporal fluctuation of equation 2.52, we obtain the local temporal RMS_T value as

$$RMS_T = \sqrt{\overline{f'^2}}. \tag{2.53}$$

The local temporal RMS_T value is averaged for all measurement points in the y-z plane to obtain a spatial mean RMS value of the temporal fluctuations $\overline{RMS_T}$. This value can be referred to the ideal global mean mixture f_{ideal}. The ideal mixture is determined by perfectly mixed flows. In case of a jet in cross flow, equation 2.54 compares the mass flow of the jet $\dot{m}_J$ to the total mass flow of jet and cross flow, similar expressions are given e.g. in [121]; likewise, a expression with air and fuel mass flows is applied to (partially) premixed flames.

$$f_{ideal} = \frac{\dot{m}_J}{\dot{m}_J + \dot{m}_X} \tag{2.54}$$

To characterize the spatial homogeneity in comparison with the global ideal mixture fraction f_{ideal}, the spatial RMS_S value is expressed by

$$RMS_S = \sqrt{\overline{(f - f_{ideal})^2}} \tag{2.55}$$

in every y-z plane perpendicular to the cross flow. The mean mixture fraction f at every measurement point is compared to f_{ideal}. With the RMS values calculated with equation 2.53 and 2.55, the temporal and spatial unmimxedness factors U_T and U_S are expressed as

$$U_T = \frac{\overline{RMS_T}}{f_{ideal}}, \text{ and} \tag{2.56}$$

$$U_S = \frac{RMS_S}{f_{ideal}}. \tag{2.57}$$

It has been shown that for a successful reduction of NO_x-emissions not only spatial inhomogeneities have to be eliminated, but also temporal fluctuations, because these fluctuations lead to hot spots and locally higher thermal NO_x-formation, see e.g. the simulation in [28]. Fric [41] reports that 10% temporal unmixedness lead to twice the NO_x-emissions (the mean mixture values being the same) compared to perfectly premixed test cases in an atmospheric test rig. The author further anticipates that this effect has a stronger influence at high pressure gas turbine like conditions, as thermal NO_x sensitivity is increasing with pressure. Biagioli and Güthe [11] confirm these findings, applying one-dimensional analysis with detailed chemistry.

3 Experimental Setup

The jet in hot cross flow configuration is investigated with an upscaled atmospheric test rig. In the following, the test rig and its components are described. The dimensioning is outlined and explained with the underlying scaling laws, using the dimensionless numbers presented in section 2.2. Finally, the boundary conditions and operating points of the experimental analysis of chapter 6 are presented.

3.1 Test Rig and its Components

Figure 3.1 shows the CAD model of the test rig. It comprises two axially staged combustion zones: The first combustion stage consists of 16 burners providing the hot cross flow of combustion products. The segmentation of the first combustion stage into a number of smaller individual flames provides a homogeneous temperature distribution across the hot flow upstream of the secondary injection. Each burner is equipped with a mixing tube followed by a swirler, which generates the recirculation zones in the primary stage required for aerodynamic flame stabilization. The front panel is cooled by the air flow in the plenum. The channel of the primary combustion zone is impingement-cooled. Due to the quick burn-out of the 16 small flames the cross flow is fully burnt when it reaches the secondary combustion zone. The comparison of NO_x-measurements with literature data and chemical calculations indicates that almost perfect mixing is achieved upstream of the exit of the burners.
The second combustion stage provides the premixed jet in hot cross flow, which is in the focus. A single jet of premixed reactants is injected from the bottom into the horizontal channel consisting of hot combustion products of the cross flow. For sufficient fuel-air premixing in the injector, a commercially available static mixer is placed 20 jet diameters upstream of the injector exit, providing a mixture quality of 99.8% at the mixer outlet. In addition, several perforated plates act as flow straighten-

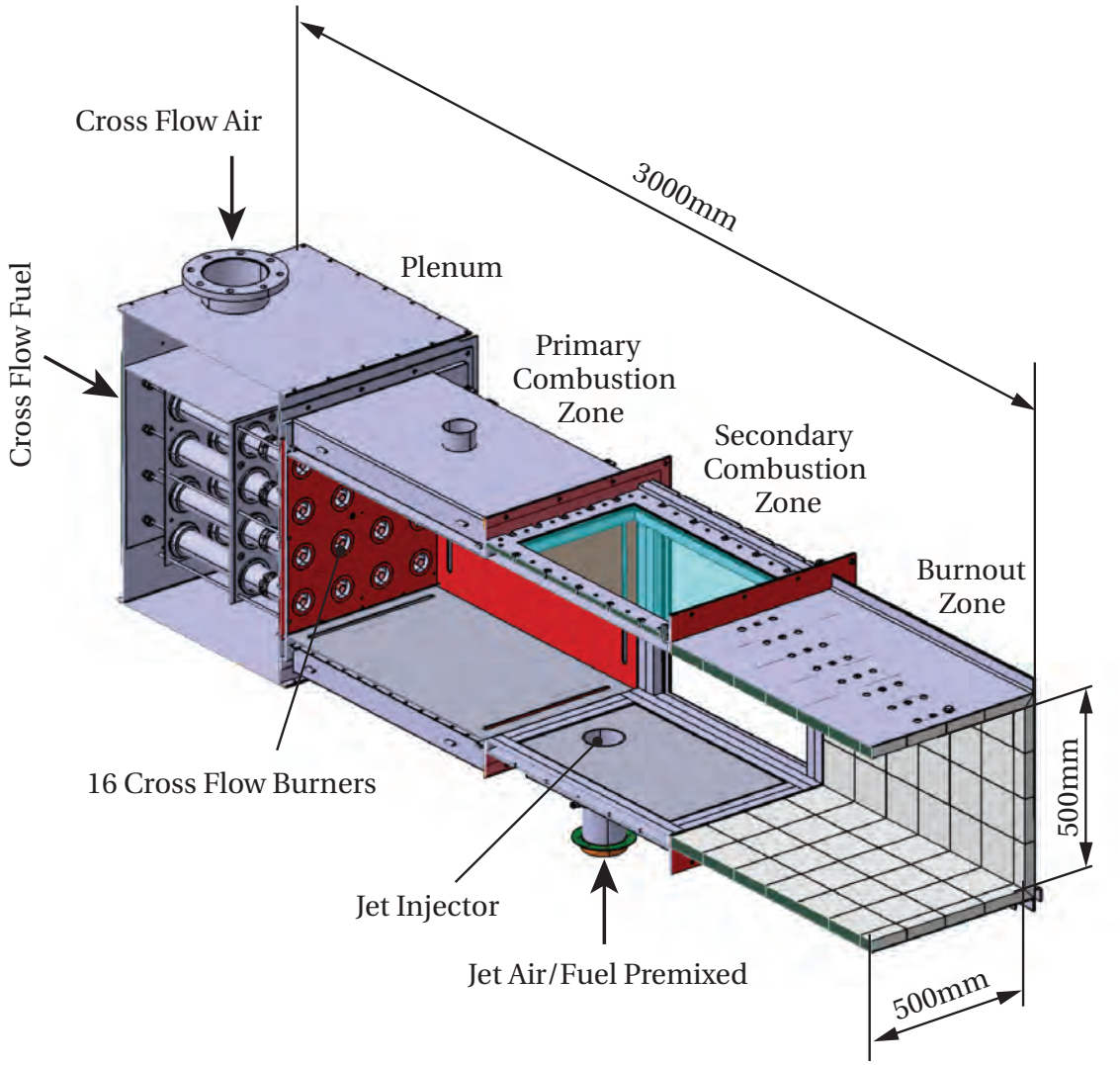

Figure 3.1: Sketch of the large scale test rig.

ers ensuring a turbulent flow profile near the injector exit [134]. The second combustion stage can be equipped with windows (quartz glasses) for optical access from up to three sides. This good optical access is important for the application of laser-optical measurements. The bottom plate and the quartz glasses are impingement-cooled by air jets. For the exhaust gas measurements, a suction probe is inserted into the channel (details in chapter 4). Therefore, one side window can be replaced by ceramic panels of varying geometry. In this way, different measurement positions downstream of the jet injection can be realized. The metal window frames of the secondary combustion zone is water-cooled in order

to avoid thermal distortion, which would break the glasses. As the flame length varies with operating condition, a burnout zone with ceramic insulation is attached to the second combustion stage to provide enough time for full burnout. The hot gases from the combustor are diluted with cooling air before they are released to the environment through an exhaust duct with large cross section.
In both combustor stages, the air can be preheated to up to 673K. Natural gas from the local supply line (exact composition given in [141]) is used as fuel. More information on the test rig is provided in [3, 77, 134].

3.2 Scaling of the Experiment

The atmospheric test rig is scaled to a hypothetical gas turbine combustion chamber. Typically, combustion in a real industrial gas turbine is characterized by a highly turbulent flow at high pressure, i.e. 20bar. Two different types of scalings are applied to the test rig: The first scaling of the test rig is based on Damköhler number similarity using ignition delay as chemical time scale. A second scaling applies Karlovitz number similarity. The flame scaled by Karlovitz number is assumed to show similar flame shape and lift-off characteristics compared to a typical flame in a gas turbine combustor. In the following, the two different scalings will be explained.

3.2.1 Ignition Delay Damköhler Number Similarity

The first scaling of the test rig is realized using the ignition delay Damköhler number Da_{ign} (see equation 2.24). This similarity results in an upscaling of the atmospheric test rig compared to a gas turbine combustor. Due to the up-scaled dimensions and the resulting higher spatial resolution this scaling is suitable for studying the interaction between the mixture and NO_x-field of the reacting flow in detail.
In order to have the same ignition delay Damköhler number Da_{ign} in the atmospheric test rig and at 20bar gas turbine conditions, the ratio between the turbulent time scale $\tau_{turb,D}$ and the ignition delay time τ_{ign} must be similar. As we assume both flows to be fully turbulent, the turbulent time scale only depends on the turbulent fluctuations, which can be directly connected to the mean velocity, i.e. same turbulence inten-

sity. Further, it was shown in section 2.2 that the ignition delay time is approximately inversely proportional to pressure. This means that at 20bar the ignition delay time is shorter by a factor of 20. This increase of the ignition delay time under atmospheric conditions has to be compensated by a higher turbulent time scale depending on the macro length scale $l_{turb,D}$ and the velocity fluctuation u'. Two possible adjustments can be made: First, the geometry can be scaled up in order to increase the macro length scale. Second, as the turbulent time scale further depends on velocity fluctuations, which are directly connected to the mean flow velocity, the velocity can be scaled down. Taking into account the infrastructural limitations regarding mass flows and power, a global geometrical upscaling of a factor of 4, and downscaling of the velocity by a factor of 5 has been chosen for the experiment [134]. This scaling results in lower Reynolds numbers of the atmospheric flows. However, all flows are still fully turbulent (see details in table 3.1).
This scaling is applied to the dimensioning of the cross flow, leading to a channel height and width of 500x500mm and to the initial jet diameter of 100mm. This scaling strategy further leads to longer absolute residence times in the experiment compared to the hypothetical gas turbine combustor. The estimated total residence time of a hypothetical gas turbine combustor is assumed to be 18ms. According to the velocity scaling factor of 5, the total residence time in the experiment is five times longer, i.e. 90ms. These numbers have to be taken into account when it comes to the modeling of NO_x-formation. For a better comparison between the two cases of 1 and 20bar (as applied in the chemical benchmark modeling of chapter 5) all residence times are normalized by the overall residence time in the combustor, i.e. τ_{cc}=1 at the end of the combustion chamber. Concerning the application of the Da_{ign} scaling of the jet, the momentum ratio of the experiment is in the same range as in gas turbine combustors.

3.2.2 Dimensioning by Karlovitz Number Similarity

Another scaling method is required to capture the effect of flame lift-off. This lifted flame is of importance for the evaluation of NO_x-formation, and is further used for data transfer to high pressure gas turbine conditions, see chapter 7. In order to get a similar flame behavior in terms

of lift-off height, scaling by Karlovitz number has been chosen. Kolb et al. [78] revealed that the lift-off height mainly depends on the laminar flame speed and the velocity at the jet outlet. Generally, a higher laminar flame speed S_l of the jet mixture will reduce the lift-off height. Autoignition plays a minor role, but is needed to explain the influence of cross flow temperature on the lift-off height of the jet (see for details [78]). The model proposed in [78] would predict a lift-off height in the hypothetical gas turbine combustor at 20bar of approximately three to five jet diameters.[1]
In the experiment, a lift-off height in the required range of three to five jet diameters is only achievable at high jet velocities. Due to infrastructural limitations, scaling according to Karlovitz number requires downscaling of the jet diameter to D=15mm. With the high velocity at the jet outlet, leading to a Karlovitz number above unity, see table 3.1, the jet is assumed to have a similar flame lift-off behavior as in a gas turbine combustor. However, as it was not possible to run the cross flow at higher velocity, this results in a higher momentum ratio of the jet scaled by Karlovitz similarty, i.e. J=150 (typical for a gas turbine combustor would be 4 to 15). In addition, to make the NO_x-measurements comparable to engine conditions, the experimental operating point must have a similar equivalence ratio and full pre-heating temperature at the inlet.

3.3 Inlet Conditions and Operating Points

The employed scaling laws lead to two different jet injector diameters of 100 and 15mm, respectively. The cross flow is scaled according to the ignition delay Damköhler number. In the following, the parameter of operating points resulting from these two scalings are presented.
For all experiments in this study, the cross flow is operated at an equivalence ratio of ϕ_X=0.5, resulting in an adiabatic flame temperature of approximately T_{ad}=1750K. The inlet temperature of the cross flow as well as the jet is T_{in}=673K, as all air flows are electrically preheated. The Reynolds number of the cross flow (approx. 24 400) is large enough to provide fully turbulent flow conditions.

[1] However, the model described in [78] is based on atmospheric experimental operating points.

Table 3.1: Operating points of ignition delay Damköhler scaling (Da_{ign}) and Karlovitz scaling (Ka).

	D [mm]	J	ϕ_J	U_J $[\frac{m}{s}]$	Re	Ka	Da_t
Da_{ign}	100	4-10	0.05-0.77	≈25	≈30 000-50 000	≈0.05-4	≈10-1000
Ka	15	150	0.66/0.77	110	26 500	3.3/1.5	16/35

Table 3.1 summarizes the parameter of the jet for the two different scaling methods. To be able to calculate the turbulent Damköhler number Da_t and the Karlovitz number Ka (see equations 2.22 and 2.23), a few assumption must be made. First, the jet diameter D is taken as the integral length scale. The turbulent velocity fluctuation u' is approximated with 10% of the mean jet velocity U_J. The thermal and mass diffusivity are assumed to be similar (following equation 2.20). The laminar flame speed is calculated with the correlation of Peters [112].

$$Ka \approx \frac{\left(U_J \cdot 0.1\right)^{1.5} \alpha^{0.5}}{D^{0.5} S_l^2} \tag{3.1}$$

$$Da_t \approx \frac{D S_l^2}{\left(U_J \cdot 0.1\right) \alpha} \tag{3.2}$$

First, the scaling according to similarity in ignition delay Damköhler number with the jet diameter of 100mm is applied to operating points with momentum ratios between 4 and 10. The equivalence ratio is varied over a wide range of very lean mixtures up to almost stoichiometric conditions (see section 6.1). The potential analysis of staged combustion in chapter 5 and the network simulation in chapter 7 use a mass split ratio of 11%. This mass split ratio corresponds to the reference case of the jet at momentum ratio J=6, which is seen to be in the momentum ratio range of technical relevance.
Two operating points of the Karlovitz scaling with the jet diameter of 15mm are selected for thorough analysis. Only the jet with an equivalence ratio of ϕ_J=0.66 is investigated experimentally. In chapter 7 the

chemical network model is also performed at the jet equivalence ratio of ϕ_J=0.77 to study the influence on NO_x-formation. Due to the smaller diameter, the jet mass flow is smaller than the mass flow of the reference case at the mass split ratio of 11%. Therefore, the mass split ratio needs to be adapted for proper analysis of the global NO_x-concentrations in section 7.5.

4 Measurement Techniques

The applied measurement techniques include standard analysis of OH* chemiluminescence and velocity field via particle image velocimetry. Conventional exhaust gas measurements with a suction probe are applied to calculate the mixture fraction using O_2-measurements and to extract normalized NO_x-concentrations. A new measurement technique was developed, which provides instantaneous and mean mixture fractions in the measurement plane of a laser sheet that is of special interest for the application to the mixing of a reacting jet in cross flow.

4.1 OH* Chemiluminescence

The OH* chemiluminescence of the jet flame of the secondary stage was recorded with a high speed camera (Photron FASTCAM-ultima APX) equipped with an image intensifier [116]. The camera records images with up to 2000 frames per second at full resolution of 1024x1024 pixels. The emission spectrum of OH* chemiluminescence is in the wavelength range around 309nm. In order to collect only the emission of the OH* chemiluminescence, a band pass filter of 309nm ±5nm is used. This application allows for a good elimination of interfering surrounding light. Since the chemiluminescence emission of OH* is not within visible spectral range, the detection of OH* is more convenient than other radicals, e.g. CH*.
Details on the physics of chemiluminescence can be found in e.g. [33, 146]. OH* chemiluminescence is emitted by OH-radicals, which are formed as intermediate molecules by chemical reactions in the flame front. Chemiluminescence is emitted, as electrons are transfered from an excited state to their ground state. The intensity of the OH* chemiluminescence depends on temperature and pressure and is used as an indicator of the rate of heat release [85]. Flames with lower equivalence ratios and a resulting lower flame temperature show weaker chemiluminescence emissions. To make weaker signals visible, higher gains of

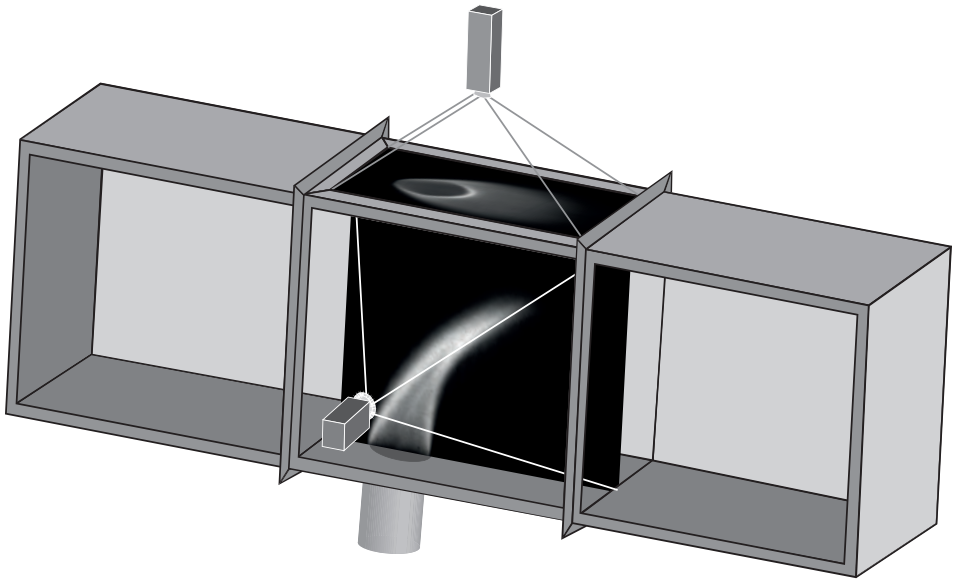

Figure 4.1: Setup of the OH*-measurements with two cameras located at the side and at the top.

the image intensifier are used. To be able to compare absolute intensities of recordings at different gains, the internal amplification factor must be determined. The conversion factor is experimentally measured by the detection of a LED light recorded with different gains (see [85] for a similar setup). In the analysis of the experimental results (chapter 6), flames of different OH* intensities are discussed. Initially all images of a operating point are averaged. The intensities of each operating point are normalized by their maximum intensity. The resulting mean images are compared with each other without gain correction. This kind of comparing is applied to operating points with different momentum ratios at the same equivalence ratio. For comparison between operating points at different equivalence ratios the conversion factor of different gains is taken into account. In this case, all intensities are normalized by the highest intensity of all operating points.
The OH* chemiluminescence recording provides a line of sight integrated picture of the flame. The recording collects the total emission of OH* chemiluminescence either in lateral view or in top view (see setup in figure 4.1). As the flame possesses no axial symmetry, Abel-inversion is not applicable. However, the side view together with the top view provide a good impression of how the flame looks like in three dimensions.

4.2 Point-Wise Exhaust Gas Measurements

Exhaust gas is measurement in planes perpendicular to the cross flow, at several positions downstream of the jet injection. For all operating points in this study, the flame is completely burnt at the position of measurement. All fuel is consumed, and CO oxidation is completed and in thermal equilibrium.
For the exhaust gas measurements, a suction probe was mounted on a computer controlled traversing system. This setup allows for point-wise measurements in the cross section (see figure 4.2 for an example of the position showing the NO_x-field). The water-cooled probe consists of a countercurrent heat exchanger. The required time to quench the exhaust gas temperature in the probe to 1500K is 0.5ms. It is assumed that at this temperature all chemical reactions forming NO_x are quenched. The probe is connected to the gas analyzers via a heated pipe. The gas probe temperature in the pipe is held constant around 100°C to prevent condensation of water. In the analyzer unit the sample flow is split. The one branch is connected to the NO_x-analyzer. NO_x-concentrations are measured with a chemiluminescence analyzer. In the other branch all water in the gas probe is removed by a condenser. The O_2 unit of the analyzers uses paramagnetism as detection method (see [34] and [1] for details).
In the following, the data analysis procedure of the taken concentration measurements to normalized condition is presented. Details on the calculations can be found e.g. in [144]. The standardization is needed to make exhaust gas measurements of different o_2-concentrations comparable (see [130] for an overview of different normalization methods).

4.2.1 Mixture Fraction from O_2-Measurements

In general, CO_2 and O_2-concentrations in combustion exhaust gas can be used to determine the equivalence ratio. The precision of the procedure depends on the measured concentration of O_2 and CO_2, respectively. Using O_2-measurements, accuracy is higher for leaner flames. In this study, all operating points have air excess, making usage of O_2-concentration preferable over CO_2-concentration [103]. The equivalence ratio at measurement point ϕ_{MP} can be calculated with the local

dry oxygen concentration γ_{O_2}:

$$\phi_{MP} = \frac{\gamma_{O_2,air} - \gamma_{O_2}}{\gamma_{O_2,air} - \gamma_{O_2}\left(1 - \frac{v_{min,dry}}{l_{min}}\right)}. \tag{4.1}$$

The calculation by means of equation 4.1 needs to take the properties of the applied fuel into account. The exact composition of the natural gas from the local supplier is given in [141]. For this composition of natural gas, the minimum air needed at stoichiometric condition is l_{min}=9.64, and the stoichiometric dry exhaust gas is $v_{min,dry}$=8.65, see table 4.1 (details on the derivation are given in [62]). The volume fraction of O_2 in air $\gamma_{O_2,air}$ is taken as 20.942%.

Table 4.1: Summary of the parameters needed for exhaust gas analysis.

	Methane	Natural Gas [141]
v_{min}	10.55	9.64
$v_{min,dry}$	8.55	8.65
l_{min}	9.55	9.64
ϕ_{15}	0.307	0.306

With the local equivalence ratio at the measurement point ϕ_{MP} calculated by the O_2-concentration, the mixture fraction in each measurement point can be determined applying equation 4.2. The variables are the calculated local equivalence ratio ϕ_{MP} and the equivalence ratio of the jet ϕ_J and the cross flow ϕ_X. The equivalence ratio of the jet and the cross flow are globally calculated on the basis the mass flows of air and fuel.

$$f = \frac{\phi_{MP} - \phi_X}{\phi_J - \phi_X} \tag{4.2}$$

4.2.2 NO_x Normalization

The NO_x raw data at each measurement point $NO_{x,raw}$ is normalized to 15% O_2 standard condition, using the local equivalence ratio ϕ_{MP} calculated from equation 4.1 [62, 144].

$$NO_x = NO_{x,raw} \frac{v_{min} + l_{min}\left(\frac{1}{\phi_{MP}} - 1\right)}{v_{min,dry} + l_{min}\left(\frac{1}{\phi_{15}} - 1\right)}. \tag{4.3}$$

As the NO_x-measurements are taken from the wet exhaust gas, the minimum amount of exhaust gas before water condensation v_{min} is needed together with the equivalence ratio ϕ_{15} corresponding to 15% O_2. With equation 4.3, the standard normalized concentrations, i.e. dry exhaust gas at 15% O_2, are calculated. All measurements in this study are normalized according to this procedure and given in dry, volumetric parts per million (ppm).

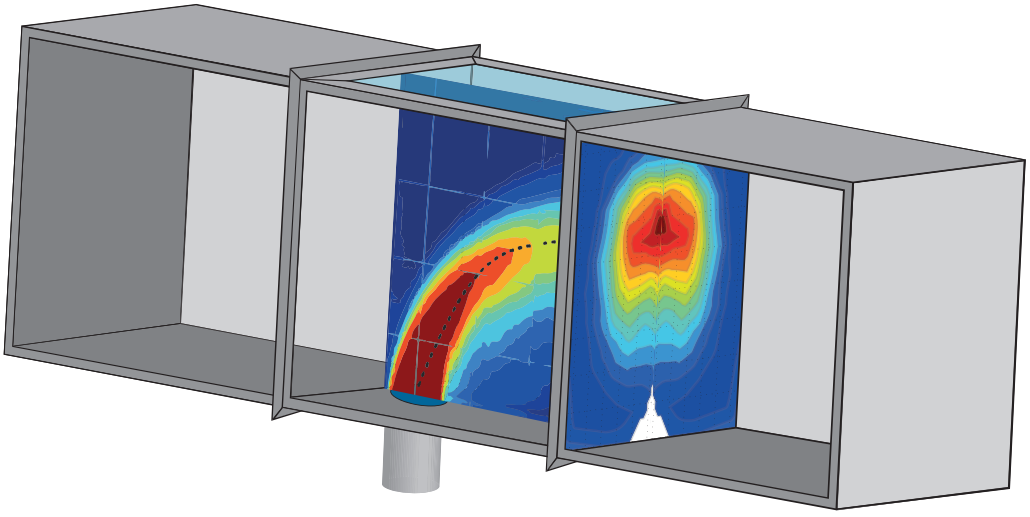

Figure 4.2: Experimental setup with the position of the laser sheet in the x-z center plane (showing an example of the mixture fraction field) and an example of NO_x-distribution in a plane perpendicular to the cross flow.

4.3 Particle Image Velocimetry

The velocity field of the non-reacting and reacting flow in the secondary combustion zone is analyzed by particle image velocimetry (PIV). Details on the PIV measurement technique can be found in [122]. For all measurements an ILA high-speed (10 kHz) PIV system with a

Nd:YLF laser (New Wave Pegasus) is used together with a CMOS camera (Photron SA5). The laser sheet is positioned in the x-z center plane of the cross flow at y=0, the camera is located perpendicular to it (for the position of the laser sheet see figure 4.2). With this setup, two velocity components in x- and z-direction (u and w) can be studied.

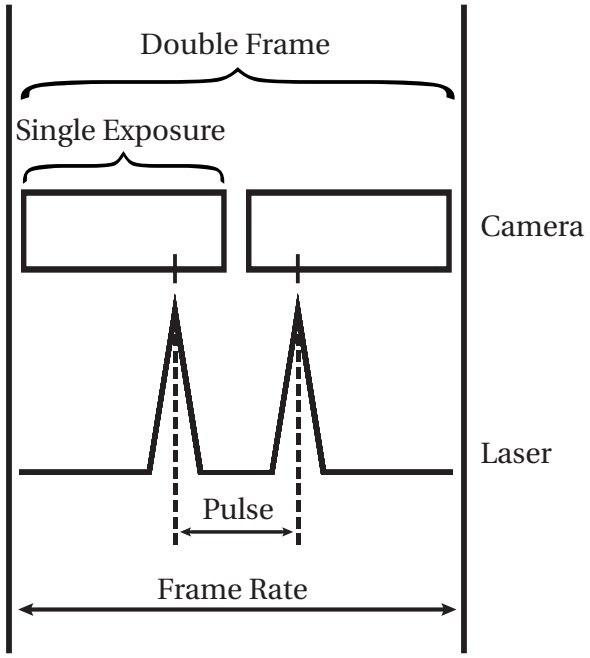

Figure 4.3: Synchronization of camera shutter and laser pulse for double frame single exposure PIV setup.

The used setup applies double frame single exposure, see figure 4.3. Each frame of a double frame is exposed to a single laser pulse. The seeding particles in the flow scatter the light of the laser sheet and the camera records the position of the tracers. The time difference between the two laser pulses are typically in the range of 10 to 100μs. The frame rate is the number of double frames per second. The velocity vectors are determined by tracking the displacement of the particles. For analysis, a conventional cross correlation algorithm is applied.
For each application, the appropriate seeding particle must be selected [97]. Typically used tracers in non-reacting flows are oil, smoke, or hollow glass spheres. The PIV method is based on the assumption that the particles follow the flow ideally. The ratio of acceleration forces to flow resistance must be as small as possible. In order to ensure that slip can be neglected, the particle is chosen to have a similar density as the sur-

rounding fluid. If this is not achievable, as in gaseous flows of high temperature, the tracer particle should be as small as possible [61, 97, 122]. Typically, in technical applications, the tracers follow the flow for turbulent frequencies up to 1000Hz [122] (see a calculation for the present setup [103]). In case of reacting flows, particles with a high melting point are needed. For the reacting and non-reacting jet in cross flow experiments, titanium dioxide TiO_2-particles have been chosen with a melting point above 2100K and a mean particle size around 1μm.

4.4 Mixture Field Analysis

For a detailed analysis of the mixture field, a new method providing a quantitative analysis of Mie scattering from seeding particles exposed to a laser pulse was developed (see [110] and [8] for discussion of different algorithms). The method depends on the correlation of the intensity of the scattered light with the mixture fraction f. The underlying idea can be found already in the early work of Stepowski [139] from 1988. A dissertation conducted at the German Aerospace Center in Cologne [147] deals with the application to non-reacting mixing flows. A similar approach is subject to recent research at Lund University [9, 79], using droplets instead of seeding particles.
As the setup is similar to PIV measurements the method is called MixPIV, in the following. However, only one of the two mixing flows is seeded with tracer particles (TiO_2). The laser sheet is positioned in the x-z center plane and the camera is located perpendicular to the cross flow, see also figure 4.2. The high-speed PIV laser system with a Nd:YLF laser and a CMOS camera is used.
The actual local mixture fraction f* is calculated following equation 4.4:

$$f^*(x,z,t) = \frac{I(x,z,t) - BG(x,z)}{I_{ref}(t)} LS(x,z) \frac{\rho_{ref}}{\rho}. \tag{4.4}$$

The measured intensity field of the scattered light in the x-z measurement plane I is corrected by subtracting interfering background light BG. Further, inhomogeneities in the laser sheet illumination LS are taken into account. The corrected intensity is normalized in every image (at

time t) by the intensity at a reference point I_{ref}. The reference point is an area of a few pixels near the jet outlet. At this point the mixture fraction is one, as it is known that the mixture only consists of jet material, see figure 4.5. Due to the high seeding density in this region, the highest intensity of scattered light is detected there. By normalizing to the reference intensity for every picture, laser pulse fluctuations and changing seeding densities are accounted for. Additionally, different densities of the reference point ρ_{ref} and the entrained fluid ρ can be considered, following the method presented in [133]. For an overview of the analysis procedure for the reacting and non-reacting case see the scheme in figure 4.4.
The analysis of the mixing field provides two-dimensional data of the mean field, as well as RMS values and probability density functions (PDF). With the calculation of the ideal mixture fraction f_{ideal}, assuming perfect mixing of both mass flows $\dot{m}_J$ and $\dot{m}_X$ (equation 2.54), the measured mixtures can be compared with the hypothetical ideal mixture in order to evaluate spatial and temporal mixing quality.

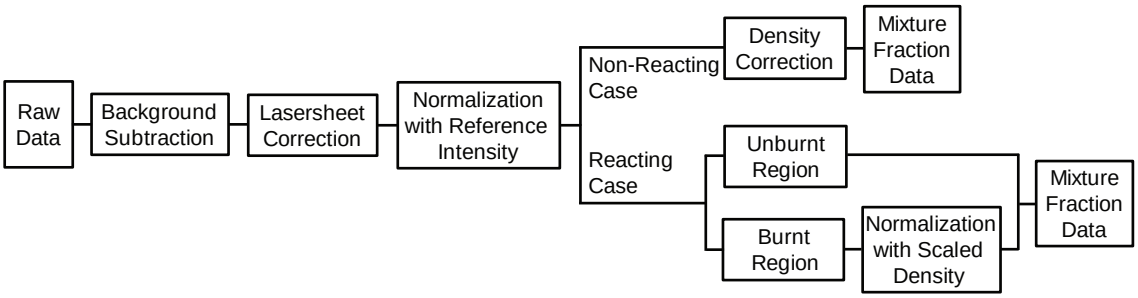

Figure 4.4: Analysis procedure of the MixPIV algorithm for reacting and non-reacting cases.

4.4.1 Validation With Temperature Measurements

The mean mixture field from the MixPIV algorithm can be checked against temperature measurements with a thermocouple (TC). The thermocouple is mounted on a traversal system and provides point-wise measurements of the three-dimensional temperature field (details given in [8, 77]). In the test setup, the jet was preheated to 393K. With the local measured mean temperature T and the given temperatures of the two mixing flows of cross flow T_X and jet T_J, the local mixture fraction f at

every x-y-z-coordinate is calculated following equation

$$f(x,y,z) = \frac{T(x,y,z) - T_X}{T_J - T_X}. \tag{4.5}$$

This validation method is restricted to non-reacting test cases. Only the mean mixture fields of the two methods can be compared. The values in the x-z center plane are in good agreement with each other, i.e. the deviation in every point is below 5% [77].

4.4.2 Application to Cases with Varying Fluid Densities

The MixPIV algorithm as described in equation 4.4 can only be applied to isothermal flows. The two mixing flows may have different, but constant densities. This assumption does not hold for reacting flows, as the density changes instantaneously at the flame front due to the steep temperature gradient over the reaction zone. In the analysis procedure for reacting cases, a two-step algorithm must be applied for pre-flame and post-flame mixing, separated by the flame front.

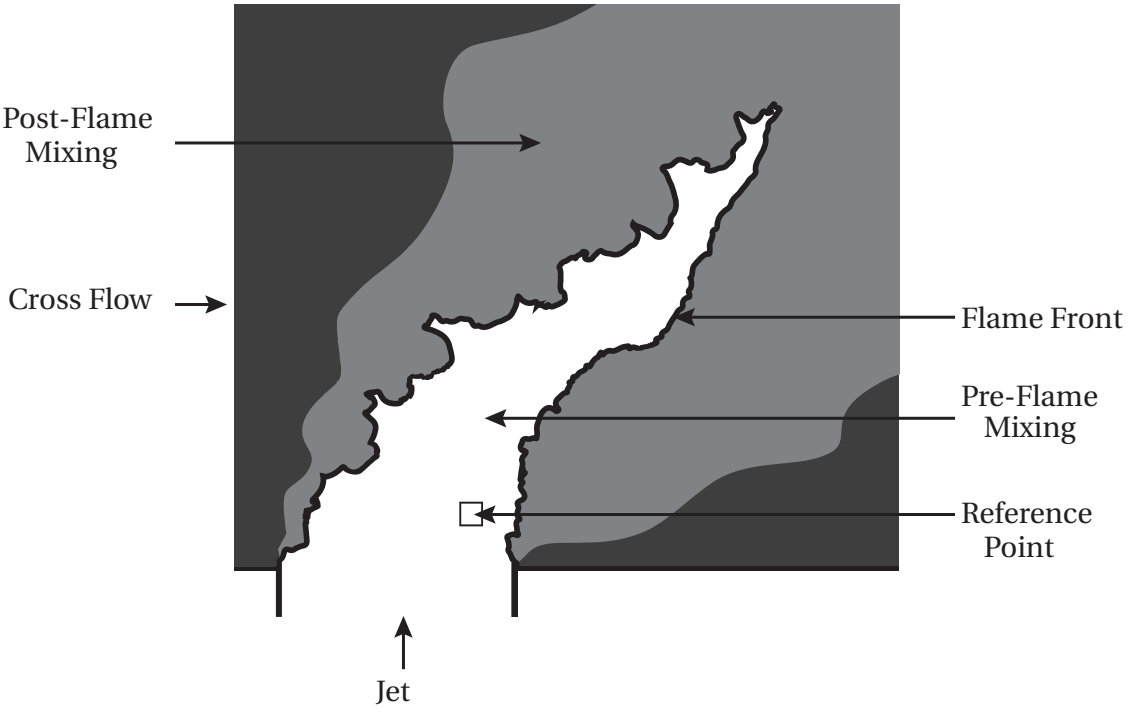

Figure 4.5: Scheme illustrating flame front detection and pre- and post-flame mixing.

The basic idea of the algorithm for reacting cases is illustrated by the schematic drawing of an instantaneous image of a reacting jet in hot cross flow shown in figure 4.5. Different zones can be distinguished: The core of the jet is characterized by high seeding density, i.e. no mixing and no reaction has taken place so far. A second zone is separated from the first zone by a distinct step in seeding concentration. This zone consists of a mixture of reactants of the jet and burnt cross flow. The position of the flame front is between these two zones. As the cross flow is not seeded, a third zone, where no particles can be detected, consists of pure cross flow material. However, there is a clearly visible mixing zone between the cross flow and the reactants of the jet in the shear layers and the wake region of the jet. The seeding density shows a distinct step over the flame front, which is not due to mixing processes, but must be attributed to a sudden combustion induced fluid expansion.
Figure 4.4 also shows the analysis procedure for reacting test cases. The density correction is split into two parts. The first part determines the pre-flame mixing of the unburnt jet with the cross flow. The second part accounts for the entrainment of cross flow into the jet products, i.e. post-flame mixing. The two algorithms use different densities of the mixing fluids (last quotient in equation 4.4). The reference intensity must be adapted to the post-flame density level.
Crucial for the procedure is the correct detection of the flame front. The position of the flame is visible by the instantaneous change in seeding density over the flame front (a similar idea to detect the flame front in PIV data is given e.g. in [142]). The flame front itself cannot be resolved, as typical flame front thickness is smaller than the resolution of the MixPIV data. The algorithm of the flame front detection includes methods from the MatLab Image Processing Toolbox, e.g. edge detection or histogram analysis [138].
This method is applicable only to the anchored flame, where the flame front is clearly detectable in the data. For the lifted jet with the smaller diameter, a separation of the pre- and post-flame region is not possible. Thus, no quantitative analysis of the mixture field data is available for these operating points. However, the MixPIV data can be used for a qualitative analysis, e.g. for detection of the mixture trajectory even for lifted flames.

5 NO_X Reduction Potential of Staged Combustion

In this chapter, the theoretical NO_x-reduction potential of a staged jet in cross flow configuration is studied numerically with simplified chemical models. The theoretical case of perfectly premixing of fuel and air prior to combustion is discussed. The case of higher NO_x-formation due to unmixedness and additional air admixing along the combustor is studied in chapter 7. Single-stage combustion at the overall equivalence ratio ϕ_{tot} is used as reference case. The comparisons are based on the same combustor exit temperature. All simulations are run at 1bar and at elevated pressure of 20bar, i.e. gas turbine combustion pressure.
Although the real topology of flame fronts at high turbulence levels is complicated [23], one-dimensional laminar flame calculations with detailed chemistry are in acceptable agreement with experimental data regarding NO_x-formation [113, 132]. In the following, such models are employed to simulate NO_x-formation. This method requires a mapping of the three-dimensional temperature field to a one-dimensional adiabatic model and thus a massive simplification concerning the fluid dynamics. Hence, these results are seen as an indicator of the theoretical potential of the staged configuration.

5.1 Model Setup

In the following, the two asymptotic cases of no and of infinitely fast mixing of the jet material with the hot cross flow are investigated and compared with single stage combustion at the same turbine inlet temperature. In the unstaged case used as reference case the reactants of the cross flow and the jet are mixed together and then burnt in a single one-dimensional freely propagating flame, see top line in figure 5.1. The worst case model with no mixing is shown in the center of figure 5.1. After full burn out, both flows are mixed together at the combustor

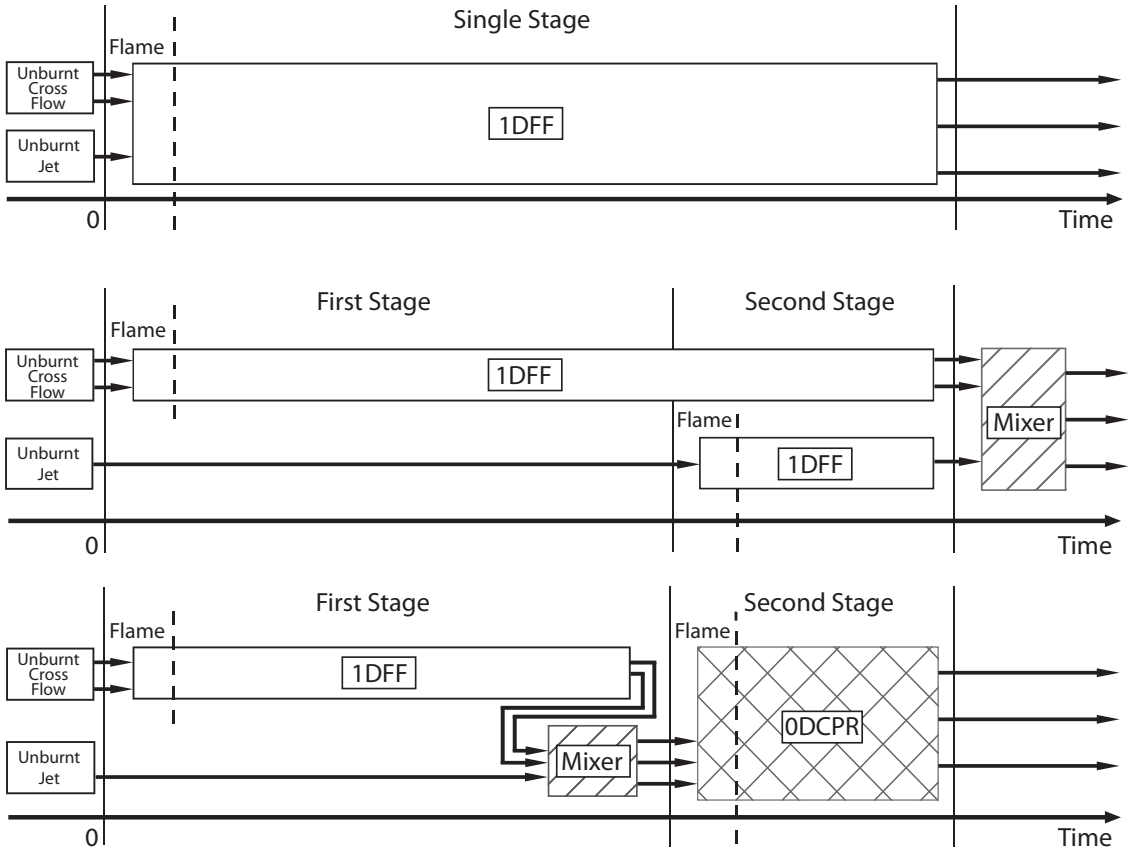

Figure 5.1: Chemical models for NO_x reduction potential simulations: First model is the single stage reference case, the two other models represent the worst and best case scenarios of the two-staged configuration.

end according to the mass split ratio (see chapter 3) and analyzed afterwards. The model for the best case, with full mixing of the jet with the cross flow before ignition, is shown at the bottom of figure 5.1. Both flows are mixed first. The resulting composition is used as initial condition for the succeeding CPR. The NO_x-concentrations for all three scenarios are evaluated at the same total combustor residence time.

Table 5.1: Parameters of the chosen test cases.

T_{in} [K]	ϕ_X	ϕ_J	ϕ_{tot}	T_{ad} [K]	msr [%]
673	0.5	0.5	0.5	1750	0-50
673	0.5	0.66	0.5177	1780	11
673	0.5	0.77	0.5296	1800	11

In the following study, three different test cases are discussed, see table 5.1. As a starting point, the simple case with the same equivalence ratio in the jet and the cross flow is investigated. Furthermore, the results of simulations with two different equivalence ratios of the jet, i.e. ϕ_J=0.66 and 0.77, are presented in more detail. For all cases, the cross flow equivalence ratio is held constant at ϕ_X=0.5. Following table 5.1, this results in an overall equivalence ratio of ϕ_{tot}=0.5177 and 0.5296 with an adiabatic flame temperature of T_{ad}=1780 and 1800K, respectively. This temperature corresponds to a mass split ratio, where 11% of the total mass flow is injected in the secondary stage. In all cases considered, the incoming flows of the jet and the cross flow are preheated to 673K. For better comparison with the high pressure case, all figures in the following are normalized by the total residence time in the combustor, i.e. τ_{cc}=1 at the end of the combustor. Due to scaling reasons, the atmospheric test rig has lower velocities and longer residence times, see section 3.2. In the following, simulations of high pressure conditions of 20bar were run at five times shorter residence times. In all calculations, natural gas is used as fuel.

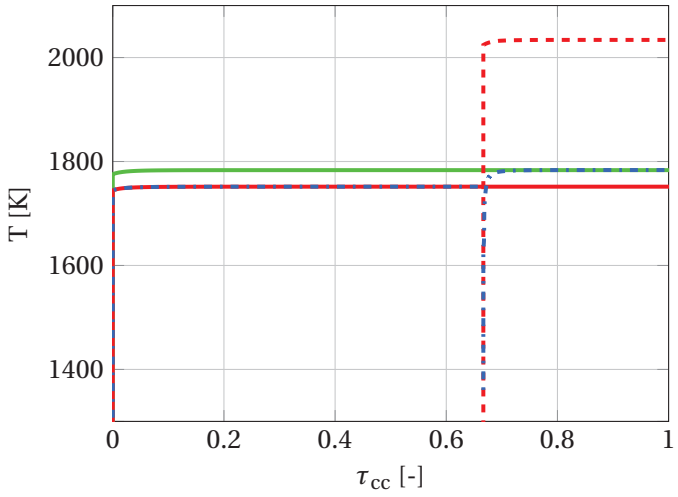

Figure 5.2: Temperature profiles for single stage (green), and best (blue) and worst case (jet dashed red line, cross flow red line) of the staged configuration at ϕ_J=0.66, overall T_{ad}=1780K.

The differences between the asymptotic models and the single stage reference case of figure 5.1 can be explained best by considering the temperature profiles shown in figure 5.2. In the single stage case, the final temperature is the adiabatic flame temperature, i.e. 1780K in the case

of ϕ_J=0.66 (corresponding to an overall equivalence ratio of ϕ_{tot}=0.5177, see table 5.1). As there is no additional jet injection in the single stage case, the temperature is constant over the entire post-flame residence time within the combustor (shown by the constant green line in figure 5.2). Furthermore, this temperature serves as reference corresponding to the same overall equivalence ratio ϕ_{tot}.
The red and the blue lines in figure 5.2 represent the two cases with jet injection at 2/3 of the total residence time. For the staged configuration, the model is divided into two parts resulting in two different temperatures. The first stage is fired with a lower equivalence ratio, resulting in a lower adiabatic flame temperature (blue/red dashed line in figure 5.2). In the second stage, the temperature is different for the best and worst case. For both asymptotic cases the jet reactants are preheated to 673K. In the best case (blue dashed line in figure 5.2), the jet of 673K is first mixed with the cross flow of 1750K resulting in a mixture temperature of approximately 1630K for the given mass split ratio of 11%. This mixture is then burnt with the same adiabatic flame temperature as in the single stage case. Thus, the final temperature represented by the green line is reached immediately upon jet injection and stays constant until it reaches the end of the combustor. However, as in the worst case the jet burns independently from the cross flow, two different burning temperatures are present in the second stage. The jet of 673K is injected and burns at a higher adiabatic flame temperature (red dashed line in figure 5.2), whereas the temperature of the model for the cross flow stays at the low temperature (red line in figure 5.2). At the end of the combustor, both flows are mixed together. The mixed temperature at the end of the combustor is not shown in figure 5.2 for the staged worst case (red lines). With the selected mass split ratio of 11% the same overall end temperature is reached.

5.2 Staging Potential

As a starting point, the configuration when both stages are fired at the same equivalence ratio is investigated. In this configuration the advantage of staging lies in the shorter residence time of the jet flow and the resulting lower NO_x-concentration. The position of the jet injection is

fixed at 2/3 of the total combustor residence time τ_{cc} resulting in a lower residence time in the second stage of 1/3 τ_{cc}. The influencing parameter is the mass split ratio msr between jet and cross flow.

Table 5.2: NO_x-concentrations of the ϕ=0.5 laminar freely propagating flame at different post-flame residence times.

	@1/3τ_{cc}	@ τ_{cc}
1bar	3.0ppm	3.8ppm
20bar	1.4ppm	2.2ppm

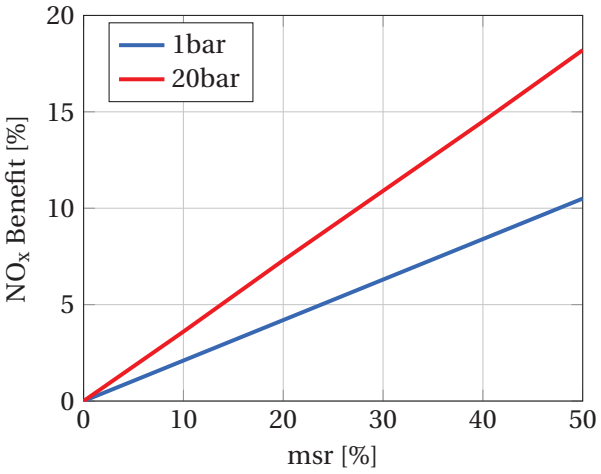

Figure 5.3: Relative NO_x-benefit of staging over mass split ratio at 1 and 20bar.

Table 5.2 shows the NO_x-results of a laminar free flame simulation at an equivalence ratio of ϕ=0.5. The normalized NO_x-concentrations are shown for two different residence times: The NO_x formed in the second stage over a residence time of 1/3 τ_{cc}, and overall NO_x formed over the total residence time in the combustor τ_{cc}. The results reveal the advantage of the shorter residence time in the second stage on NO_x. Figure 5.3 illustrates the influence of mass split ratio on the relative NO_x benefit. An increased mass flow in the second stage corresponds to a higher mass split ratio. Under the assumption of perfect premixing in both stages, there is a linear increase of the theoretical NO_x benefit compared to the single stage case at 1 and 20bar. However, the relative NO_x benefit is higher for the 20bar test case originating from the higher influence of post flame NO_x-formation.

In conclusion, it is favorable, to inject the secondary jet flow as late as possible and to increase the mass flow ratio of the jet. On the other side, if the injection of the jet is too far downstream, the burnout of the flame is not finished or CO is not yet in thermal equilibrium. Flame burn-out can play a role in technical applications, but was not considered in the presented model.
As it was shown, there is a theoretical NO_x reduction potential for the staged jet in cross flow configuration with same equivalence ratios of the jet and the cross flow. In the following, the two other test cases with a higher equivalence ratio in the second stage are studied, using the chemical models from figure 5.1. In this configuration, staging results in a higher thermal output, i.e. higher turbine inlet temperature, without changing the equivalence ratio of the first stage. The overall power can be controlled by changing the jet fuel flow only. The results of the best and worst case simulations are again compared to the NO_x-concentration of the single stage reference case of a freely propagating flame with the same adiabatic flame temperature (see table 5.1).
Figures 5.4 and 5.5 summarize the NO_x-results of the chemical modeling. For both jet equivalence ratios of ϕ_J=0.66 and 0.77 the best case shows a reduction potential for ambient pressure as well as for the 20bar case. The key to lower NO_x again lies in the shorter residence time in the second combustion zone. Additionally, the cross flow is fired at a lower temperature also resulting in lower NO_x. The potential is higher with an increased jet equivalence ratio. The higher equivalence ratio of the jet does not promote NO_x-formation, because perfect mixing prior to ignition has been assumed. This behavior is different for the worst case of no mixing between jet and cross flow. With staging, the NO_x-concentrations are by far highest, although the residence time in the second stage is short.
In addition, figures 5.4 and 5.5 show the differences of in-flame and post-flame NO_x-formation under atmospheric and 20bar conditions: At high pressure, the overall NO_x-concentrations are lower due to the lower total residence time in the combustor. The in-flame NO_x-formation is of minor importance and the post-flame NO_x is becoming dominant. In the present configuration with its specific scaling to high pressure, the thermal NO_x-formation is approximately the same for the 1bar and 20bar case. The level of mixing of the hot jet products with the cross

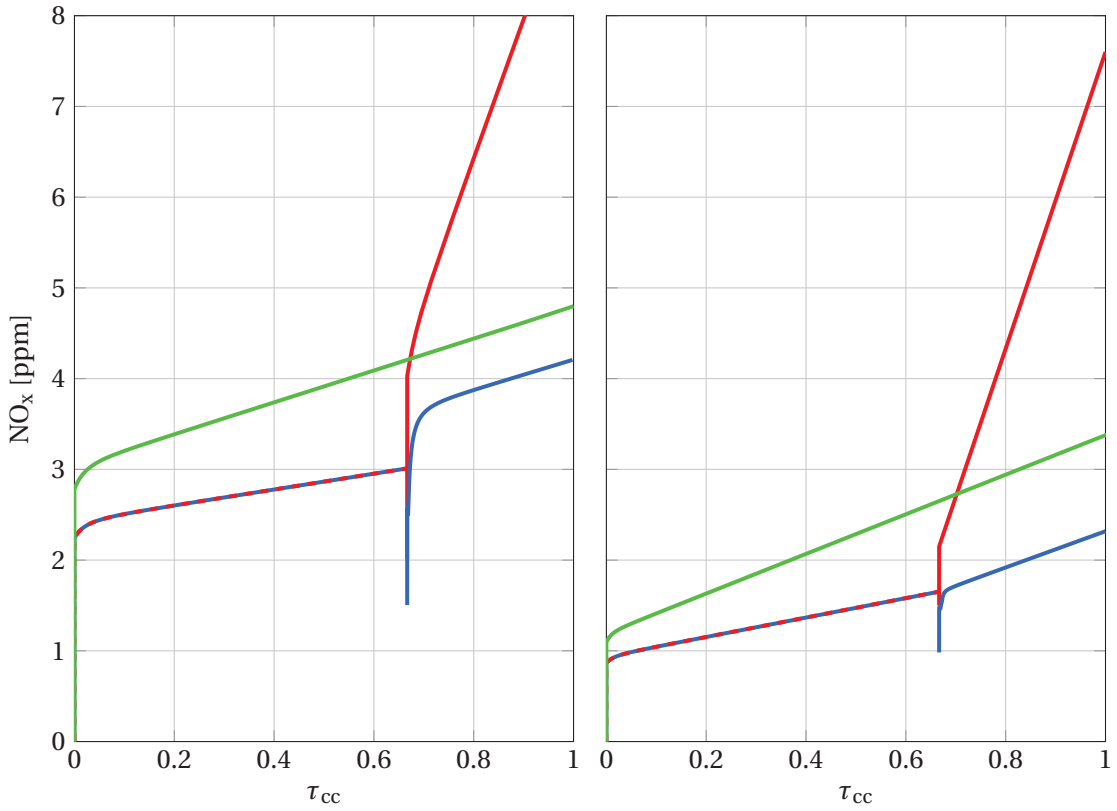

Figure 5.4: Calculated NO_x-concentrations at ambient pressure (left) and 20 bar (right) for single stage (green), and best (blue) and worst case (red) of the staged configuration at ϕ_J=0.66 .

flow is decisive for the NO_x reduction potential of staging. In addition, post-flame NO_x-formation is prevailing under high pressure resulting in a stronger influence of the mixing between jet and cross flow for the 20 bar case and a larger reduction potential. These modeling results show that staged combustion requires a high degree of mixing prior to ignition of the secondary fuel-air jet flow. Also in the case with higher equivalence ratio in the second stage, the NO_x reduction potential originates entirely from the lower residence time in the second stage.

Table 5.3: NO_x-results of the potential analysis at 1 and 20bar: single stage reference case and best case of staged combustion.

			reference case		best case	
ϕ_X	ϕ_J	ϕ_{tot}	1bar	20bar	1bar	20bar
0.5	0.66	0.5177	4.8ppm	3.4ppm	4.2ppm	2.3ppm
0.5	0.77	0.5296	6.1ppm	4.5ppm	4.7ppm	2.6ppm

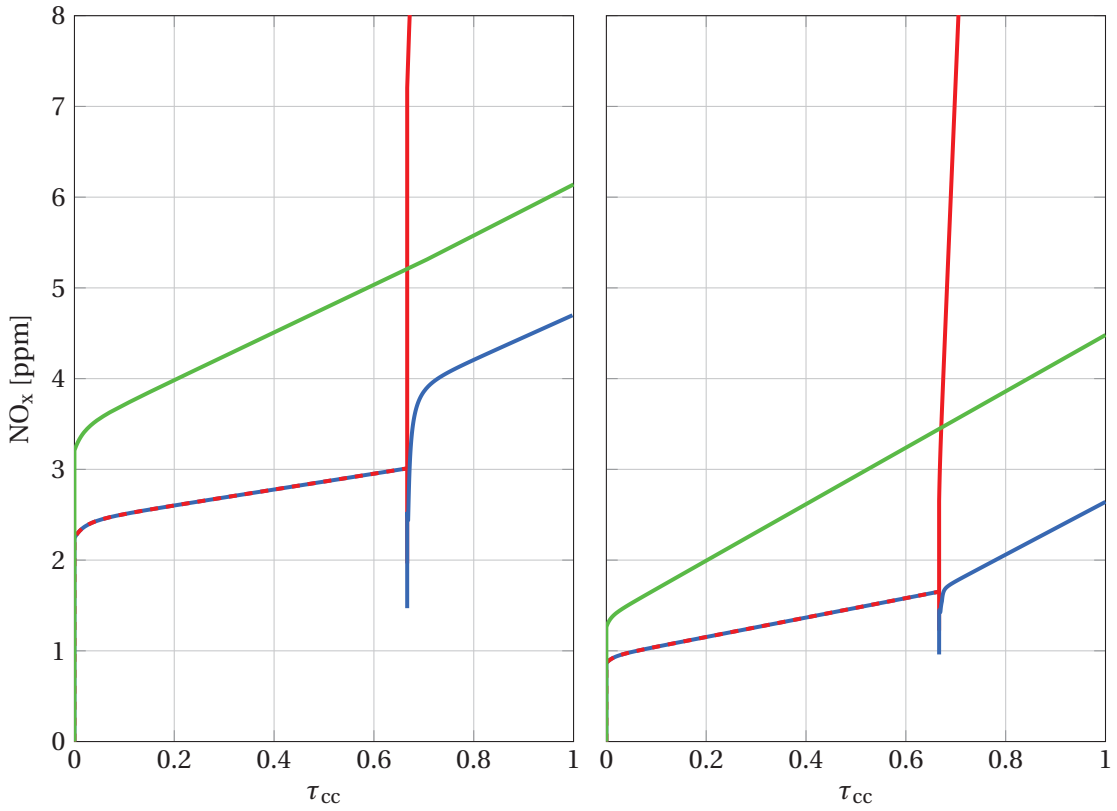

Figure 5.5: Calculated NO_x-concentrations at ambient pressure (left) and 20 bar (right) for single stage (green), and best (blue) and worst case (red) of the staged configuration at ϕ_J=0.77.

Table 5.3 shows the NO_x-results of chemical reactor modeling of the single stage reference case and the best case of staged combustion for the two jet equivalence ratios (ϕ_J=0.66 and 0.77) at atmospheric and 20bar conditions. In conclusion, a NO_x reduction potential exists for atmospheric as well as engine conditions. At high pressure, staged combustion is even more promising than for the atmospheric case. Thus, lab scale experiments underestimate the effect of staging on the NO_x reduction potential. In absolute numbers, reactor modeling indicates that the maximum theoretical reduction is in the range of 1-2ppm assuming perfectly premixed reactants in both stages.
However, the exploitation of the reduction potential requires a high level of mixing prior to ignition. The main challenge is to delay ignition of the jet mixture, which is exposed to the hot products of the first stage. The best case of perfect mixing of jet and cross flow before ignition is technically not feasible. Two different flame types of anchored and lifted

flames are discussed in the following chapter 6. Detaching the jet flame from the circumference of the injector augments the pre-flame mixture and also decreases NO_x-formation. The influences of pre-flame and post-flame mixing, as well as residence time on in-flame and post-flame NO_x-formation, is studied in detail with a chemical network model in chapter 7. It is further discussed if and how a beneficial application of staged combustion in terms of overall NO_x-reduction is technically achievable, especially at high pressure gas turbine conditions. Chapter 7 also deals with the impact of higher NO_x-levels in state of the art gas turbine combustors on staged combustion NO_x reduction potential. Temporal and spatial unmixedness and air addition along the combustor liner result in a higher effective flame temperature in the first combustion zone, which leads to higher NO_x-formation rates.

6 Experimental Results

In this chapter, the experimental findings obtained with the atmospheric test rig are discussed. In the first part, the experimental results of the upscaled injector of 100mm diameter are presented in detail. Momentum ratios between 4≤J≤10 are chosen as this range is relevant for gas turbine combustors. Due to the large diameter and the resulting high spatial resolution of the experimental data, the measurements are suitable for a detailed analysis of the velocity and mixture field and its influence on NO_x formation. The second part of the chapter focuses on the investigation of the lifted jet flame with 15mm diameter. The data of the lifted flame is further needed for the validation of the chemical network model in chapter 7.

6.1 Anchored Flames

Reacting tests of the jet scaled by ignition delay Damköhler number Da_{ign} are performed (see section 3.3). For all operating points in this section an anchored flame is detected. The non-reacting velocity field of the 100mm diameter jet injector is investigated and compared to the velocity field of the reacting operating points.

6.1.1 Flame Shape and Stabilization

The flame shape and stabilization is discussed by studying experimental data of OH* chemiluminescence and reacting velocity fields in the center plane.

6.1.1.1 Flame Characterization by OH* Chemiluminescence

A sensitivity study is conducted in order to investigate the influences of the jet equivalence ratio ϕ_J and the momentum ratio J on flame shape and flame length. The momentum ratio is varied between 4≤J≤10, and the equivalence ratio is studied between $0.05 \leq \phi_J \leq 0.77$.

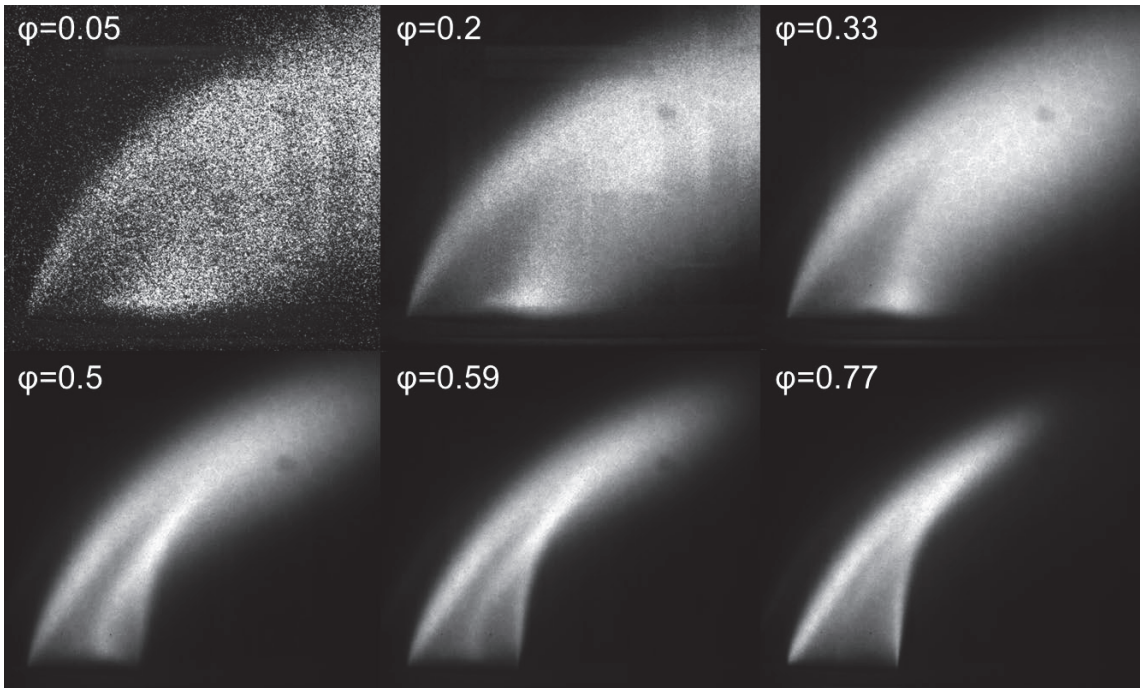

Figure 6.1: Mean OH* image of the flame in side view for J=6 at equivalence ratio of $0.05 \leq \phi_J \leq 0.77$.

Figure 6.1 shows the influence of jet equivalence ratio for a momentum ratio of J=6 in side view. As the flames of the operating points given in figure 6.1 are recorded at different gains and normalized to maximum intensity of each picture, the absolute intensities are not comparable with each other. Even for very lean mixtures of ϕ_J=0.05, the flame is stabilized at the circumference of the jet injector. For higher equivalence ratios (ϕ_J>0.77), the flame stabilizes inside the injector, but only at the upstream side. This behavior can be explained by the vortex system: The horseshoe vortex allows the hot cross flow material to penetrate the injector pipe as explained in section 2.1.3. Inside the pipe, the highly reactive mixture ignites instantaneously. As with increasing equivalence ratio and increasing flame temperature the quenching distance decreases the flame is able to propagate into the pipe. The flame shapes of the different equivalence ratios are similar within the range of the studied momentum ratios ($4 \leq J \leq 10$).

Figure 6.2 shows the side and the top view of a J=8 flame at two different equivalence ratios of ϕ_J=0.77 (left) and ϕ_J=0.33 (right). Both views together give an idea of the three-dimensional shape of the flame. On the left side of figure 6.2, as a typical example of high equivalence ra-

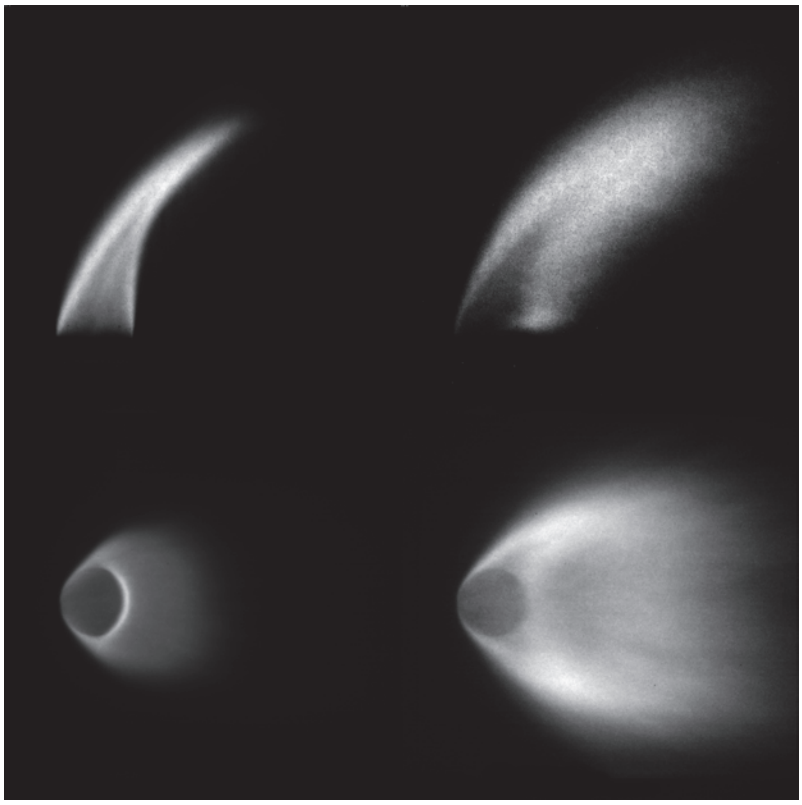

Figure 6.2: Mean OH* image in side (top) and top (bottom) view of the J=8 flame at equivalence ratio ϕ_J=0.77 (left) and ϕ_J=0.33 (right).

tio ($\phi_J \geq 0.5$), the flame has sharp boundaries and burns out very quickly. Further downstream, when the jet is bend in direction of the cross flow, the flame is very thin and flat, see top left picture of figure 6.2. With less reactive mixture, i.e. lower equivalence ratios, the flame is longer and due to the fluctuating position of the flame the contours are blurred (see second column of figure 6.2).

In figure 6.3 and 6.4, the intensity profiles at x/D=1.5 are compared regarding penetration depth and flame position. In order to be able to compare records of different gains of the image intensifier, all mean intensity signals are corrected and normalized by the highest intensity at J=10 and ϕ_J=0.77. Figure 6.3 shows the influence of the momentum ratio at constant equivalence ratio of the jet at ϕ_J=0.5. As expected, the maximum is shifted to higher z/D positions with increasing momentum ratio J. However, the shapes of the intensity profiles are similar for all momentum ratios independent of the equivalence ratio.

In figure 6.4, the intensity profiles of different equivalence ratios, $0.1 \leq \phi_J \leq 0.77$, at a momentum ratio of J=10 are compared with each

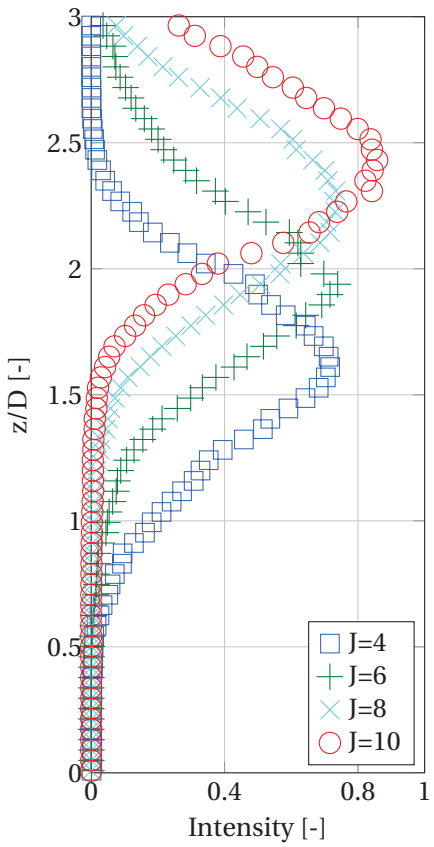

Figure 6.3: Intensity profile of mean OH* images at x/D=1.5 for momentum ratio 4≤J≤10 at jet equivalence ratio ϕ_J=0.5.

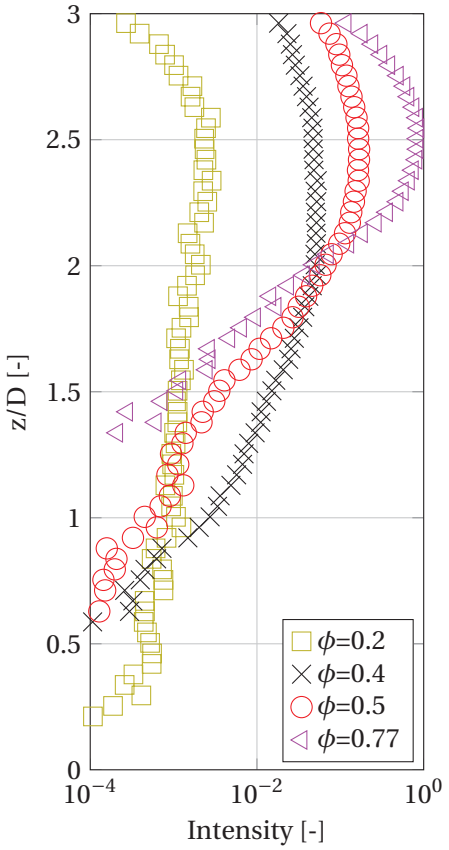

Figure 6.4: Intensity profile of mean OH* images at x/D=1.5 for jet equivalence ratio 0.05≤ϕ≤0.77 at momentum ratio J=10.

other. The intensity profiles at x/D=1.5 show a wider distribution with decreasing equivalence ratio. In contrast to the distinct intensity maximum for the high equivalence ratio of ϕ_J=0.77, the profile for ϕ_J=0.2 spreads over almost the complete height. By studying the J=8 flame (see the top view in figure 6.2), it is revealed that at equivalence ratio ϕ_J=0.33 the flame is also expanded in y-direction to the same extend. As OH* records provide line of sight integrated images, the OH* data is not adequate to determine the exact position of the local reaction zone.

6.1.1.2 Velocity Field in the Center Plane

Particle Image Velocimetry (PIV) measurements are taken in order to analyze the velocity field in the x-z center plane at y=0. First, the results of the non-reacting experiments are discussed. The momentum ratio is

varied within the characteristic range of 1≤J≤15. In accordance with literature, two different flow patterns in the mean velocity fields are distinguished depending on momentum ratio.

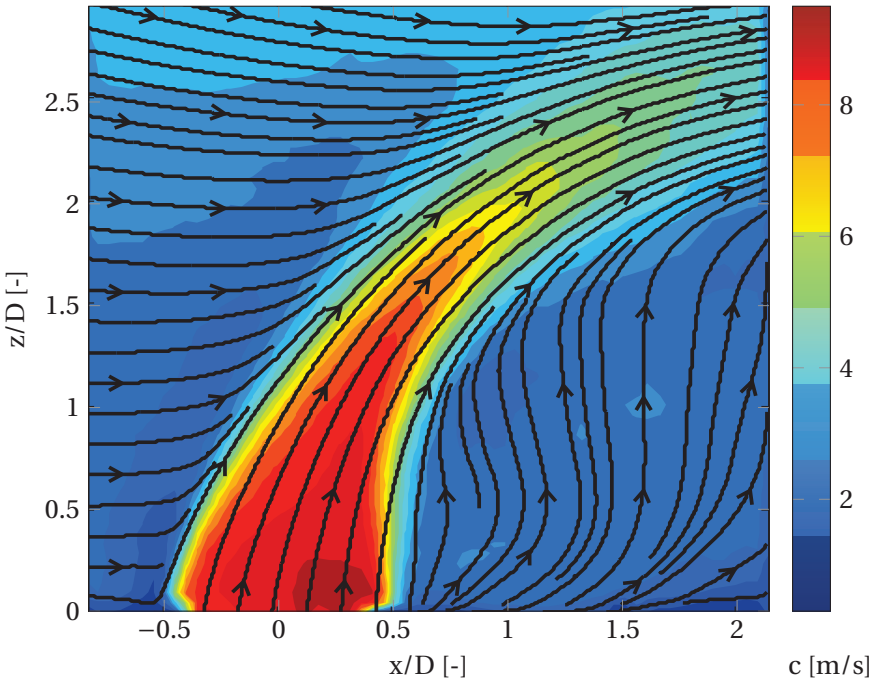

Figure 6.5: Mean velocity field with streamlines of the non-reacting jet at high momentum ratio J=10.

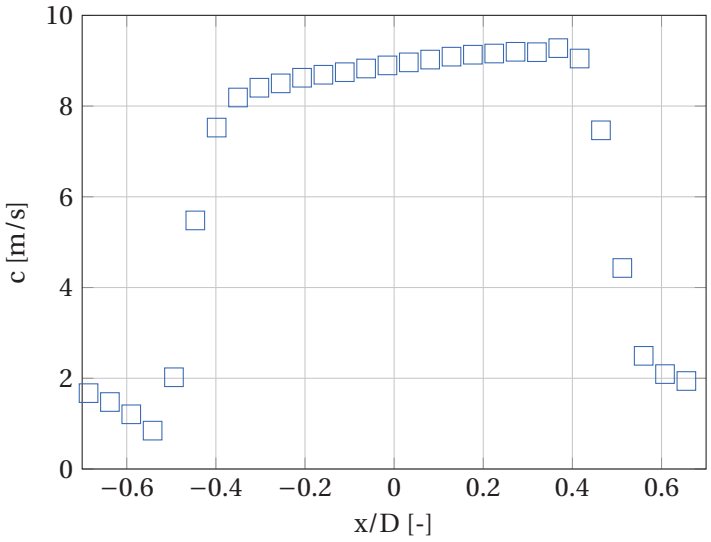

Figure 6.6: Mean velocity profile at jet outlet z/D=0.1 of the non-reacting jet at momentum ratio J=10.

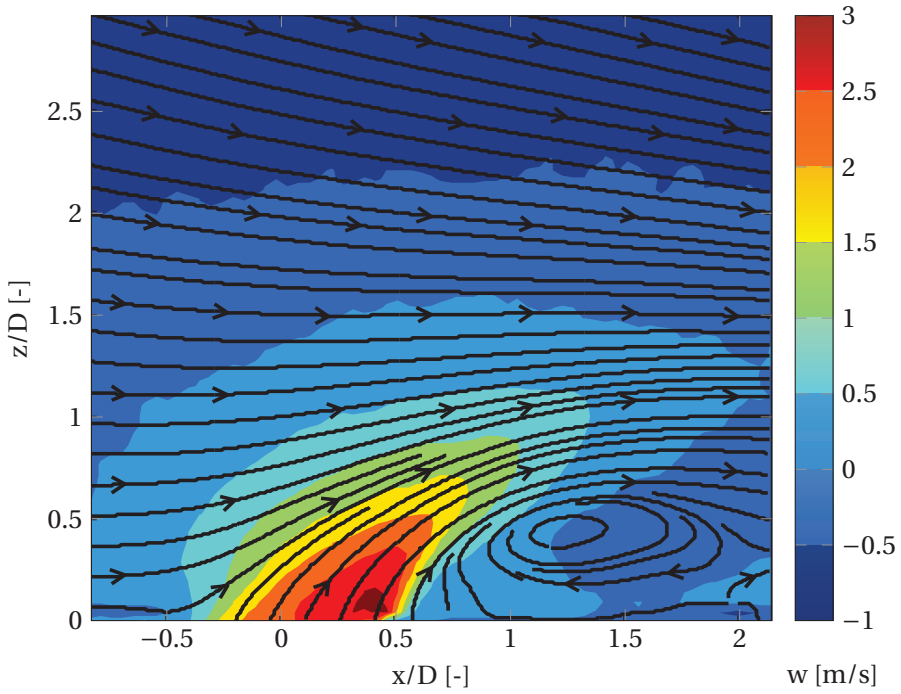

Figure 6.7: Mean velocity field with streamlines of the non-reacting jet at low momentum ratio J=1.

As an example for high momentum ratio, figure 6.5 depicts the mean velocity field of the non-reacting jet in cross flow at J=10. According to literature, the flow pattern with the upward streamlines in the wake region is characteristic for momentum ratios higher than 2 [42], see additional experimental results in figure A.2. However, more detailed structures – like the horseshoe vortex in the boundary layer near the circumference (see figure 2.4 and 2.5) – are not detectable in the data, as the resolution near the wall is too low. The absolute velocity magnitude c in x- and z-direction, i.e. $c=\sqrt{u^2+w^2}$, shows its maximum at the jet outlet and is decreasing along the jet trajectory. Due to the influence of the cross flow, the maximum velocity is shifted downstream. Figure 6.6 shows the velocity profile of the non-reacting jet at momentum ratio J=10 immediately above the jet outlet at z/D=0.1. The maximum velocity is located at x/D≈0.35. Similar velocity distributions are observed for all examined momentum ratios between 1≤J≤15.
An example of the flow field of the low momentum ratio jet with J=1 is shown in figure 6.7. Due to the low velocity, the jet is hardly penetrating the cross flow. The resulting streamlines of the mean velocity field show the typical clockwise rotating pattern in the wake.

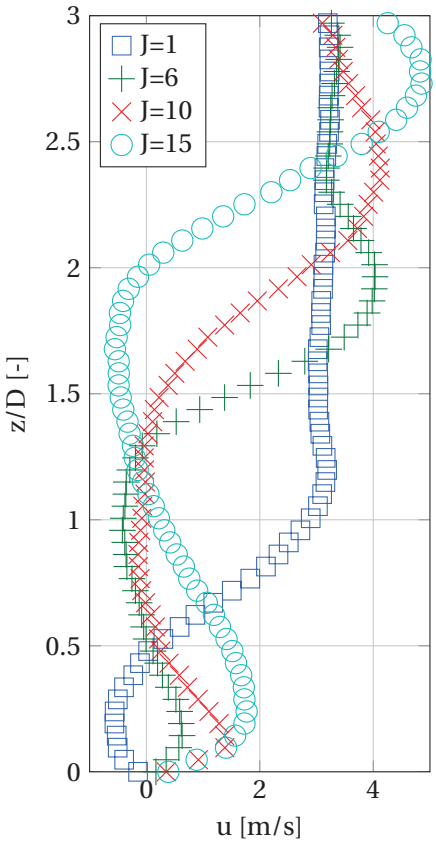

Figure 6.8: Mean profiles of the axial velocity component at x/D=1.5 for J=1,6,10 and 15. Note the negative velocity in the z/D<0.5 region at J=1.

To compare the penetration depth of the different non-reacting jets investigated, figure 6.8 depicts the velocity profile in x-direction at x/D=1.5 for momentum ratios between 1≤J≤15. The maximum velocity u is shifted to a higher z/D position with increasing momentum ratio. There is no significant maximum for the momentum ratio of J=1 at x/D=1.5. The recirculating flow of the J=1 jet is revealed in the lower part of the profile in figure 6.8. At z/D<0.5, reverse flow near the wall is visible.
In section 2.2.1, the turbulence intensity is calculated with the RMS_c-value of the velocity fluctuations, see equations 2.9 and 2.10. The RMS_c-value includes fluctuations u' and w' in the x-z center plane. For better comparison of different velocities, the RMS_c-values are normalized by the mean jet velocity U_J. As an example, figure 6.9 depicts the turbulence intensities Tu of the non-reacting jet at momentum ratio J=10, see additional experimental results in figure A.2. The turbulence is evolving in the shear layer similar to a free jet and reaches its maximum where the

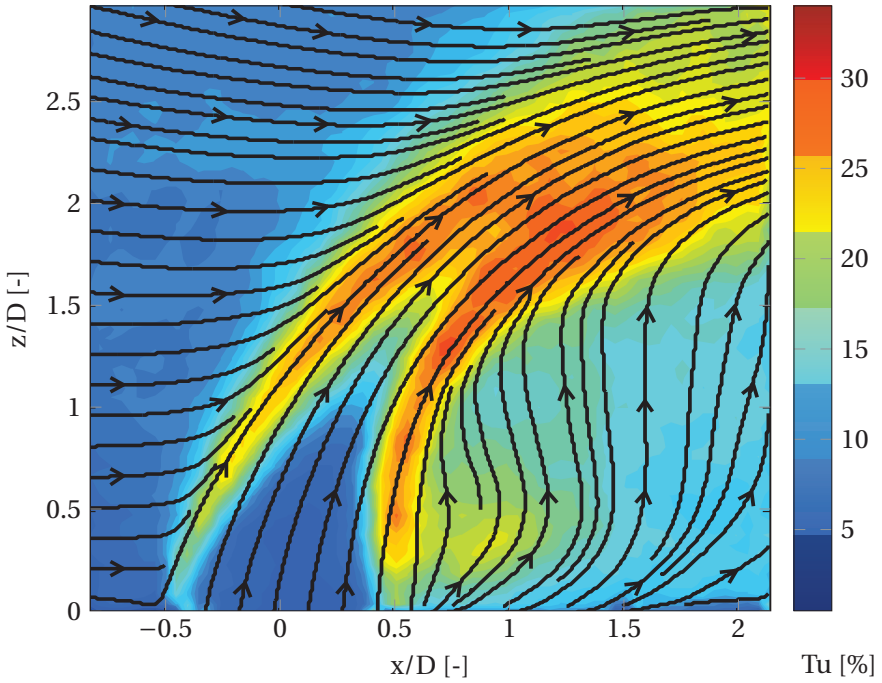

Figure 6.9: Mean turbulence intensities with streamlines of the non-reacting jet at momentum ratio J=10.

windward and lee side shear layers meet and the inner core of low turbulence vanishes. The maximum value of the turbulence intensities for all momentum ratios lies around 25 to 30%. Also the wake region is characterized by a relatively high turbulence of 10-30% (see figure A.2). However, the turbulence intensity in the wake region decreases with higher momentum ratio resulting in a poorer mixing for higher momentum ratios in the wake region behind the jet.

To get an understanding of the flow of the reacting jet and on how the additional heat release influences the velocity field, PIV measurements are conducted similarly to the non-reacting case. For all tests the laser sheet is at the same position as described for the non-reacting jet, i.e. in the x-z center plane at y=0. Figure 6.10 shows the mean velocity field of the reacting jet at momentum ratio J=10 and jet equivalence ratio ϕ_J=0.5, see additional experimental results in figure A.1. Due to strong light reflections, it is only possible to derive velocity vectors as close as approximately z/D=0.25 to the wall. In comparison to the tests without reaction, the jet penetrates deeper into the cross flow as the jet obtains an additional momentum from the gas expansion due to the reaction.

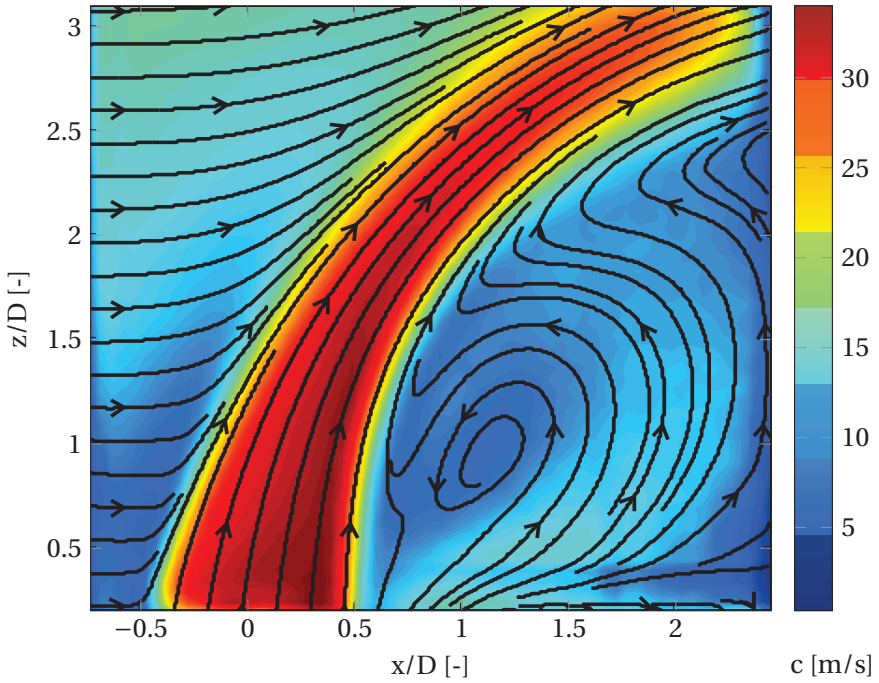

Figure 6.10: Mean velocity field with streamlines of the reacting jet at momentum ratio J=10 and jet equivalence ratio ϕ_J=0.5.

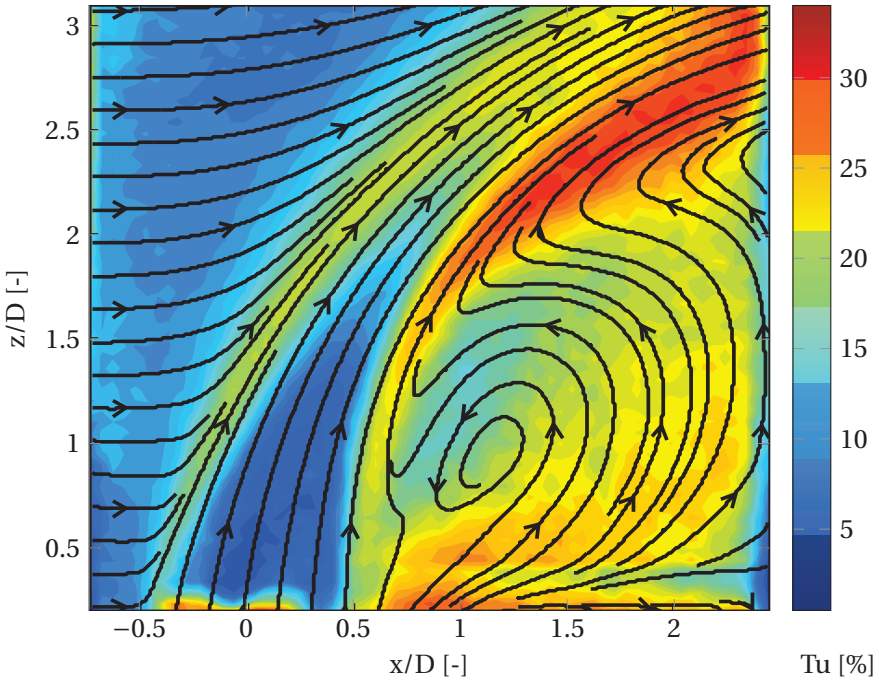

Figure 6.11: Mean turbulence intensities with streamlines of the reacting jet at momentum ratio J=10 and jet equivalence ratio ϕ_J=0.5.

As shown in figure 6.10, the mean velocity field shows a strong recirculation flow behind the jet for jet equivalence ratios ϕ_J=0.5 and higher.

This recirculating flow of the reacting velocity field is rotating counterclockwise in contrast to the clockwise rotating flow field pattern in the wake behind the jet for experiments without reaction at low momentum ratio, i.e. J<2. With leaner mixtures at jet equivalence ratios around $\phi_J \leq 0.4$, the recirculation zone in the wake region breaks down and the flow fields exhibit the typical upward streamlines as known from the test case without reaction. The core of the jet with its high velocity does not have the typical triangular shape known from the experiments without reaction (see figure 6.15). The region of high momentum is broader and longer.
Similarly to the test cases without reaction, the turbulence intensities are calculated with equations 2.9 and 2.10. As an example, figure 6.11 presents the results of the J=10 jet at equivalence ratio ϕ_J=0.5. In the jet region the turbulence is of the same level as in the case without reaction, i.e. approximately 30%. In the wake region the turbulence varies between 20 to 25% (see addition experimental results in figure A.1).
Figures 6.12 and 6.13 compare the influence of momentum ratio and jet equivalence ratio on the penetration depth of the velocity trajectory showing profiles of the axial velocity u at x/D=1.5. Figure 6.12 reveals the influence of the momentum ratio J. Similar as in the test without reaction, the maximum of the velocity u is shifted to higher z/D coordinates with increasing momentum ratio. As expected, the magnitude of the maximum velocity is also increasing from momentum ratio 4 to 10.
Figure 6.13 compares the influence of different jet equivalence ratios in the range of $0.33 \leq \phi_J \leq 0.66$ for J=10. The equivalence ratio has only little influence on the magnitude of the maximum u-velocity ($u \approx 20$ m/s). The z/D position of the maximum is slightly lower for the ϕ_J=0.33 jet.
In figures 6.12 and 6.13 the near wall region (z/D<0.5) is characterized by a positive u-velocity. A strong reverse flow is observed, see e.g. between z/D=1 and z/D=2.2 for the J=10 jet in figure 6.13. The position of the center of the recirculating flow depends on momentum ratio and equivalence ratio. The momentum at the jet outlet where the flame is stabilized must be high enough, i.e. the pressure must be low enough, to force the flow to recirculate. Unfortunately, the flow patterns near the wall could not be detected by the PIV data appropriately. However, the streamlines must originate from other planes and enter the center plane from the side.

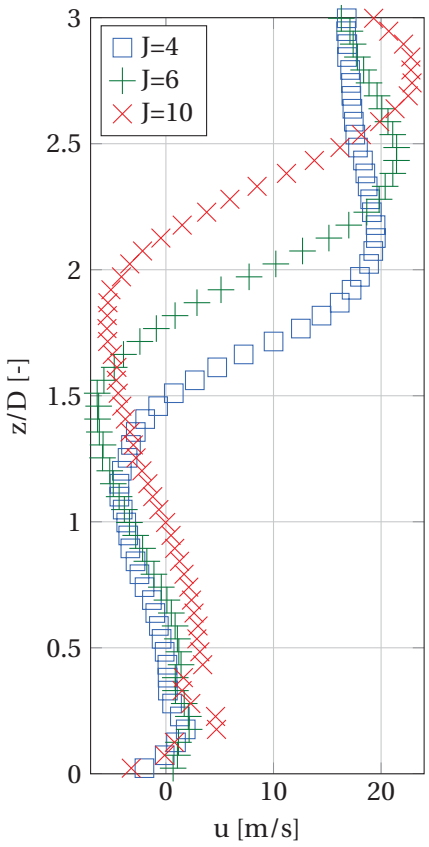

Figure 6.12: Mean reacting profiles of the velocity component u at x/D=1.5 for momentum ratio J=4,6 and 10 at jet equivalence ratio ϕ_J=0.5.

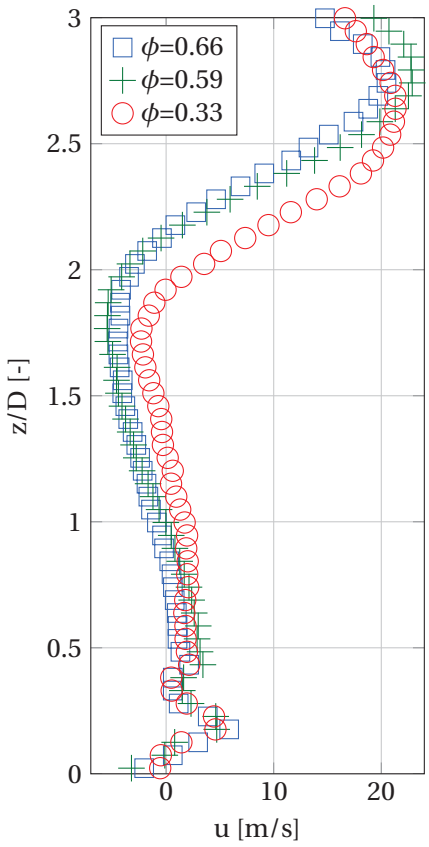

Figure 6.13: Mean reacting profiles of the velocity component u at x/D=1.5 for jet equivalence ratio $0.33 \leq \phi_J \leq 0.66$ at momentum ratio J=10.

A comparison between the non-reacting jet and the reacting jet at equivalence ratio ϕ_J=0.5 is given in figure 6.14. In general, the reacting jet exhibits a deeper penetration compared to the non-reacting jet of the same momentum ratio. The additional momentum due to reaction can be taken into account using equation 2.7 (see section 2.1.2 for the reacting momentum ratio definition). The momentum ratio of the reacting jet is calculated with the burnt jet products. By this equation, a non-reacting jet of momentum ratio J=15 is approximately similar in penetration depth to a reacting jet at J=6, see figure 6.14.
Figure 6.14 further illustrates the differences of the flow field. First, the core area of high velocity is thicker and longer in the reacting case. The ongoing reaction leads to higher temperature and lower density in the jet flow resulting in an additional momentum. In the jet area of high ve-

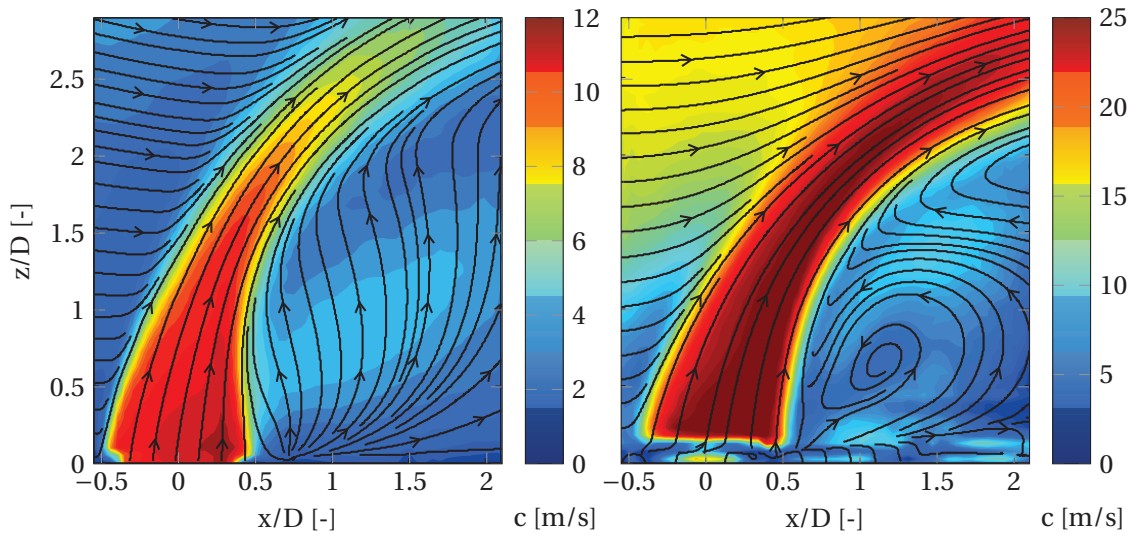

Figure 6.14: Velocity field comparison between the non-reacting jet at momentum ratio J=15 (left) and the reacting jet at J=6 and ϕ_J=0.5 (right).

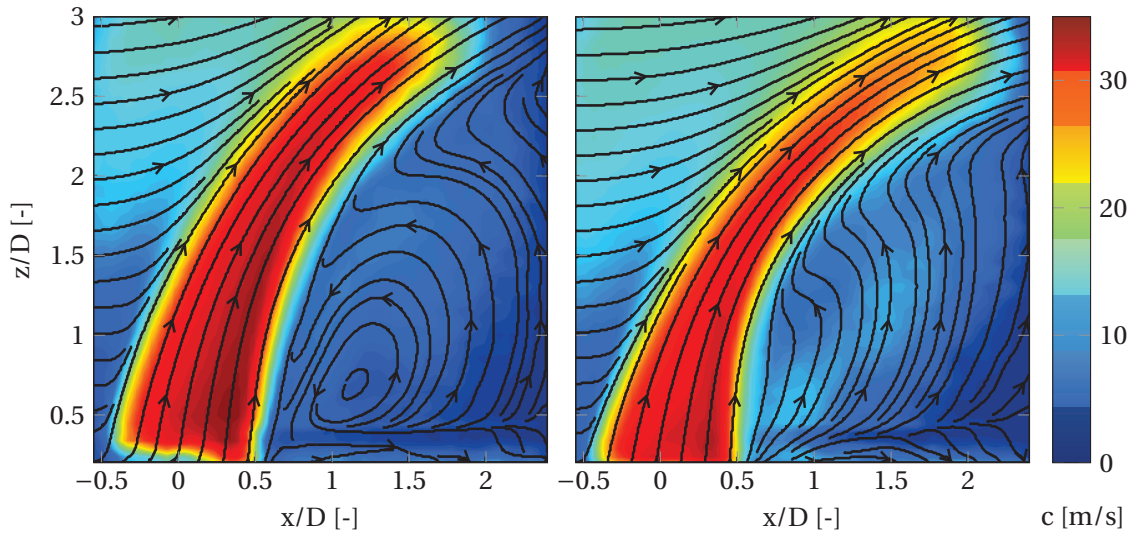

Figure 6.15: Velocity field comparison between the reacting jets of equivalence ratio ϕ_J=0.66 (left) and ϕ_J=0.33 (right) both at momentum ratio J=10.

locity the pressure is lower compared to the pressure in the wake region. The suction effect of the jet forces the flow in the wake behind the jet to recirculate counter-clockwise. In contrast to the reacting test case, the jet flow without reaction has a shorter core region since the velocity is reduced by turbulent diffusion processes and no additional momentum is present. The suction effect of the non-reacting jet is weaker resulting

in a different flow field in the wake region with upward streamlines as expected from literature.
Figure 6.15 reveals the differences of the reacting flow at high and low equivalence ratio of the jet. With lower heat release in the jet the core area of high velocity becomes shorter and the suction effect of the jet is reduced. The reacting jet at high momentum ratio (J=10) and equivalence ratio ϕ_J=0.33 (see right side of figure 6.15) depicts the flow pattern of upward streamlines in the wake similar to the non-reacting case. Reacting jets of an equivalence ratio $\phi_J \geq 0.5$ depict the counter-clockwise recirculating flow pattern in the wake.

6.1.2 Interaction Between Mixture and NO_x-Formation

In this section, the mean and instantaneous mixture field and its effect on NO_x-formation is studied in detail. As measurements and subsequent analysis turned out to be time-consuming, the following analysis is restricted to momentum ratio of J=6. The influence of jet equivalence ratio on the mixture and NO_x-field is taken into account by studying two different operating points at ϕ_J=0.66 and ϕ_J=0.77.

6.1.2.1 Exhaust Gas Measurements

Of main interest for the following analysis is the distribution of mixture fraction and NO_x-concentrations. As NO_x-levels are high in the anchored flame, the absolute NO_x-value is not of direct technical interest. However, the high spatial resolution due to the large diameter of the jet facilitates a detailed study of the interaction between mixing and NO_x-formation. Point-wise exhaust gas measurements in the y-z plane are taken four jet diameters downstream of the jet injection. In this plane combustion is complete for all presented operating points. The measurements conducted with a suction probe are analyzed in terms of the mean mixture fraction (calculated from O_2-concentration following equation 4.2) and mean NO_x-concentrations normalized to 15% O_2 at every measurement point.
Figure 6.16 shows the mean mixture fraction f derived from exhaust gas measurements for the two studied jet equivalence ratios of ϕ_J=0.66 and ϕ_J=0.77. The crosses mark the measurement points. The field is inter-

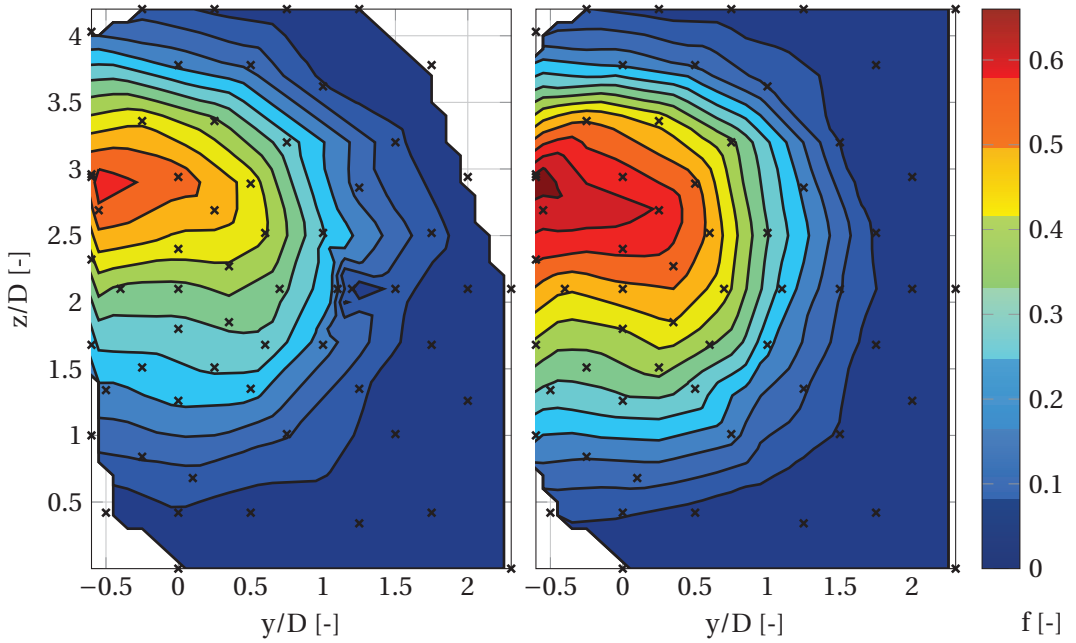

Figure 6.16: Mixture fraction f for jet equivalence ratios of ϕ_J=0.66 (left) and ϕ_J=0.77 (right) at x/D=4.

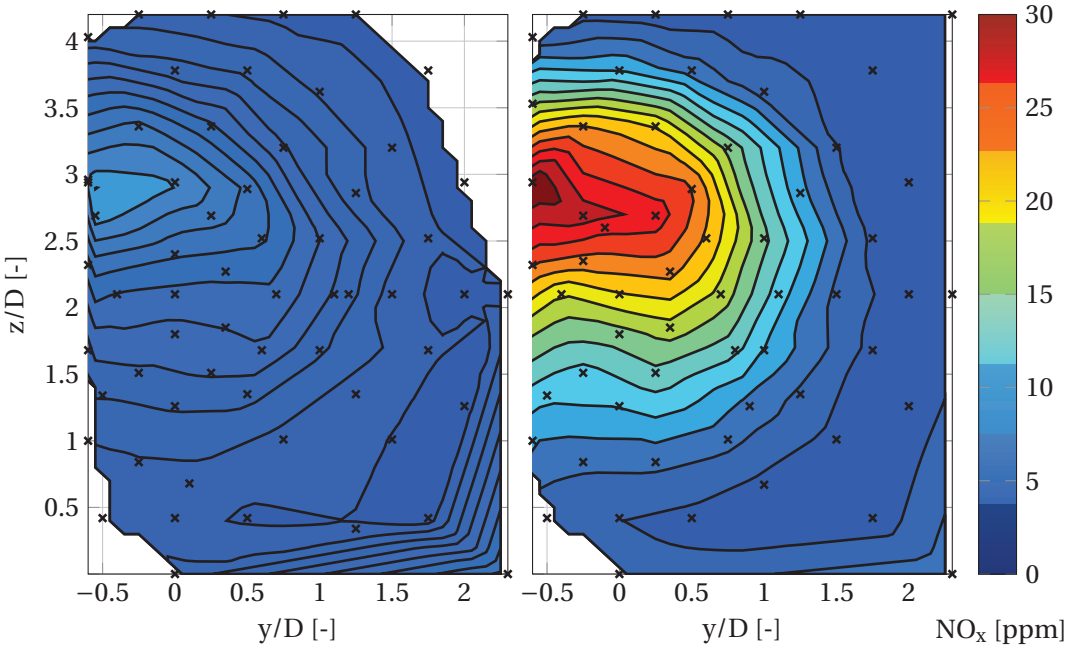

Figure 6.17: Normalized NO_x-concentrations for jet equivalence ratios of ϕ_J=0.66 (left) and ϕ_J=0.77 (right) at x/D=4.

polated in between these points. The results show that for the higher equivalence ratio, the mixing in the core of the jet is poorer for ϕ_J=0.77 (f approx. 0.6) than in the case of ϕ_J=0.66 (f around 0.5). The jet penetra-

tion depth, i.e. the position of the highest mixture fraction on the axis of symmetry at y=0, is approximately three diameters from the lower wall for both jets in this measurement plane. The distribution of the iso-contours of mixture fraction shows the characteristic kidney shape also observed in non-reacting jets in cross flow. A particularly interesting point is that the mixture gradient in the shear layer at the top of the jet is much steeper than at the bottom and towards the side walls. The two shear layers differ in the characteristics of the vortices: The vortices in the windward side show the typical ring-like form, whereas the shear layer vortices on the lee side are disturbed by the cross flow, as discussed in section 2.1.3 (see figure 2.3). As a result, the jet entrains pure cross flow in the upper shear layer, whereas a mixture of jet and cross flow is formed in the wake behind the jet.
NO_x-measurements for the two operating points are given in figure 6.17. High NO_x-concentrations in the area of high jet concentration are measured for the ϕ_J=0.77 jet. For the lower equivalence ratio jet of ϕ_J=0.66, normalized NO_x-concentrations of up to approximately 7.5ppm are measured. This behavior indicates a strong dependence of NO_x-formation on jet equivalence ratio according to the non-linear temperature dependency of the NO_x-kinetics.

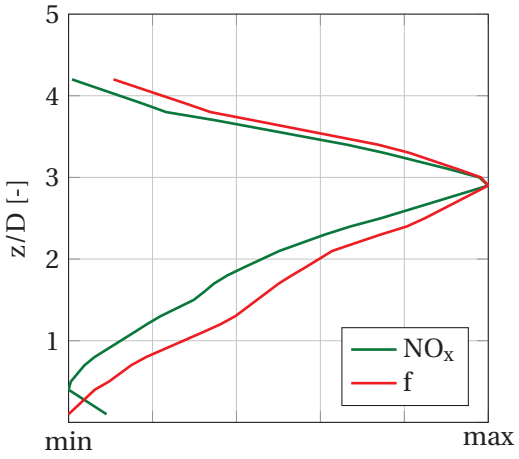

Figure 6.18: Comparison of normalized profiles of mixture fraction f and NO_x for jet equivalence ratio ϕ_J = 0.66 at x/D=4 and y/D=0.

The absolute NO_x-level of the atmospheric anchored flame is of minor interest for the technical application to gas turbine combustion. However, the distribution of the NO_x-values and the similarity to the distri-

bution of the mixture fraction gives a general indication of where and how NO_x is formed. Figure 6.16 shows that the jet core consists of approx. 50% jet material. In that zone, the jet NO_x-concentration is highest, see figure 6.17. The fields of NO_x-concentration and mixture fraction exhibit a large degree of similarity. In figure 6.18, the profiles along the z-axis, i.e. the height of the channel, at x/D=4 and y/D=0 are shown for a jet equivalence ratio of ϕ_J=0.66. The mixture fraction f and NO_x-concentrations are normalized by the difference between the maximum and minimum value. The two lines are in good agreement in the upper shear layer. However, in the lower part, the NO_x profile declines a little bit faster than the mixture fraction. In general, the gradients are steeper in the shear layer at the top than towards the bottom wall. This effect is also visible for the ϕ_J=0.77 configuration not shown here. Figure 6.18 shows that a simple correlation between the mean mixture fraction and the resulting NO_x-concentrations does not exist, although temperature reduction by entraining cross flow material is the main driver to reduce NO_x-formation. To further reveal differences between the distribution of NO_x-formation and mixture fraction, the x-z center plane perpendicular to the exhaust gas measurement profiles is studied.

6.1.2.2 Center Plane Mixture Analysis of the Mean and Time-Dependent Field

In order to further analyze the mixture field upstream of the x/D=4 measurement plane the Mie scattering method (MixPIV, see details on the method in chapter 4) was applied to the x-z plane at y=0, which cuts through the middle of the jet in longitudinal direction. Unfortunately, this measurement technique was only applicable for the ϕ_J=0.66 jet, since with higher equivalence ratio the flame luminescence increasingly interferes with the scattering of the seeding particles and deteriorates the data quality. Although not all disturbances due to background and laser sheet inhomogeneities could be perfectly eliminated, the mixture field data allows quantitative evaluations and it can be used for statistical analysis, which delivers RMS values and PDFs of the mixture fraction (see section 2.3.4). The temporal mean mixture field is shown on the left of figure 6.19, and the temporal RMS_T-values of the mixture on the right. The black dashed line denotes the mixture trajectory consisting of the points with highest value of the mixture fraction, see section 2.1.2.

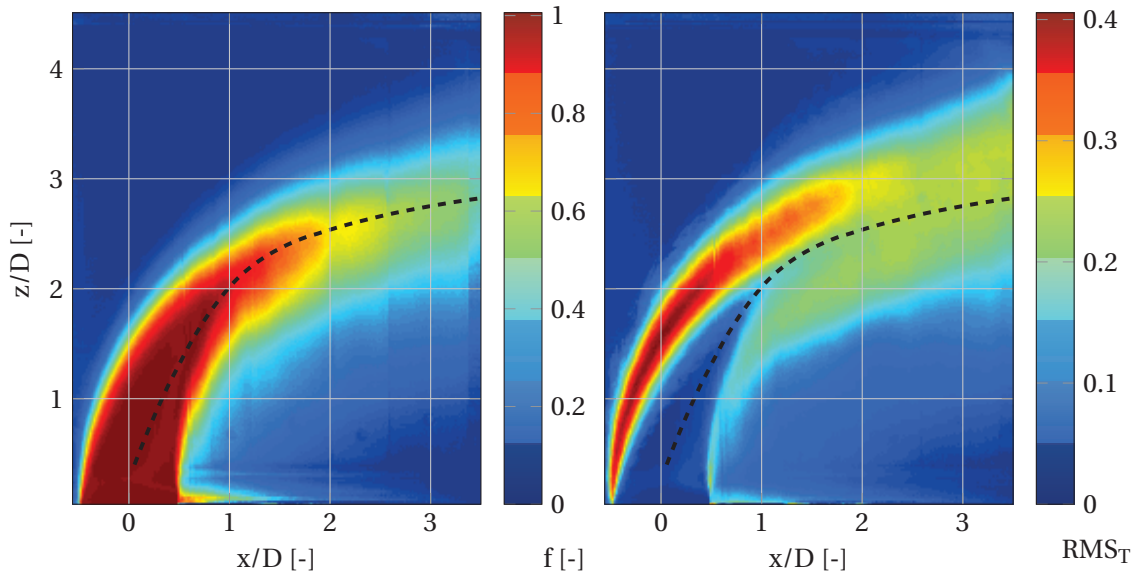

Figure 6.19: Mean mixture field and RMS_T in the x-z center plane for jet equivalence ratio of ϕ_J=0.66. The dashed line denotes the jet mixture trajectory.

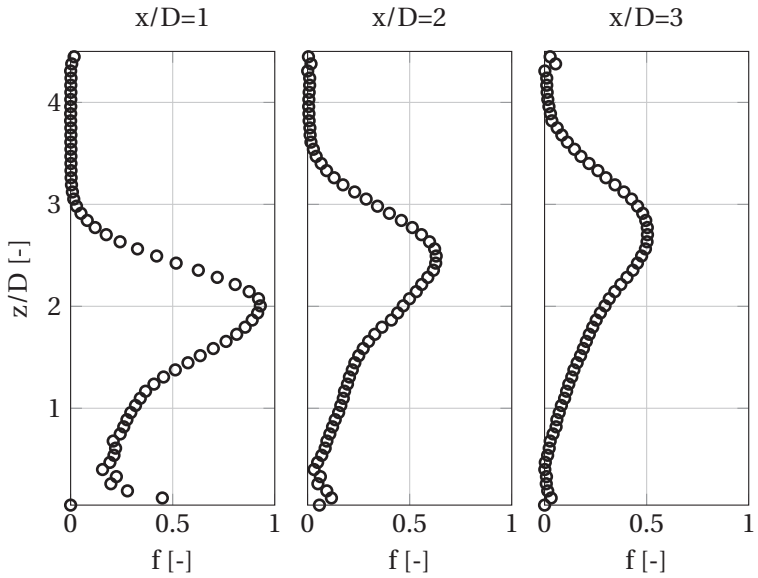

Figure 6.20: Mixture profiles in the x-z center plane at x/D=1,2,3 for jet equivalence ratio of ϕ_J=0.66.

The mixture profiles over the height of the channel can be used to compare against the distribution of mixture fraction in the line of symmetry of the exhaust gas measurements perpendicular to the center plane given in figure 6.16. Therefore, profiles of the mean mixture fraction in y-direction one, two, and three diameters downstream of the location of

the jet injection are plotted in figure 6.20. Some disturbances due to reflections are visible near the bottom wall, but above y/D≈0.3 the data is free of such errors. For cross checking, the profile of the mean field at x/D=3, see figure 6.20, can be compared against the distribution of the mixture fraction f in figure 6.16 at x/D=4. The maximum mixture fraction f is approx. 0.5. However, data of the mixture fraction (with MixPIV) in the center plane is not available at the x/D=4 position and − assuming a progressing decay − would lie slightly below the maximum mixture fraction in figure 6.16. The profiles in figure 6.20 confirm that the gradient in the shear layer at the top is much steeper than the gradient in the shear layer below the jet, see figure 6.16 and 6.17 for comparison. Also the measured width of the jet in z-direction matches this data, ranging from approx. 0.5D to 4D in figure 6.20 at x/D=3 (compare to figure 6.16). Following the trajectory of worst mixture, shown in figure 6.19, a distance of approx. three diameters from the bottom wall is reached at x/D=3. These results again are in good agreement with the data shown in figure 6.16.

In addition to the time mean temperature, temperature fluctuations play an important role in NO_x-formation and are caused by temporal mixing fluctuations. An indication of the temporal mixture quality in the experiment is given by the RMS_T-values of the mixture fraction f. The data of the MixPIV analysis in the x-z center plane of the ϕ_J=0.66 jet is shown in figure 6.19. The field of the RMS_T-values on the right side of figure 6.19 reveals two zones with high temporal fluctuations, which represent the shear layers between the jet and the cross flow. In the windward shear layer RMS_T-values up to 0.4 are reached. In this upper shear layer, jet material mixes with pure cross flow. The high RMS_T-values indicate a high level of temporal unmixedness in that zone. Interestingly, the RMS_T-values in the shear layer on the lee side of the jet are much smaller and do not exceed 0.2. In the region in the wake behind the jet, turbulent mixing between the jet flow and the cross flow is stronger. As a result of the vortex system, see figures 2.2 and 2.3, the gradient in the region below the jet trajectory is lower and also the temporal fluctuations of the mixture fraction RMS_T are smaller, compare to figure 6.18. These results indicate that the mixing progress on the lee side is more developed than in the windward shear layer. It was shown for reacting jets that, due to the recirculation zone in the wake behind the jet, veloc-

ity fluctuations are higher compared to the windward shear layer (see figures 6.11 and A.1). The regions of high velocity fluctuations and high temporal fluctuations of mixture fraction are distributed differently. The higher and steeper gradient of the windward shear layer leads to higher fluctuations of mixture fraction in this region.

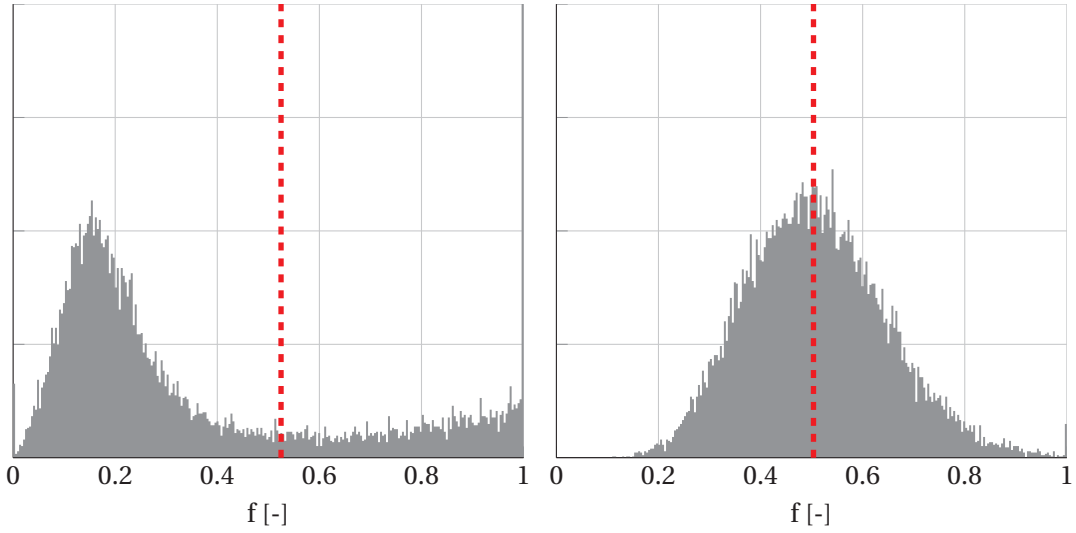

Figure 6.21: Characteristic PDFs in the windward (left) and lee (right) shear layer for ϕ_J=0.66, mean mixture fraction indicated by red line.

The differences of mixing in the two shear layers can be further characterized by the PDFs shown in figure 6.21. Two characteristic PDFs are chosen as examples of the temporal mixture distribution in the windward and lee side shear layer. The PDFs in figure 6.21 illustrate the different degree of mixing in the two shear layers. At the two selected positions in both shear layers the mean mixture fraction represented by the vertical red dotted line is almost identical (f ≈0.5). The PDF representing the windward side indicates a high level of local unmixedness: Although the mean mixture is approx. 0.5 (f=0.525), this mixture is hardly ever appearing. The highest peak is at the mixture fraction of one, consisting of pure jet material. The second peak is at f≈0.15, near the overall ideal mixture. The shape of the PDF indicates that the local mixing state is in between the temporarily unmixed case with bimodal PDF, and the case with a certain degree of mixing represented by a Gaussian shape of the PDF. The PDF on the lee side indicates higher mixing progress, although the variance is large. The observed differences regarding the mixing state

in the two shear layers lead to the conclusion that NO_x-formation is significantly different.

6.1.2.3 Influence of Mean Mixture Field and Temporal Fluctuations on NO_x-Formation

It is shown in figure 6.19 that the mixing on the windward and the lee side shear layer is different. While the upper shear layer entrains (colder) pure cross flow material, the wake region consists of a (hotter) mixture of cross flow and jet products. This effect leads to the steeper decline of the upper gradient in the distribution of the mean mixture fraction and of the NO_x, see figures 6.18 and 6.20. Temporal fluctuations of the mixture fraction have an important influence on NO_x-formation, see section 2.3.4. Due to the high thermal sensitivity of post-flame NO_x-formation, temperature peaks connected to temporal fluctuations of the mixture fraction lead to higher NO_x. In terms of NO_x-formation, the windward shear layer has the disadvantage of a higher temporal unmixedness exemplified by the higher RMS_T-values and the bimodal PDF shape. Compared to the more advanced mixture distribution in the lee side shear layer with the Gaussian shaped PDF, the same mean mixture fraction would result in lower NO_x in the lee side shear layer, see lower part of figure 6.18.

6.2 Lifted Flames

In section 3.2, a second scaling principle following similarity in Karlovitz number of the jet flame was introduced. It was assumed that this scaling leads to similar lift-off heights and flame positions compared to gas turbine application. The results of the experiments with the smaller diameter of D=15mm will be presented in the following. In contrast to the results of the large-scale experiments with the 100mm diameter jet, the experiments with a smaller diameter at a higher momentum ratio are not suitable for studying the reacting flow-field in detail, since the mixture fraction analysis is not applicable to the lifted jet flames, see section 4.4. The lifted flame is analyzed to collect the data needed for the chemical network modeling of the following chapter 7 and the transfer to high pressure conditions. The parameters of interest are state of mixture at ig-

nition f_{pf} and the mixture fraction at measurement point f_{MP}, as well as the post-flame residence time τ_{post}, i.e. the time of flight a particle moving along the trajectory from the end of the flame until the measurement point.
In the following, the lifted flame scaled by Karlovitz number at equivalence ratio ϕ_J=0.66 is studied in detail. The operating conditions are given in table 3.1, see section 3.3.

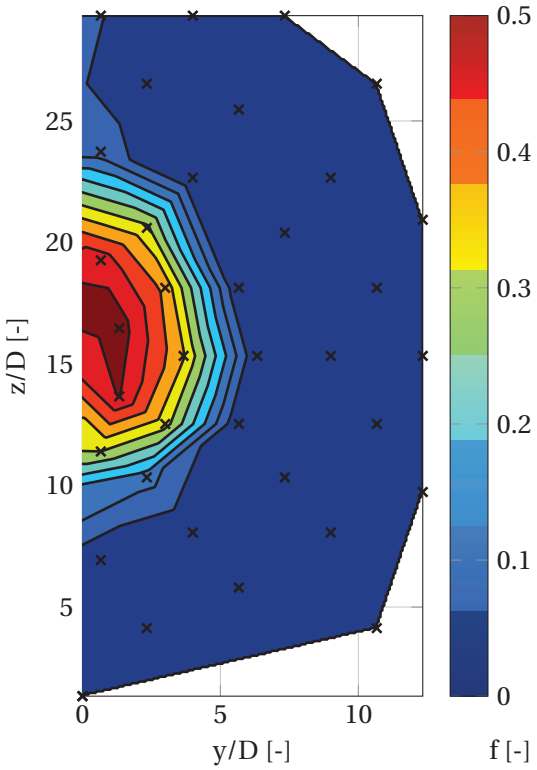

Figure 6.22: Mixture fractions of the lifted flame scaled by Karlovitz number at equivalence ratio ϕ_J=0.66 in the y-z plane 7.7 jet diameters downstream of the jet injection, the measured points are marked with crosses.

6.2.1 NO_x-Concentrations and Mixture Fields

Also for the lifted flame scaled by Karlovitz number exhaust gas measurements are performed with the traversable water-cooled suction probe, see section 4.2. The results of the mixture fraction f and the normalized NO_x-measurements at x/D=7.7 are shown in figures 6.22 and 6.23, respectively. The mixture fraction is calculated following equation 4.2, and the NO_x-data are normalized to 15% O_2 using the measured lo-

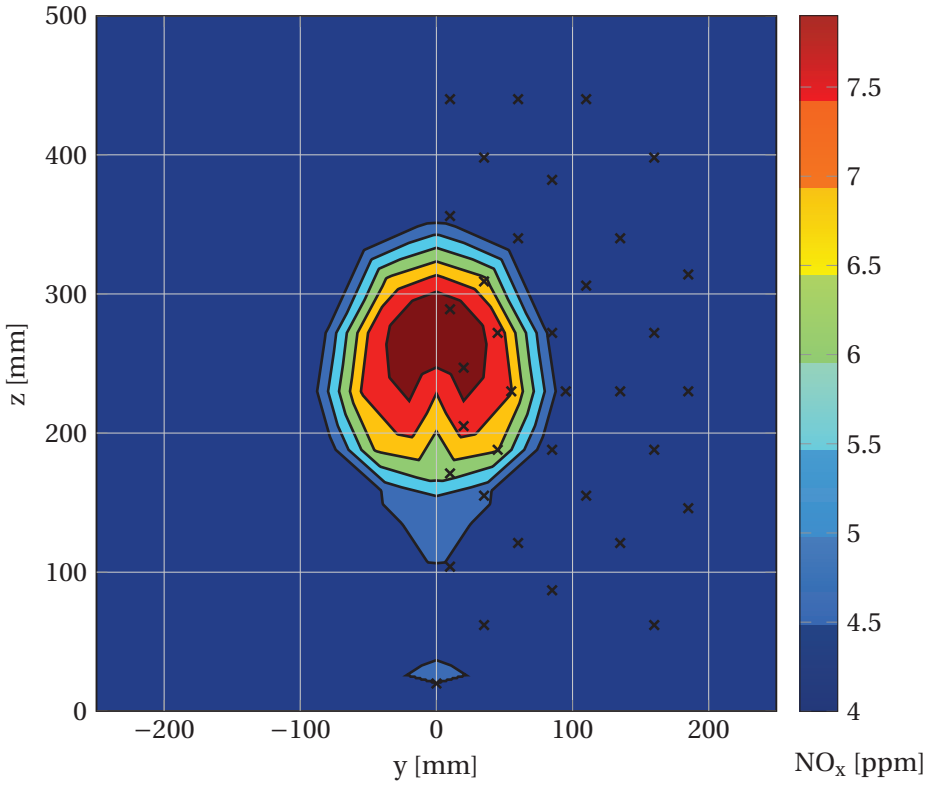

Figure 6.23: Normalized NO_x of the lifted flame scaled by Karlovitz number at equivalence ratio ϕ_J=0.66 in the y-z plane 7.7 jet diameters downstream of the jet injection, the measured points are marked with crosses.

cal O_2-concentrations. At the measurement position the jet flame is fully burnt and CO is in thermal equilibrium. For extracting the global mean NO_x-value, the NO_x-field of the whole channel (500x500mm) is needed, see figure 6.23. In figure 6.23, the NO_x-value of the cross flow is mapped on areas outside the jet region, where no measurement data are available. The NO_x-concentration of the cross flow without secondary injection is measured separately and compared to the NO_x-result of free flame simulation. A consistent value of approx. 4ppm is obtained by both the measurements and the simulation. Figure 6.23 shows the NO_x-distribution over the entire channel (values are mirrored at the center line) for the lifted flame scaled by Karlovitz number at equivalence ratio ϕ_J=0.66 in the y-z-measurement plane 7.7 jet diameters downstream of the jet injection.

In contrast to the results obtained from the anchored flame with significantly lower momentum ratio (figure 6.18) the fields of the mixture fraction and the NO_x-concentration are similar to a large degree. This effect

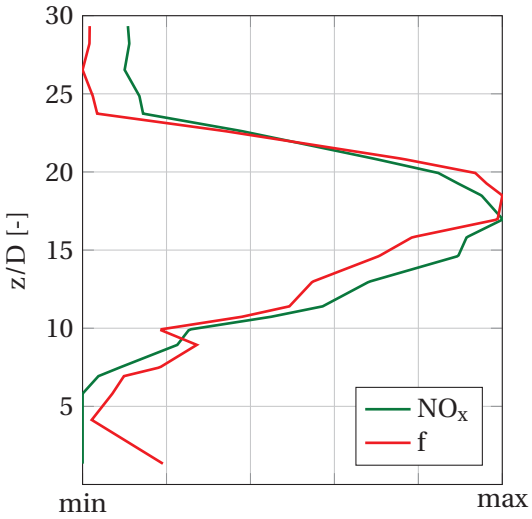

Figure 6.24: Comparison of mixture fraction and NO_x profiles over the channel height at y/D=0 of the lifted flame scaled by Karlovitz number at equivalence ratio ϕ_J=0.66.

is shown more precisely in figure 6.24 at y/D=0. Both profiles of NO_x and mixture fraction are normalized with the difference of their maximum and minimum values. The influence of the different mixture histories in the lower and upper shear layer are negligible for this high momentum ratio jet, as the influence of the lower wall is reduced. Due to the high momentum of the jet, the velocity and mixture field becomes similar to the one of a free jet, see section 2.1.3. The similarity between the mixture fraction and the NO_x-concentration, see figure 6.24, is later used in the framework of chemical reactor modeling. In that context, the mixture fractions and NO_x-concentrations in the measurement plane following the jet trajectory is needed. The comparison of figure 6.22 with figure 6.23 reveals that the mixture fraction on the jet trajectory of f_{MP}=0.5 corresponds to the maximum NO_x-concentration of 7.5ppm. These values will be used as anchor points for the model presented in chapter 7.

6.2.2 Flame Position and Post-Flame Residence Time

Beside the presented mixture fraction and NO_x-measurements in the y-z plane at x/D=7.7 downstream of the jet injection, a detailed analysis of the mixing field and the residence time in the x-z center plane would be helpful for the appropriate setup of the chemical network model. However, the quantitative analysis of the mixture field using Mie scattering

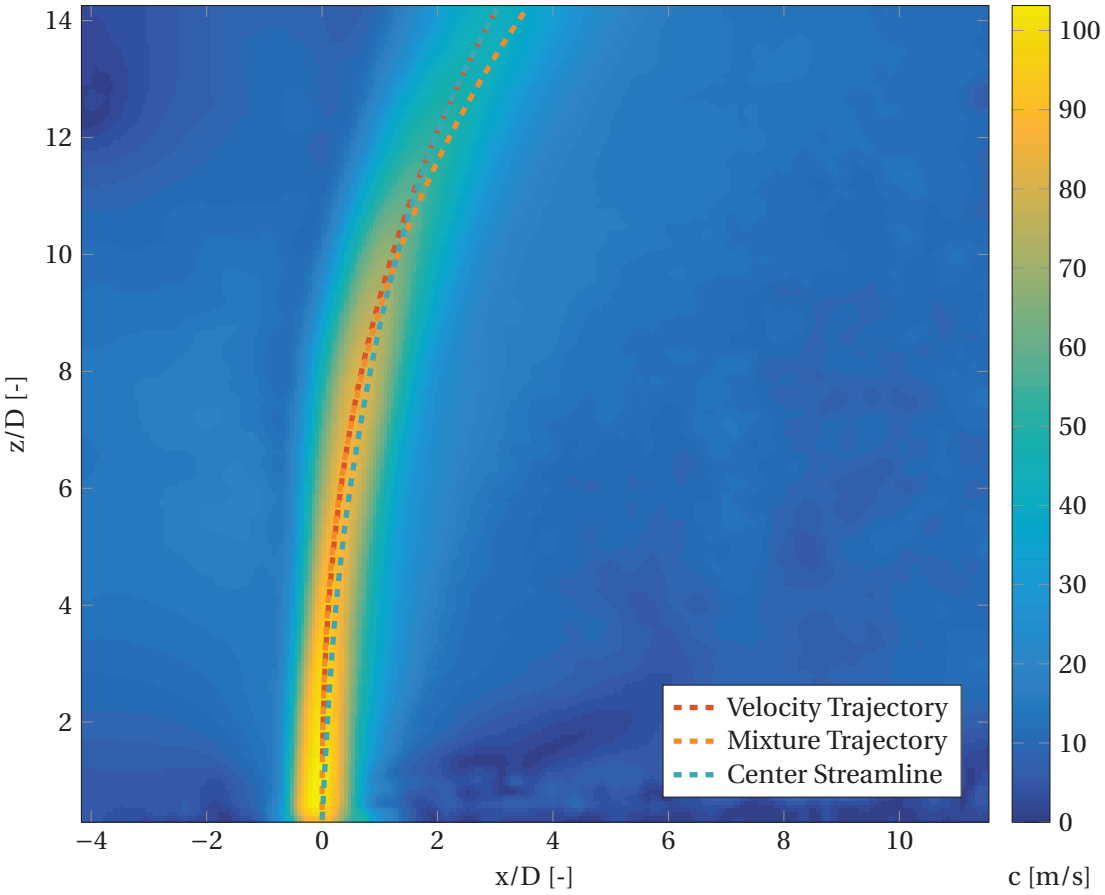

Figure 6.25: Comparison of extracted jet trajectories and velocity field in the x-z center plane of the lifted flame scaled by Karlovitz number at equivalence ratio ϕ_J=0.66.

imaging (MixPIV) is not applicable to the lifted flames, as the flame front cannot be detected in the data. Thus, it is not possible to determine the state of mixture at ignition (pre-flame mixture f_{pf}) from the experimental data. This fact limits the merit of Mie scattering imaging for the analysis of the lifted flame. However the jet trajectory can be clearly identified with this method.

The trajectories from PIV and Mie scattering imaging are shown in figure 6.25, together with the measured velocity field. As only the velocity in the jet is of interest, the cross flow is left unseeded for practical reasons. The velocity field outside the jet region is not analyzed and the velocity c is zero in figure 6.25. Velocity and mixture trajectory as well as the center streamline are compared with each other in figure 6.25. For the high momentum ratio of the lifted flame, all three evaluation methods for the jet trajectory deliver almost identical results as expected in the near field.

As the measurement section in figure 6.25 does not fully cover the jet trajectory downstream to x/D=7.7, where data in the y-z plane is available, an extrapolation is required for z/D>14. For this purpose, the trajectories shown in figure 6.25 are fitted following equation 2.3. The results obtained for the velocity trajectory (equation 6.1) and for the mixture trajectory (equation 6.2) are plotted in figure 6.26.

$$\frac{z_v}{D} = 9.2621 \left(\frac{x}{D}\right)^{0.3860} \tag{6.1}$$

$$\frac{z_f}{D} = 9.096 \left(\frac{x}{D}\right)^{0.3545} \tag{6.2}$$

The comparison of the factors A and B in equations 6.1 and 6.2 to literature data following equation 2.3 [51, 94] shows good agreement. Factor B (B=0.386) is near the upper limit of the reported values (0.28<B<0.34). Factor A depends on how the momentum ratio is calculated. The momentum ratio based on the density of the reactants is J=150. However, chemical reaction has an effect on the trajectory, because the expansion due to heat release increases the effective jet momentum. Following equation 2.7 in section 2.1.2, a reacting momentum ratio of J_{reac}=375 is obtained. The value of factor A for this higher momentum ratio is approximately A=1.5. These values are again in good agreement with literature (1.2<A<2.6).
In figure 6.26 the available data from the x-z center plane (at y=0) are combined with mixture fraction data from figure 6.22 at y=0. The three trajectories are similar to each other in the near field and start to differ at the beginning of the far field region. According to literature, e.g. [51, 63], the mixture trajectory lies slightly below the velocity trajectory. This trend is also observed in figure 6.26. The penetration depth of the fitted mixture trajectory at x/D=7.7 is compared with the position of the worst mixture of the exhaust gas measurements, see figure 6.22 for comparison. Both methods consistently deliver z/D≈18 at x/D=7.7 for the location of the mixture trajectory. These results indicate that the trajectory of the jet can be described with data from the x-z center plane (at y=0) and from the y-z plane at x/D=7.7 consistently.

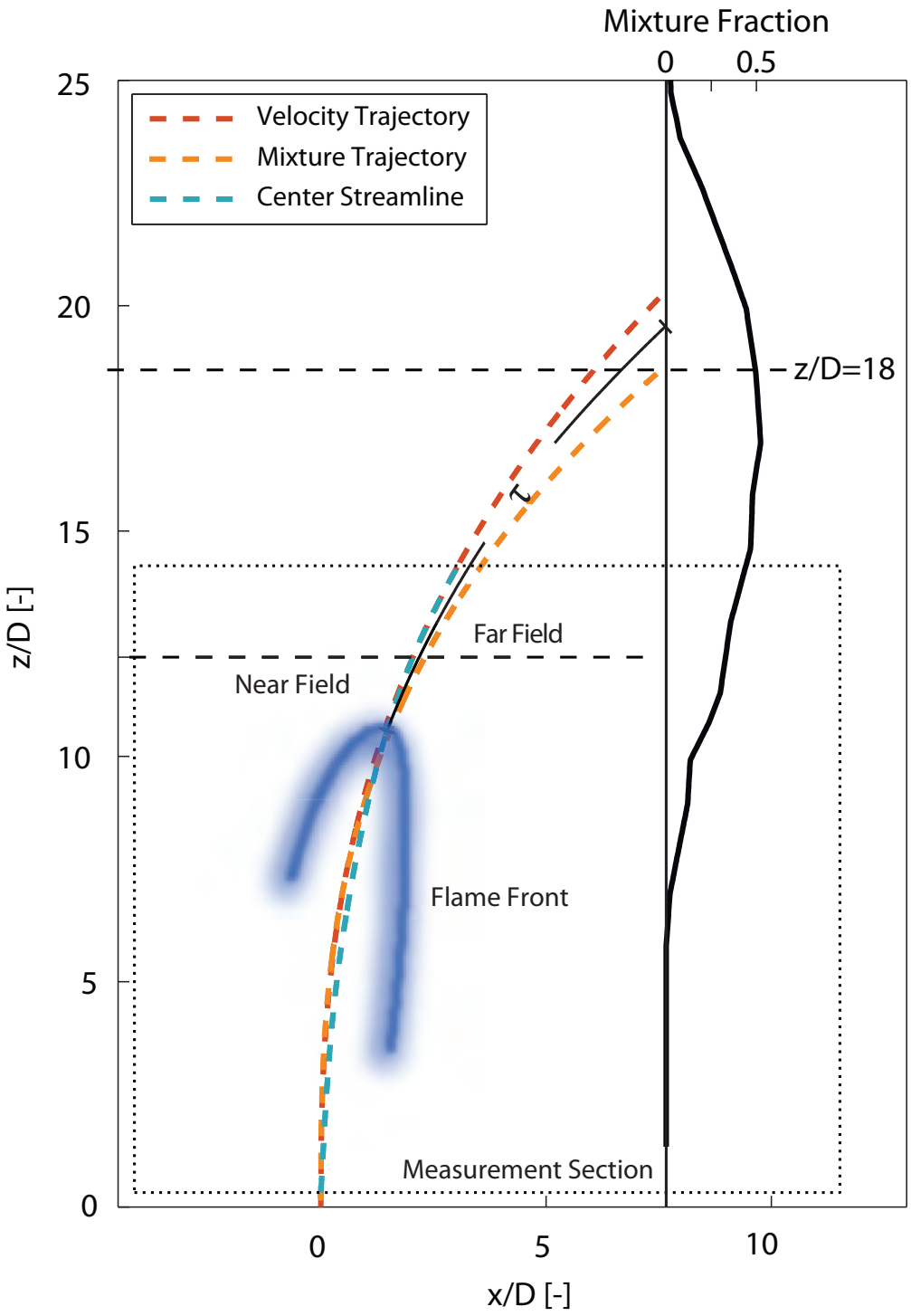

Figure 6.26: Comparison of extracted jet trajectories and position of the flame in the x-z center plane with the mixture fraction at x/D=7.7 of the lifted flame scaled by Karlovitz number at equivalence ratio ϕ_J=0.66.

For the validation of the reactor model, the information on the flame position and shape are needed. In the current study, the position of the flame tip is estimated from OH* images, which provide line of sight integrated data in y-direction. The flame position is shown as the blue zone in figure 6.26 illustrating the derived flame position in the center plane at y=0.
Finally, putting all information together, an estimate of the "time of flight" of the jet material along the jet mixing trajectory after the flame is extracted. This quantity is essential to receive good results from the chemical network model, as NO_x-formation is sensitive to the residence time in the hot environment. In the following, the residence time is calculated by integrating the velocity along the jet trajectory in time starting from the flame tip. The velocity data are extracted from the available PIV velocity field and the fitted trajectory allowing extrapolation to x/D=7.7 (figure 6.26). The decay of the velocity along the trajectory outside the visible region is estimated using the power law $(z/D)^{-2/3}$ proposed in [52]. This law is applied to the velocities u and w in x- and z-direction, respectively, following [51]. For the w-component of the velocity, the jet outlet velocity U_J is taken as initial value, see equation 6.3. For the u-velocity component, the cross flow velocity U_X is taken as the asymptotic maximum value in equation 6.4.

$$w \propto \left(\frac{z}{D}\right)^{-2/3} U_J \tag{6.3}$$

$$U_X - u \propto \left(\frac{z}{D}\right)^{-2/3} U_X \tag{6.4}$$

From both components, the absolute velocity $c=\sqrt{u^2+w^2}$ along the jet trajectory is calculated. Finally, the residence time from the flame tip to the measurement plane at x/D=7.7 is estimated by integration of the absolute velocity c along the trajectory coordinate ξ. This method delivers a post-flame residence time of approximately τ_{post}=5ms, which is applied to the chemical network model presented in the following section.

7 Chemical Network Model for Data Transfer to Gas Turbine Conditions

Chemical reactor network models are widely used as they have the ability to transfer atmospheric data to higher pressure conditions, see e.g. [10, 22, 49]. However, the network model must be adapted to the individual problem considered to capture the prevailing effects from three-dimensional reacting flow field on chemistry.
In the following, a combination of experimental data and chemical modeling is used to study NO_x-formation in lifted flames. First, the experimental results are used to validate the network model. Second, a sensitivity study investigates differences in pre- and post-flame mixing under atmospheric and 20bar combustion in detail. Finally, the experimentally validated model is run at 20bar. The results of the simulation will lead to an evaluation of the benefit of axial staging concerning NO_x-emissions under engine conditions. Moreover, also the realistic case of higher NO_x-levels due to unmixedness and air addition along the combustor liner are investigated.

7.1 Similarity Considerations for a Transfer to 20bar

The operating point of the lifted flame with the smaller diameter of 15mm is characterized in section 3.2 and is chosen due to a similarity in Karlovitz number. It is assumed that this operating point shows similarity in lift-off height to a flame under typical conditions in a gas turbine combustor. In the experimental analysis of section 6.2 it was shown that the fields of mixture fraction and NO_x-concentration exhibit a high degree of similarity in the atmospheric case. For scaling of atmospheric data to engine conditions, we assume that the flow and mixture fields are independent of pressure. With this assumption, experimental data in the y-z plane are scaled to high pressure conditions according to equation 7.1 and 7.2 respectively.

$$\left.\frac{f(y,z)-\min\left(f(y,z)\right)}{\max\left(f(y,z)\right)-\min\left(f(y,z)\right)}\right|_{1bar} = \left.\frac{f(y,z)-\min\left(f(y,z)\right)}{\max\left(f(y,z)\right)-\min\left(f(y,z)\right)}\right|_{20bar} \tag{7.1}$$

$$\left.\frac{NO_x(y,z)-\min\left(NO_x(y,z)\right)}{\max\left(NO_x(y,z)\right)-\min\left(NO_x(y,z)\right)}\right|_{1bar} = \left.\frac{NO_x(y,z)-\min\left(NO_x(y,z)\right)}{\max\left(NO_x(y,z)\right)-\min\left(NO_x(y,z)\right)}\right|_{20bar} \tag{7.2}$$

Due to the similarity between the mixture fraction and NO_x-concentration fields, only the minimum and maximum NO_x-value is needed to be modeled. With the similarity rule according to equation 7.2 and the atmospheric NO_x-field data (see figure 6.23), the two-dimensional distribution in the y-z plane can be reconstructed for engine conditions. This data can then be used to calculate the mean NO_x-concentration, that is required to evaluate the potential benefit of the jet in cross flow configuration compared to single stage combustion.
For the lifted flame at the equivalence ratio of ϕ_J=0.66, minimum and maximum values are available from experiments and will be used for the validation of the reactor network model, which is introduced in the next section.

7.2 Reactor Network Model Structure

The structure of the employed reactor network model is shown in figure 7.1. It consists of a freely propagating flame (1DFF) burning a mixture of jet and cross flow material and a constant pressure reactor (CPR), which allows continuous admixing of cross flow material to the post-flame region.
For the calculation of the NO_x-concentration in the hot cross flow, a separate one-dimensional free flame model is employed [45], which is fed with the reactants of the first combustor stage. The burnt cross flow products are stored in a reservoir, which is used to provide the cross flow material for entrainment upstream of the freely propagating flame and along the post-flame reactor.

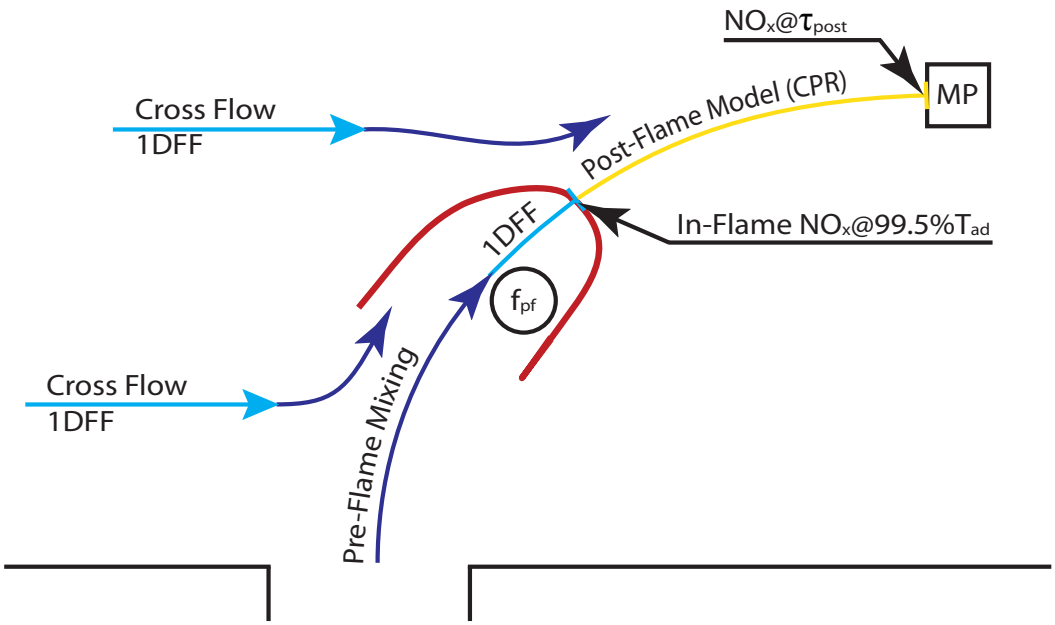

Figure 7.1: Scheme of the chemical network model.

The main purpose of the network model is the computation of the species concentrations due to chemical reactions along the jet trajectory under engine conditions. The NO_x-concentrations are evaluated at a predefined position corresponding to the combustor exit. In case of model validation, the data are evaluated at the position of the atmospheric test. The model consists of two consecutive parts, see figure 7.1: The first part consists of a free flame burning a pre-flame mixture, which is characterized by the mixture fraction f_{pf} at ignition, see section 2.3.2.1. The mixture fraction is calculated with equation 2.45. The NO_x formed until the end of the flame (at 99.5% T_{ad}) is allocated to in-flame NO_x.
The composition of the products at the end of the flame front is used as the initial condition for the second or post-flame part of the reactor model, which covers the post-flame region downstream of the heat release zone. It is modeled with a constant pressure reactor (CPR), see section 2.3.2.2. The state of the reactor is advanced in time until the post-flame residence time τ_{post} is reached. A constant entrainment of cross flow material into the CPR is specified to take jet mixing into account. All NO_x-concentrations in the following are normalized to 15% O_2, as described in section 4.2.2.

7.3 Model Validation with Experimental Data

In this section, the NO_x-formation along the jet trajectory is simulated with the network model for the lifted flame at equivalence ratio ϕ_J=0.66. The NO_x-concentration in the cross flow is used as input parameter. According to the measurements, 4ppm NO_x is generated in the first stage of the test rig (see figure 6.23). The NO_x-value on the jet mixture trajectory at x/D=7.7 is also known from experiments presented in the previous chapter, see section 6.2. Because the mixing with cross flow is worst along the jet mixture trajectory, the highest NO_x-concentrations are found in that region. At the reference measurement point (at x/D=7.7, see MP in figure 7.1), a value of NO_x=7.9ppm is measured for the lifted flame at the equivalence ratio of ϕ_J=0.66. Furthermore, it is known from the experiments that the mixture fraction on the jet trajectory at x/D=7.7 is f_{MP}=0.5, and that the post-flame residence time of the jet material flowing along the jet trajectory is approximately τ_{post}=5ms.
However, little is known about the degree of pre-flame mixing in terms of the mixture fraction f_{pf} at the onset of reaction. For this reason, a straightforward validation of the network model is not possible, but the network model can be used to identify, which pre-flame mixture fraction f_{pf} leads to the measured value of NO_x=7.9ppm at x/D=7.7. The network model predicts that a mixture fraction of f_{pf}=0.52 leads to this value (see figure 7.5, details are given in the following sensitivity study). NO_x-values as low as 7.9ppm can only be achieved if the mixture at the location of flame stabilization in the jet is already massively diluted by cross flow combustion products. This result is particularly interesting, because the mixture fraction at the measurement point (MP in th figure 7.1) is in the same range.

7.4 Sensitivity Study

In the following, the sensitivity of the model on the input parameters is investigated in order to assess its predictive capability regarding the NO_x-emissions of axially staged combustors operated at engine conditions. A sensitivity study is conducted, which covers the influence of pre-flame and post-flame mixing, post-flame residence time and temperature on NO_x-formation. Simulations are run at 1bar and 20bar in order

to investigate the pressure dependencies of the kinetics. In the following, the lifted flame at the equivalence ratio of ϕ_J=0.66 is selected with the equivalence ratio of ϕ_X=0.5 in the cross flow.

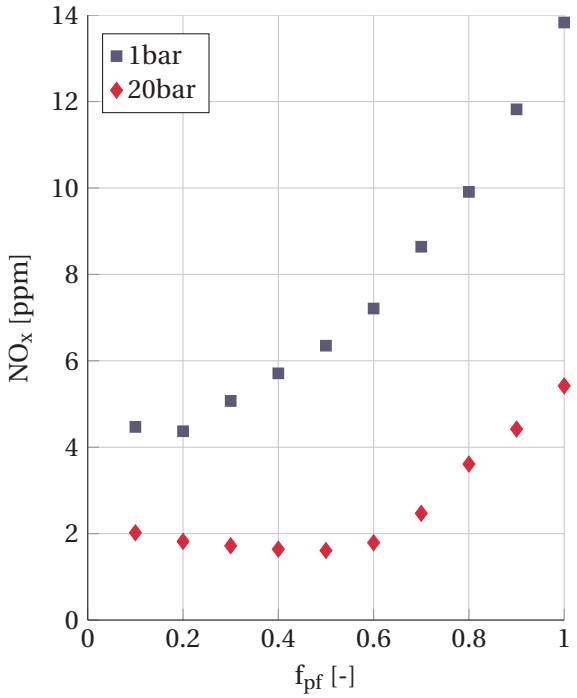

Figure 7.2: Influence of pre-flame mixing on in-flame NO_x-formation at 1bar and 20bar (lifted flame at equivalence ratio ϕ_J=0.66).

Figure 7.2 depicts the influence of pre-flame mixing on in-flame NO_x-formation. Apparently a higher degree of mixing before the onset of reaction in the freely propagating flame reduces in-flame NO_x-formation at 1bar and 20bar. However, at high pressure, at f_{pf}=0.6, minimum in-flame NO_x is reached and stronger pre-flame mixing does not further reduce in-flame NO_x-formation. This result differs from the 1bar case: The increase of pre-flame mixing leads to a drop of in-flame NO_x until f_{pf}=0.2 is reached. The general level of in-flame NO_x is significantly lower at 20bar, because the reaction time in the flame front drops with increasing pressure. These results indicate that mixing before the onset of reaction is beneficial only up to a certain level at 20bar.
In order to study the influence of post-flame mixing on NO_x-formation, the scenario shown in figure 7.3 is studied. In all calculations the mixture fraction at the end of the reactor (MP) is set to f_{MP}=0.5 and the post-

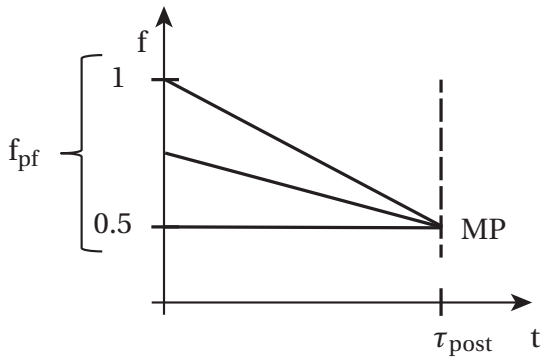

Figure 7.3: Scenario for investigating the influence of post-flame mixing on NO_x-formation.

flame residence time is kept constant at τ_{post}=5ms for the atmospheric and 20bar test case, because these values correspond to experimental results of the lifted flame. The pre-flame mixture is the first parameter of interest regarding post-flame NO_x-formation. It is varied in the reasonable range between $0.5 \leq f_{pf} \leq 1$. At f_{pf}=0.5, no further cross flow material is entrained downstream of the flame front, see the second part of the network model in figure 7.1. For higher f_{pf}, constant entrainment of cross flow material over time is assumed in the post-flame region. In any case, the level of entrainment is selected such that the measured mixture fraction of f_{MP}=0.5 is reached at the end of the reactor (MP). This means that a reduction of the level of pre-flame mixing automatically leads to stronger entrainment in the post-flame region. Independent of the choice of the pre-flame mixture f_{pf}, T_{MP}=1890K is finally reached at the end of the post-flame reactor for the jet equivalence ratio of ϕ_J=0.66. This temperature corresponds to the measured mixture fraction (at MP) f_{MP}=0.5.

Figure 7.4 schematically shows the typical concentration decay of jet material along the trajectory of a turbulent jet in cross flow (see details in [136]). The figure illustrates that assuming linear decay is reasonable. Figure 7.5 depicts the predicted NO_x-concentration for pre-flame mixtures between $0.5 \leq f_{pf} \leq 1$. For both investigated pressures, the NO_x-formation monotonically drops when pre-flame mixing is increased, although in-flame NO_x has a minimum for f_{pf}=0.5 at 20bar, see figure 7.2. In general, a higher degree of pre-flame mixing is favorable in terms of overall NO_x-reduction. The effect is stronger at 20bar than at 1bar. The

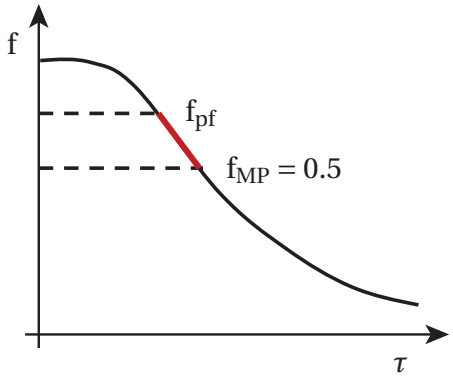

Figure 7.4: Sketch of the mixture fraction f along the trajectory of a jet in cross flow, adapted from [136].

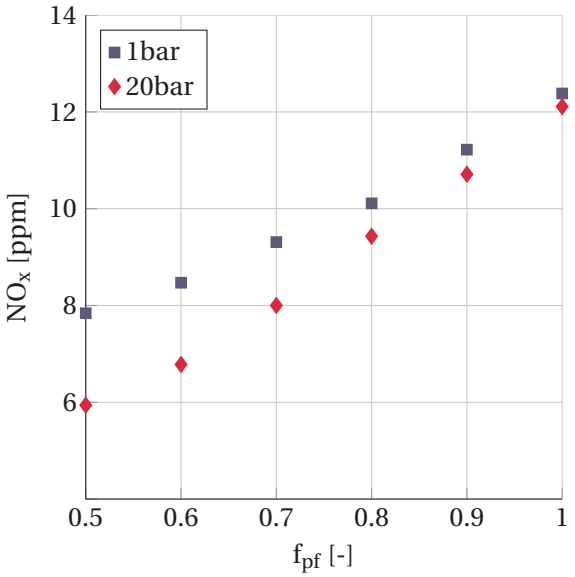

Figure 7.5: Influence of pre-flame mixing on overall NO_x-level after τ_{post}=5ms at 1 and 20bar.

comparison of figure 7.2 with figure 7.5 reveals that total NO_x at 20bar is dominated by post-flame NO_x-formation, although the selected post-flame residence time is very low (τ_{post}=5ms). Under atmospheric conditions, the contribution of post-flame NO_x-formation to total NO_x is significantly smaller and vanishes for low degrees of pre-flame mixing. If no pre-flame mixing is present, the NO_x-concentration in the post flame zone drops from 13.8ppm at the end of the heat release zone to 12.4ppm at the end of the post-flame reactor due to the dilution of the combustion products with cross flow material containing 4ppm NO_x.

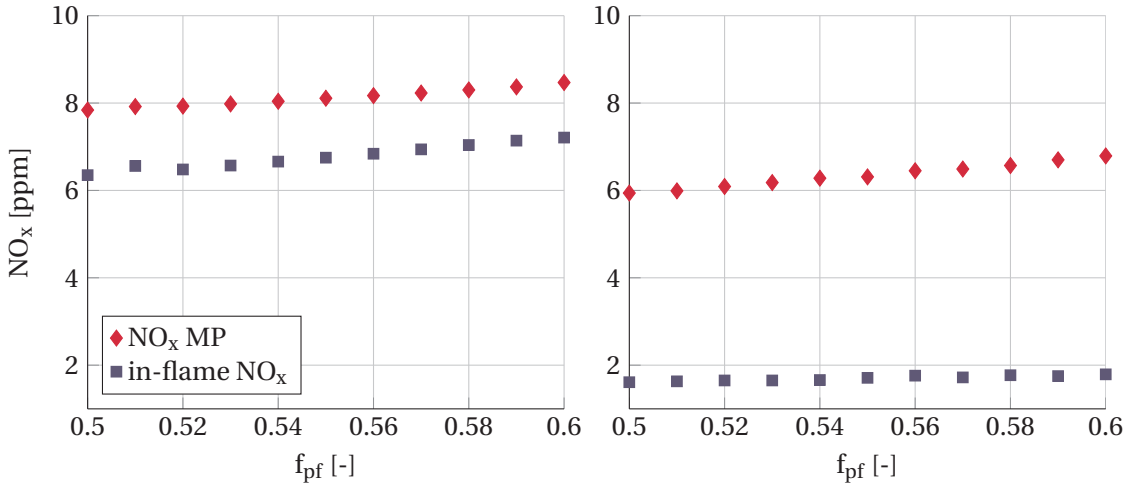

Figure 7.6: Comparison of total NO_x-concentrations with in-flame NO_x at 1bar (left) and 20bar (right) (lifted flame at equivalence ratio ϕ_J=0.66).

In order to further study the contribution of in-flame and post-flame NO_x-formation to total NO_x, the in-flame and the overall NO_x at the end of the post-flame reactor are plotted for pre-flame mixtures between $0.5 \leq f_{pf} \leq 0.6$, see figure 7.6. For the atmospheric case, the benefit of pre-flame mixing originates from the drop of in-flame NO_x-formation. In contrast, at 20bar, in-flame NO_x is almost constant in the pre-flame mixing range of $0.5 \leq f_{pf} \leq 0.6$ (see figure 7.2). Thus, the reduction of total NO_x is due to lower post-flame NO_x-formation, which depends on temperature and residence time. The adiabatic flame temperature for the pre-flame mixture of f_{pf}=0.6 is approximately 1920K. Although the resulting temperature overshoot with respect to the final temperature on the jet trajectory in the measurement plane (x/D=7.7) is not more than 30K, an increase of the NO_x-concentration by approximately 15% is computed between f_{pf}=0.5 and 0.6 (see figure 7.6 on the right).
In figure 7.7, the influences of temperature and residence time on NO_x-formation are shown for 20 bar. The NO_x-formation is cut by 50% if pre-flame mixing is increased from f_{pf}=1 to f_{pf}=0.5. The better pre-flame mixing reduces the adiabatic flame temperature of the burnt mixture by 140K, although the final temperature T_{MP}=1890K and mixture fraction f_{MP}=0.5 remain constant. In addition, the NO_x-concentrations are linearly increasing with post-flame residence time for a given degree of pre-flame mixing. Depending on pre-flame mixture f_{pf}, every additional

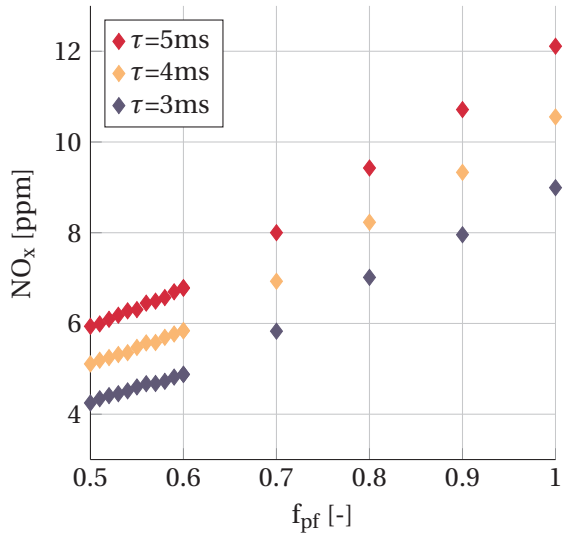

Figure 7.7: Influence of residence time and pre-flame mixture f_{pf} on overall NO_x-formation at 20bar (lifted flame at equivalence ratio ϕ_J=0.66).

millisecond of residence time increases the overall NO_x by 0.9 to 1.5ppm in the range of $0.5 \leq f_{pf} \leq 1$. This result reveals the residence time to be the important driver of NO_x-formation at 20bar.

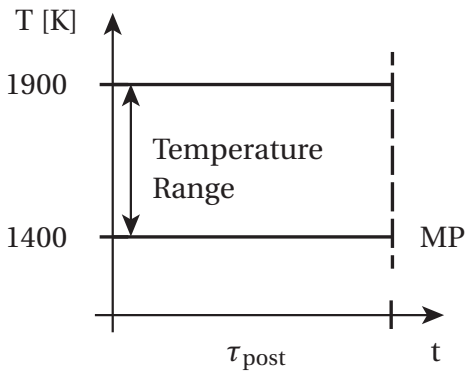

Figure 7.8: Scenario for the post-flame zone model with constant reactor temperature.

Finally, the influence of the temperature in the post-flame zone on NO_x-formation is studied. For this purpose, the scenario shown in figure 7.8 is employed. The product composition computed with the freely propagating flame model for a mixture with f_{pf}=0.5 is used as initial condition of the post-flame reactor. The temperature of the reactor is set to a constant value. No further entrainment is considered. Simulations with this reactor model are run in the temperature range between 1400 and 1900K. The post-flame NO_x is evaluated after a residence time of

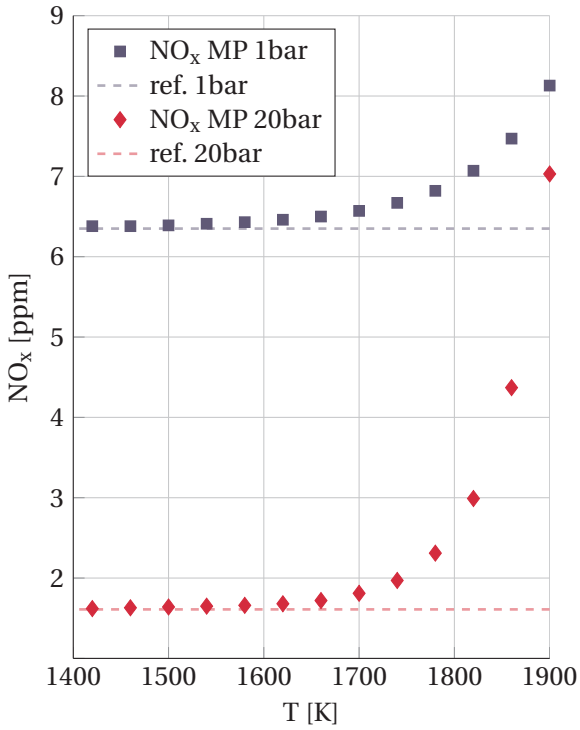

Figure 7.9: Temperature dependency of post-flame NO_x-formation at 1 and 20 bar and a residence time of τ_{post}=5ms (lifted flame at equivalence ratio ϕ_J=0.66).

τ_{post}=5ms. For both pressures, the typical exponential dependency of post-flame NO_x-formation on temperature according to Arrhenius' law is obtained (figure 7.9). In both cases, the asymptotic value of negligible post-flame NO_x-formation is reached below 1600K. As this limit is much lower than the temperatures in the jet region, post-flame NO_x-formation always contributes to the overall concentration levels of NO_x. In general, the dependencies of in-flame and post-flame NO_x-formation on pressure and temperature are in good agreement with literature studies [11, 23, 32, 129].

In conclusion, the sensitivity study has shown the pre-flame mixture f_{pf} to be the first dominant factor on overall NO_x-formation for both atmospheric conditions and combustion at 20bar. The dominant effect at high pressure is not the reduction of in-flame NO_x, but the lower adiabatic flame temperature T_{ad} of the burnt mixture, and the resulting shorter residence time in the hot environment. The exponential sensitivity of NO_x-formation on temperature was shown as well. The influence of temperature on post-flame NO_x-formation is of minor importance under atmospheric condition. The further reduction of over-

all NO_x with higher entrainment of cross flow material before ignition of the flame is caused by a reduction of in-flame NO_x-formation. Independent of pressure, the asymptotic value of negligible post-flame NO_x-formation is around 1600K. In general, the temperature effect can be reduced linearly by avoiding long residence time in hot environment, especially at 20bar.

7.5 NO_x Reduction Potential through Axial Staging

In chapter 5, a NO_x reduction potential analysis of staged combustion was conducted assuming perfect premixing of fuel and air (PP) in all combustion stages. The single stage combustion simulations provide values for the global NO_x-concentrations (see results in table 5.3 corresponding to a mass split ratio of 11%) and are taken as reference case in the following. The two different equivalence ratio of ϕ_J=0.66 and ϕ_J=0.77 in the jet are also considered in the network analysis of the lifted jet flame.

Table 7.1: Global NO_x of the single stage combustion for the perfectly premixed case (PP) and the partially premixed cases (F2 and F3). The NO_x-values are taken from the potential analysis of chapter 5.

			1bar	20bar		
ϕ_X	ϕ_J	ϕ_{tot}	PP	PP	F2	F3
0.5	0.66	0.5177	4.8ppm	3.4ppm	6.8ppm	10.2ppm
0.5	0.77	0.5296	6.1ppm	4.5ppm	9.0ppm	13.5ppm

However, as discussed in section 2.3.4, in reality significantly higher NO_x-emissions must be expected due to unmixedness of fuel and air in state of the art single stage combustors. Pilot stages and inevitable air admission through the flame tube increase the level of unmixedness further, and significantly raise the effective flame temperature above the turbine inlet temperature. In order to capture these effects in a simple manner, the single stage combustion data taken from table 5.3 are extended with two additional scenarios, assuming that the first stage produces twice (F2) and three times (F3) the minimum NO_x-value for perfect premixing, respectively. Based on this approach, we obtain the ref-

erence data for the three scenarios given in table 7.1. In the following study, the jet mixture of fuel and air is always perfectly premixed, although achieving perfect premixing in staged engine combustors may be difficult.
The following analysis is focused on the 20bar case with higher technical relevance. In the chemical potential analysis of chapter 5, the mass split ratio is 11% due to the large diameter of the injector of 100mm. This mass split ratio also determines together with the jet equivalence ratio ϕ_J the overall equivalence ratio ϕ_{tot}, see table 7.1. In contrast, the experiments with Karlovitz number scaling were conducted with a 15mm injector diameter. Although injection velocities are higher, this results in a lower mass flow in the secondary stage. The differences in mass split ratio must be taken into account by a factor of 7.9 in order to be able to compare the mean NO_x-values to the same overall equivalence ratio ϕ_{tot}. The area of jet influence is increased before the global NO_x-concentrations are calculated. The extracted mean NO_x-value (NO_x mean) can then be compared to the single stage combustion data given in table 7.1.
In the following reactor network model study of the lifted jet flame (see results in table 7.2 and 7.3), the same inlet conditions as in the experiment are applied to the high pressure simulations (f_{pf}=0.52, f_{MP}=0.5 see section 7.3). The only parameter that is not *per se* determined at 20bar conditions is the residence time after the flame τ_{post}. A total residence time of 6ms in the second stage was assumed to be typical for gas turbine conditions. The second scaling principle (Karlovitz number) results in almost identical jet velocities in the atmospheric test and the engine combustor. However, this high velocity could only be realized in the test rig with smaller diameter and at higher momentum ratio, as the conditions of the cross flow had to be kept constant. This lower momentum ratio results in a significantly lower penetration depth in the engine combustor with respect to the experiment. Furthermore, the velocity decay along the trajectory will be much lower under engine conditions, as the velocity of the cross flow and the jet are in the same range. Both effects result in lower residence times in the engine case. On the basis of these considerations, a reasonable range of the post-flame residence time between 3ms$<\tau_{post}<$5ms is selected for the simulations of the maximum NO_x-concentrations on the jet centerline.

Table 7.2: Results of network modeling (lifted flame at equivalence ratio ϕ_J=0.66). NO_x-values for the single stage combustion are taken from table 7.1.

ϕ_J=**0.66**	τ_{post} [ms]	NO_x min [ppm]	NO_x max [ppm]	NO_x mean [ppm]	single stage [ppm]
1bar	5	4.0	7.9	6.0	4.8
20bar	5	2.2	6.1	4.2	3.4
PP	4	2.2	5.2	3.7	
	3	2.2	4.4	3.3	
20bar	5	4.4	6.6	5.5	6.8
F2	4	4.4	5.6	5.1	
	3	4.4	4.9	4.7	
20bar	5	6.6	7.3	7.0	10.2
F3	4	6.6	6.5	6.5	
	3	6.6	5.6	6.1	

The results of the network model simulations of the lifted flame at equivalence ratio ϕ_J=0.66 and ϕ_J=0.77 are summarized in tables 7.2 and 7.3. Network modeling along the worst mixture trajectory delivers the maximum NO_x-values (NO_x max), the minimum NO_x-values are extracted from the simulations of the freely propagating flame model for the cross flow (NO_x min). Applying equation 7.2, the modeled NO_x-values are mapped to the channel using the field of the atmospheric measurements, see figure 6.23. An example is displayed in figure 7.10, obtained with the generic perfectly premixed first stage (PP) at a post-flame residence time of τ_{post}=3ms. The jet region needs to be scaled according to mass split ratio and therefore is expanded by a factor of 7.9. From this planar information the global mean NO_x-values is integrated (NO_x mean) and can now be compared with the single stage reference case (single stage). The results of the simulations at atmospheric and 20bar conditions of tables 7.2 and 7.3 are discussed in the following.
Staging at atmospheric pressure using lifted flame does not reduce the NO_x-values below the reference value for perfectly premixed single stage combustion. At 20bar the generic test case with perfectly premixed conditions shows a slight benefit in terms of NO_xs, however, only for the lowest residence time of τ_{post}=3ms. In this context, it is important to note that the level of the NO_x-concentrations in any case is much lower than

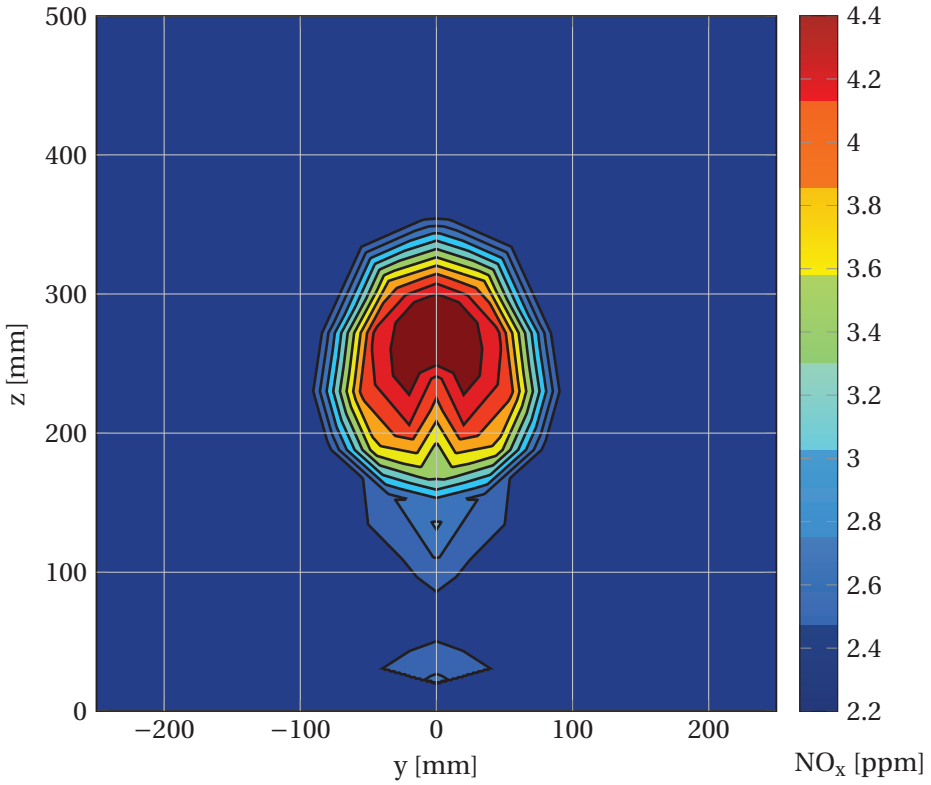

Figure 7.10: Computed NO_x-field at 20bar using the minimum and maximum values from table 7.2 and equation 7.2 for pressure scaling (lifted flame at equivalence ratio ϕ_J=0.66, τ_{post}=3ms).

NO_x-values of real engines operated with the same turbine inlet temperature, if perfect premixing of fuel and air (PP) is assumed. Taking into account the higher NO_x-concentrations of real engines with single stage combustors (cases F2 and F3) leads to a totally different picture. For both scenarios, significant NO_x benefits of staged combustion are identified: For F2, a reduction by 20% is predicted, and the reduction is 31% for F3 with a higher degree of unmixedness. Table 7.2 reveals that the NO_x reduction potential depends on the post-flame residence time in the second stage (see figure 7.11).
Finally, the reactor network model is applied to the lifted flame with a significantly higher jet equivalence ratio of ϕ_J=0.77, assuming the same pre-flame mixture as in the network model for the jet at equivalence ratio ϕ_J=0.66, i.e. f_{pf}=0.52 and f_{MP}=0.5. The higher jet equivalence ratio results in a higher maximum temperature in the measurement plane of 1970K for the mixture fraction f_{MP}=0.5. Table 7.3 summarizes the results for 20bar. The minimum NO_x-values of the cross flow (NO_x min) are

Table 7.3: Results of network modeling (lifted flame at equivalence ratio ϕ_J=0.77). NO_x-values for the single stage combustion are taken from table 7.1.

ϕ_J=**0.77**	τ_{post} [ms]	NO_x min [ppm]	NO_x max [ppm]	NO_x mean [ppm]	single stage [ppm]
20bar	3	2.2	12.0	7.2	4.5
PP	2	2.2	8.9	5.6	
	1	2.2	5.6	3.9	
20bar	5	4.4	18.8	11.7	9.0
F2	4	4.4	15.7	10.1	
	3	4.4	12.6	8.6	
20bar	5	6.6	19.5	13.2	13.5
F3	4	6.6	16.4	11.6	
	3	6.6	13.3	10.0	

taken from the free flame simulation at the equivalence ratio of ϕ_X=0.5 (see table 7.2).

Although the chemical potential analysis in chapter 5 showed a higher overall reduction potential, it is much harder to get a benefit for this operating point with higher equivalence ratio in the jet. The NO_x-value of 4.5ppm for the generic perfectly premixed (PP) single stage case can only be reduced with staged combustion, if the residence time in the post-flame region is unrealistically low. This effect is due to the sensitivity of the post-flame NO_x-formation on the jet temperature, which is higher for the lifted flame at equivalence ratio ϕ_J=0.77 compared to the lower equivalence ratio ϕ_J=0.66. A benefit of staging can only be obtained for high degrees of unmixedness of the first stage (see figure 7.11).

A combination of experimental results and chemical modeling was applied in order to transfer the experimental NO_x-results to 20bar gas turbine conditions. It was shown that the NO_x-concentration of the lifted flame at equivalence ratio ϕ_J=0.66 is in the range of the value of the single-stage simulation in chapter 5, assuming perfectly premixed conditions. A higher NO_x reduction potential exists, if the first stage produces higher NO_x due to unmixedness. In the typically range of double (F2) and three times (F3) higher NO_x-values of a real gas turbine combustor, a NO_x reduction potential of up to 31% is revealed (see blue squares in figure 7.11). For the operating point of the lifted flame at

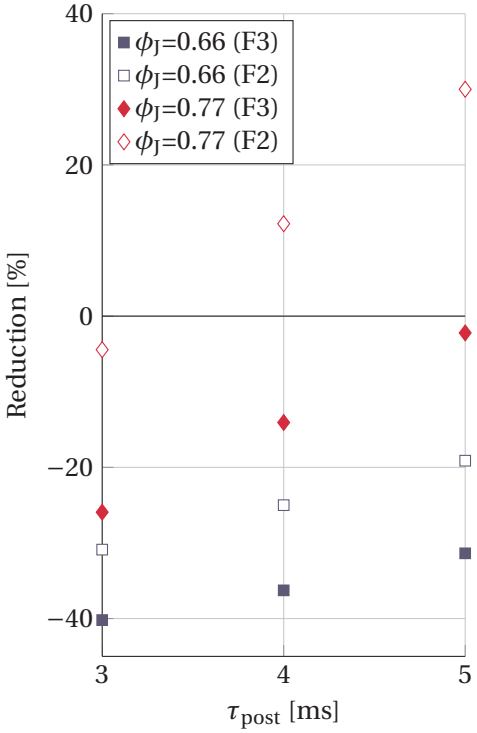

Figure 7.11: NO_X reduction potential at 20bar of the lifted flame at equivalence ratio ϕ_J=0.66 and ϕ_J=0.77 with unmixedness (F2 and F3).

the equivalence ratio of ϕ_J=0.77 of the jet it is harder to achieve a NO_x-benefit as the temperature at the same mixture is higher (see red diamonds in figure 7.11). In the temperature range between 1890K and 1970K at the jet equivalence ratio of ϕ_J=0.66 and 0.77, respectively, this is the major NO_x-driver at 20bar.

8 Summary and Conclusions

Nitrous oxides (NO_x) are air pollutant emissions causing smog and acid rain. The objective of the study at hand is the analysis of the potential of axially staged combustion for the reduction of overall NO_x-emissions in stationary gas turbines. The axially staged combustion chamber consists of a first stage of conventional burner design, and fuel-air jets injected into the hot exhaust of the first combustion zone.

In the first step, the potential of NO_x-reduction is investigated by simplified chemical models, and assuming perfect premixing of fuel and air in both the jet and the cross flow. Two asymptotic cases of no and perfect mixing of jet and cross flow material are considered as worst and best case, respectively. The potential study shows that staged combustion can lead to lower NO_x, if perfect mixing of jet and cross flow is achieved. If mixing between jet and cross flow is low, staged combustion will lead to higher NO_x-concentrations than single stage combustion at the same overall equivalence ratio. Under the assumption of perfect mixing, the reduction potential of a jet at the equivalence ratio of ϕ_J=0.77 is higher compared to a jet at the equivalence ratio of ϕ_J=0.66.

Atmospheric combustion experiments are performed on a large-scale test rig. The dependency between the mixture and the NO_x-field of anchored flames is experimentally studied at high spatial resolution. For this purpose, a laser-optical measurement technique is developed allowing quantitative analysis of the instantaneous and mean mixture fields. It is revealed that downstream of the secondary combustion zone local mixture fraction and NO_x-concentration are closely linked to each other. These results show that dilution of the jet material with combustion products is the key to the exploitation of the NO_x reduction potential of staged combustion. The temporal fluctuations of the mixture fractions in the shear layers of the reacting jet in hot cross flow also have an influence on NO_x-formation. This behavior is also detectable in the comparison of the normalized distribution of the NO_x and mixture fraction profiles a few jet diameters downstream of the jet injection.

Of high technical relevance are lifted flames in the second stage as mixing of jet and cross flow material prior to ignition is present. The exploitation of the NO_x reduction potential of the lifted flame is investigated by a combined approach of experiments and chemical reactor network modeling. A more sophisticated chemical network model is developed, taking into account pre-flame and post-flame mixing. After validation of the model by experimental data of the lifted flame, the same model is used in a sensitivity study on NO_x-formation at 1bar and 20bar. The network model is applied to study influences of pre-flame and post-flame mixing as well as post-flame residence time and temperature on NO_x-formation in the reacting jet. Achieving a high degree of pre-flame mixing is essential for the NO_x-reduction of axial staging requiring large lift-off heights of the flame in the second stage. The dominating effect at engine pressure is the drop of flame temperature with pre-flame mixing and the resulting shorter residence time in the hot environment. In contrast, the reduction of in-flame NO_x is of minor relevance. This dependency is qualitatively different at atmospheric pressure. At atmospheric pressure, the reduction of in-flame NO_x-formation is the dominant effect. As expected, the second parameter influencing the NO_x-reduction of axial staging is the post-flame residence time in the jet, which should be selected as short as possible.
Finally, the technical relevant case of higher NO_x-emissions of real gas turbine combustors compared to premixed laminar calculations are considered. The higher NO_x-levels originate from unmixedness of air and fuel, and air admission along the combustor liner. Two additional scenarios taking into account twice to three times higher NO_x-concentrations compared to a hypothetical perfectly mixed combustor are considered. The real benefit of axially staged combustion becomes visible, if a realistic level of NO_x in the first stage is considered. Reactor modeling indicates a NO_x reduction potential of up to one third for realistic degrees of unmixedness. However, if the difference of the equivalence ratios of both stages is selected too large, the benefit of axially staged combustion vanishes. The optimum equivalence ratio difference between both stages thus depends on the quality of the first stage with respect to NO_x-formation.

A Additional Experimental Results

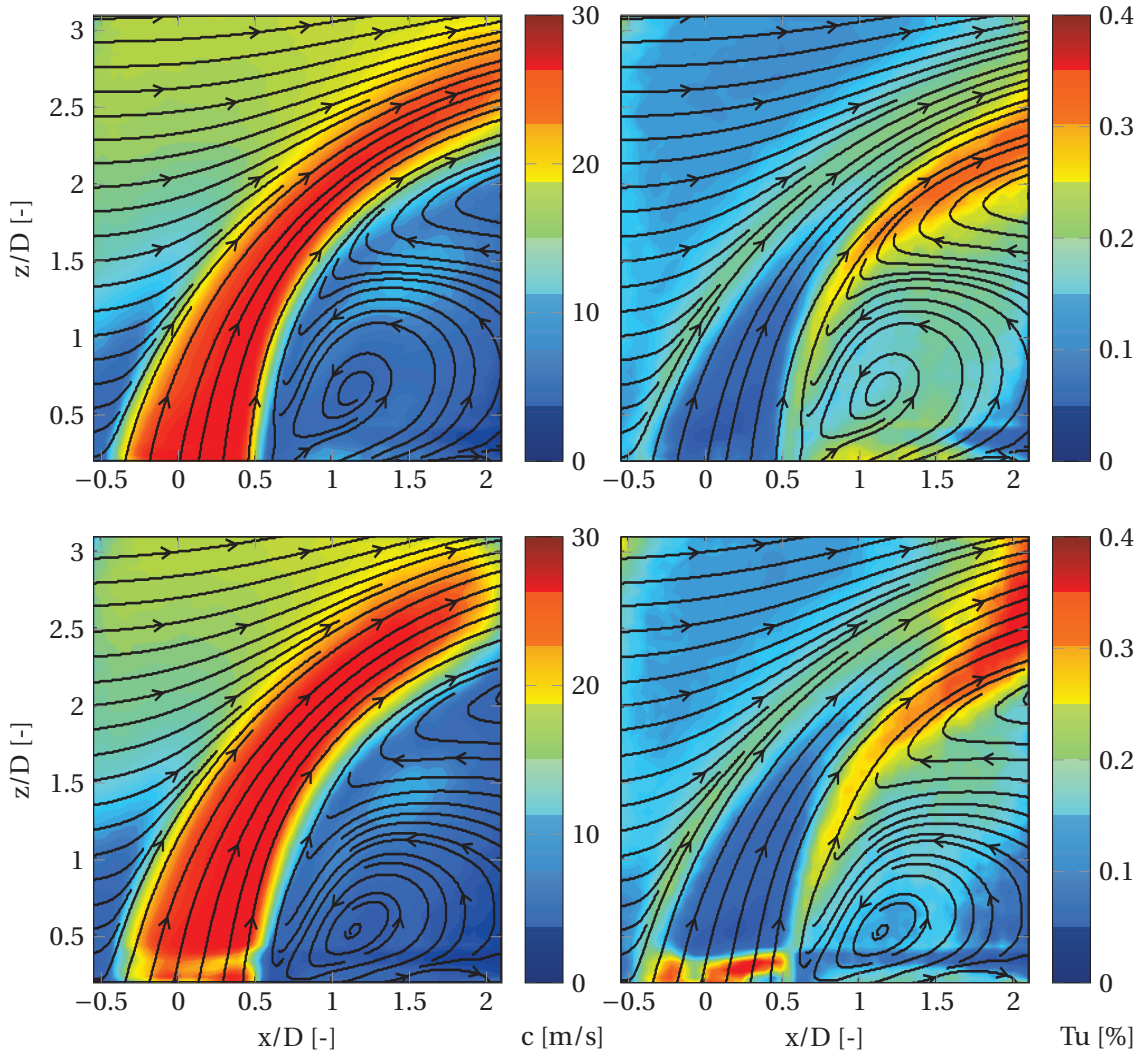

Figure A.1: Mean velocity field (left) and turbulence intensity (right) of the reacting jet at momentum ratio J=6 and jet equivalence ratio ϕ_J=0.5 (top) and 0.66 (bottom).

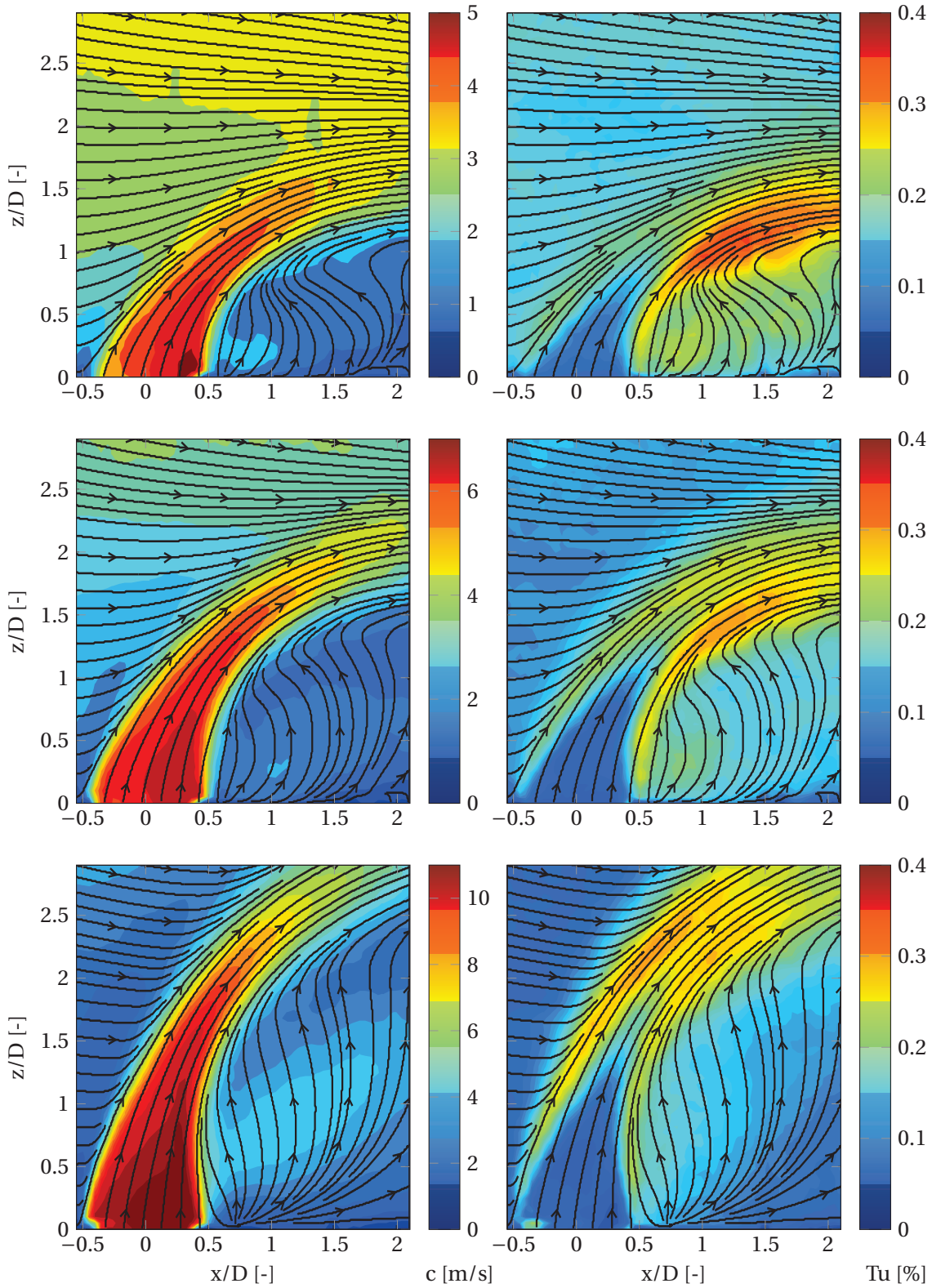

Figure A.2: Mean velocity field (left) and turbulence intensity (right) of the non-reacting jet at momentum ratios J=3 (top), 6 (center) and 15 (bottom).

Bibliography

[1] ABB, 1996. *Advance Optima - Systembeschreibung*.

[2] Adachi, S., Iwamoto, A., Hayashi, S., Yamada, H., and Kaneko, S., 2007. "Emissions in Combustion of Lean Methane-Air and Biomass-Air Mixtures Supported by Primary Hot Burned Gas in a Multi-Stage Gas Turbine Combustor". *Proceedings of the Combustion Institute,* ***31***, pp. 3131–3138.

[3] Ahrens, D., Kolb, M., Hirsch, C., and Sattelmayer, T., 2014. "NO_x Formation in a Reacting Premixed Jet in Hot Cross Flow". In Proceedings of ASME Turbo Expo 2014, GT2014-26139.

[4] Aida, N., Nishijima, T., Hayashi, S., Yamada, H., and Kawakami, T., 2005. "Combustion of Lean Prevaporized Fuel-Air Mixtures Mixed with Hot Burned Gas for Low-NO_x Emissions over an Extended Range of Fuel-Air Ratios". *Proceedings of the Combustion Institute,* ***30***, pp. 2885–2892.

[5] Aida, N., Nishijima, T., Yamada, H., Hayashi, S., and Kawakami, T., 2003. "Injection of Lean Mixtures into Hot Burned Gas for Maintaing Low-NO_x Emissions over an Extended Range of Fuel-Air Ratios in Prevaporized Combustion". In Proceedings of the International Gas Turbine Congress 2003, TS-142.

[6] Akbari, A., Hill, S., MCDonell, V., and Samuelsen, S., 2011. "Experimental and Computational Analyses of Methane and Hydrogen Mixing in a Model Premixer". *Journal of Engineering for Gas Turbines and Power,* ***133***(10), pp. 1–11.

[7] Andrews, G., Bradley, D., and Lwakabamba, S., 1975. "Turbulence and Turbulent Flame Propagation - a Critical Appraisal". *Combustion and Flame,* ***24***, pp. 285–304.

[8] Baur, A., 2013. "Bestimmung der Mischung in einem reagierenden Jet in Hot Crossflow mit Hilfe laserunterstützter Messmethode". Master's thesis, Lehrstuhl für Thermodynamik, Technische Universität München.

[9] Berrocal, E., Kristensson, E., Richter, M., Linne, M., and Alden, M., 2008. "Application of Structured Illumination for Multiple Scattering Suppression in Planar Laser Imaging of Dense Sprays". *Optics Express,* ***16***(22), pp. 17870–17881.

[10] Bhargava, A., Kendrick, D., Colket, M., and Sowa, W., 2000. "Pressure Effect on NO_x and CO Emissions in Industrial Gas Turbines". In Proceedings of ASME Turbo Expo 2000, GT2000-0097.

[11] Biagioli, F., and Güthe, F., 2007. "Effect of Pressure and Fuel-Air Unmixedness on NO_x Emissions from Industrial Gas Turbine Burners". *Combustion and Flame,* ***151***(1-2), pp. 274–288.

[12] Borghi, R., 1985. "On the Structure and Morphology of Turbulent Premixed Flames". In *Recent Advances in the Aerospace Sciences*, C. Casci and C. Bruno, eds. Springer US, pp. 117–138. In Honor of Luigi Crocco on His 75th Birthday.

[13] Bowman, C., 1971. "Investigation of Nitric Oxide Formation Kinetics in Combustion Process: The Hydrogen-Oxygen-Nitrogen Reaction". *Combustion Science and Technology,* ***3***(1), pp. 37–45.

[14] Bowman, C., 1992. "Control of Combustion-Generated Nitrogen Oxide Emissions: Technology Driven by Regulation". *Symposium (International) on Combustion,* ***24***, pp. 859–878.

[15] Bowman, C., Hanson, R., Davidson, D., (Jr.), W. G., Lissianski, V., Smith, G., Golden, D., Frenklach, M., and Goldenberg, M., 2014. http://www.me.berkeley.edu/gri_mech/.

[16] Bozzelli, J., and Dean, A., 1995. "O + NNH: A Possible New Route for NO_x Formation in Flames". *International Journal of Chemical Kinetics,* ***27***(11), November, pp. 1097–1109.

[17] Broadwell, J., and Breidenthal, R., 1984. "Structure and Mixing of a Transverse Jet in Incompressible Flow". *Journal of Fluid Mechanics,* ***148***, pp. 405–412.

[18] Brückner-Kalb, J., 2008. "Sub-ppm-NO_x-Verbrennungsverfahren für Gasturbinen". PhD thesis, Lehrstuhl für Thermodynamik, Technische Universität München.

[19] Cantera Documentation, 2014. http://cantera.github.io/docs/-sphinx/html/index.html, February.

[20] Cardenas, C., Denev, J., Suntz, R., and Bockhorn, H., 2012. "Study of Parameters and Entrainment of a Jet in Cross-Flow Arrangement with Transition at Two Low Reynolds Numbers". *Experiments in Fluids,* ***53***(4), pp. 965–987.

[21] Cardenas, C., Sedlmaier, J., Zarzalis, N., Valdes, R., and Krebs, W., 2011. "Measurement of a Benchmarking Jet in Crossflow Configuration Under Highly Turbulent Conditions". In Proceedings of ASME Turbo Expo 2011, GT2011-45262.

[22] Coda Zabetta, E., Kilpinen, P., Hupa, M., Stahl, K., Leppälahti, J., Cannon, M., and Nieminen, J., 2000. "Kinetic Modeling Study on the Potential of Staged Combustion in Gas Turbines for the Reduction of Nitrogen Oxide Emissions from Biomass IGCC Plants". *Energy & Fuels,* ***14***(4), pp. 751–761.

[23] Correa, S., 1993. "A Review of NO_x Formation Under Gas-Turbine Combustion Conditions". *Combustion Science and Technology,* ***87***(1-6), pp. 329–362.

[24] Cortelezzi, L., and Karagozian, A., 2001. "On the Formation of the Counter-Rotating Vortex Pair in Transverse Jets". *Journal of Fluid Mechanics,* ***446***, pp. 347–373.

[25] Damköhler, G., 1940. "Der Einfluss der Turbulenz auf die Flammengeschwindigkeit in Gasgemischen". *Zeitschrift für Elektrochemie und angewandte physikalische Chemie,* ***46***(11), pp. 601–626.

[26] Danckwerts, P., 1952. "The Definition and Measurement of Some Characteristics of Mixtures". *Applied Scientific Research, Section A,* ***3***(4), pp. 279–296.

[27] Davis, L., and Black, S., 2000. Dry Low NO_x Combustion Systems for Heavy-Duty Gas Turbines. Tech. rep., GE Power Systems.

[28] Dederichs, S., Habisreuther, P., Zarzalis, N., Beck, C., Krebs, W., and Prade, B., 2013. "Assessment of a Gas Turbine NO_x Reduction Potential Based on a Spatiotemporal Unmixedness Parameter". In Proceedings of ASME Turbo Expo 2013, GT2013-94404.

[29] Denev, J., Fröhlich, J., and Bockhorn, H., 2007. "Direct Numerical Simulation of a Transitional Jet in Crossflow with Mixing and Chemical Reactions". In Proceedings of the 5th Int. Symp. on Turbulence and Shear Flow Phenomena, TU-Munich, Garching, Germany, August 27-29, R. Friedrich, N. Adams, J. Eaton, J. Humphrey, N. Kasagi, and M. Leschziner, eds., Vol. 3, pp. 1243–1248.

[30] Denev, J., Fröhlich, J., and Bockhorn, H., 2009. "Large Eddy Simulation of a Swirling Transverse Jet into a Crossflow with Investigation of Scalar Transport". *Physics of Fluids,* ***21***(1), pp. 1–21.

[31] Döbbeling, K., Hellat, J., and Koch, H., 2007. "25 Years of BBC/ABB/Alstom Lean Premixed Combustion Technologies". *Journal of Engineering for Gas Turbines and Power,* ***129***(1), pp. 2–12.

[32] Drake, M., and Blint, R., 1991. "Calculations of NO_x Formation Pathways in Propagating Laminar, High Pressure Premixed CH_4/Air Flames". *Combustion Science and Technology,* ***75***(4-6), pp. 261–285.

[33] Eckbreth, A., 1996. *Laser Diagnostics for Combustion Temperature and Species*, second ed., Vol. 3 of *Combustion Science & Technology Book Series*. Gordon and Breach Publisher.

[34] ECO PHYSICS, 1997. *CLD 700 EL ht Manual*.

[35] Fearn, R., and Weston, R., 1974. "Vorticity Associated with a Jet in a Cross Flow". *AIAA Journal,* ***12***(12), pp. 1666–1671.

[36] Feitelberg, A., and Lacey, M., 1998. "The GE Rich-Quench-Lean Gas Turbine Combustor". *Journal of Engineering for Gas Turbines and Power,* ***120***(3), pp. 502–508.

[37] Fenimore, C., 1971. "Formation of Nitric Oxide in Premixed Hydrocarbon Flames". *Symposium (International) on Combustion,* ***13***, pp. 373–380.

[38] Fiorina, B., Baron, R., Gicquel, O., Thevenin, D., Carpentier, S., and Darabika, N., 2003. "Modelling Non-Adiabatic Partially Premixed Flames Using Flame-Prolongation of ILDM". *Combustion Theory and Modelling,* ***7***, pp. 449–470.

[39] Fleck, J., Griebel, P., Sadanandan, R., Steinberg, A., Stöhr, M., Aigner, M., and Ciani, A., 2010. "Characterization of a Generic, Fuel Flexible Reheat Combustor". In The Future of Gas Turbine Technology, 5th International Conference.

[40] Fleck, J., Griebel, P., Steinberg, A., Stöhr, M., Aigner, M., and Ciani, A., 2012. "Autoignition Limits of Hydrogen at Relevant Reheat Combustor Operating Conditions". *Journal of Engineering for Gas Turbines and Power,* ***134***(4), pp. 1–8.

[41] Fric, T., 1993. "Effects of Fuel-Air Unmixedness on NO_x Emissions". *Journal of Propulsion and Power,* ***9***(5), pp. 708–713.

[42] Fric, T., and Roshko, A., 1994. "Vortical Structure in the Wake of a Transverse Jet". *Journal of Fluid Mechanics,* ***279***, pp. 1–47.

[43] Galeazzo, F., Prathap, C., Kern, M., Habisreuther, P., and Zarzalis, N., 2012. "Investigation of a Flame Anchored in Crossflow Stream of Vitiated Air at Elevated Pressures". In Proceedings of ASME Turbo Expo 2012, GT2012-69632.

[44] Glassman, I., and Yetter, R., 2008. *Combustion*, fourth ed. Elsevier.

[45] Goodwin, D., Malaya, N., Moffat, H., and Speth, R., 2003. "Cantera: An Object-Oriented Software Toolkit for Chemical Kinetics, Thermodynamics, and Transport Processes". In Chemical Vapor Desposition XVI and EUROCVD, Vol. 14, pp. 2003–2008.

[46] Güthe, F., Hellat, J., and Flohr, P., 2009. "The Reheat Concept: The Proven Pathway to Ultralow Emissions and high Efficiency and Flexibility". *Journal of Engineering for Gas Turbines and Power,* ***131***(2), pp. 1–7.

[47] Gutmark, E., Ibrahim, I., and Murugappan, S., 2008. "Circular and Noncircular Subsonic Jets in Cross Flow". *Physics of Fluids,* ***20***(7), pp. 1–18.

[48] Habisreuther, P., Galeazzo, F., Prathap, C., and Zarzalis, N., 2013. "Structure of Laminar Premixed Flames of Methane Near the Auto-Ignition Limit". *Combustion and Flame,* ***160***(12), pp. 2770–2782.

[49] Han, D., Mungal, M., Zamansky, V., and Tyson, T., 1999. "Prediction of NO_x Control by Basic and Advanced Gas Reburning Using the Two-Stage Lagrangian Model". *Combustion and Flame,* ***119***(4), pp. 483–493.

[50] Harrington, J., Smith, G., Berg, P., Noble, A., Jeffries, J., and Crosley, D., 1996. "Evidence for a New NO Production Mechanism in Flames". *Symposium (International) on Combustion,* ***26***, pp. 2133–2138.

[51] Hasselbrink, E., and Mungal, M., 2001. "Transverse Jets and Jet Flames. Part 1. Scaling Laws for Strong Transverse Jets". *Journal of Fluid Mechanics,* ***443***, pp. 1–25.

[52] Hasselbrink, E., and Mungal, M., 2001. "Transverse Jets and Jet Flames. Part 2. Velocity and OH Field Imaging". *Journal of Fluid Mechanics,* ***443***, pp. 27–68.

[53] Haven, B., and Kurosaka, M., 1997. "Kidney and Anti-Kidney Vortices in Crossflow Jets". *Journal of Fluid Mechanics,* ***352***, pp. 27–64.

[54] Hayashi, S., and Yamada, H., 2000. "NO_x Emissions in Combustion of Lean Premixed Mixtures Injected into Hot Burned Gas". *Proceedings of the Combustion Institute,* ***28***, pp. 2443–2449.

[55] Hayashi, S., Yamada, H., and Makida, M., 2005. "Extending Low-NO_x Operating Range of a Lean Premixed-Prevaporized Gas Turbine Combustor by Reacting of Secondary Mixtures Injected into Primary Stage Burned Gas". *Proceedings of the Combustion Institute,* ***30***, pp. 2903–2911.

[56] Hayhurst, A., and Hutchinson, E., 1998. "Evidence for a New Way of Producing NO via NNH in Fuel-Rich Flames at Atmospheric Pressure". *Combustion and Flame,* ***114***, July, pp. 274–279.

[57] Hayhurst, A., and Vince, I., 1980. "Nitric Oxide Formation from N_2 in Flames: The Importance of Prompt NO". *Progress in Energy and Combustion Science,* ***6***(1), pp. 35–51.

[58] Heravi, H., Azarinfar, A., Kwon, S., and Syred, N., 2007. "Determination of Laminar Flame Thickness and Burning Velocity of Methane-Air Mixture". In Third European Combustion Meeting.

[59] Hermsmeyer, H., Prade, B., Gruschka, U., Schmitz, U., Hoffmann, S., and Krebs, W., 2002. "V64.3A Gas Turbine Natural Gas Burner Development". In Proceedings of ASME Turbo Expo 2002, GT2002-30106.

[60] Hill, S., and Smoot, L., 2000. "Modeling of Nitrogen Oxides Formation and Destruction in Combustion Systems". *Progress in Energy and Combustion Science,* ***26***, pp. 417–458.

[61] Hjelmfelt, A., and Mockros, L., 1966. "Motion of Discrete Particles in a Turbulent Fluid". *Applied Scientific Research,* ***16***, pp. 149–161.

[62] Hoferichter, V., 2013. "Pollutant Formation in a Reacting Jet in Hot Cross Flow". Master's thesis, Lehrstuhl für Thermodynamik, Technische Universität München.

[63] Holdeman, J., 1972. Correlation for the Temperature Profiles in the Plane of Symmetry Downstream of a Jet Injected Normal to a Crossflow. Tech. Rep. TN D-6966, NASA.

[64] Holdeman, J., Smith, T., Clisset, J., and Lear, W., 2005. A Spreadsheet for the Mixing of a Row of Jets with a Confined Crossflow. Tech. Rep. TM–2005-213137, NASA.

[65] Holdeman, J., and Walker, R., 1977. "Mixing of a Row of Jets with a Confined Crossflow". *AIAA Journal,* ***15***(2), pp. 243–249.

[66] Huang, J., Hill, P., Bushe, W., and Munshi, S., 2004. "Shock-Tube Study of Methane Ignition Under Engine-Relevant Conditions: Ex-

periments and Modeling ". *Combustion and Flame,* ***136***, pp. 25 – 42.

[67] Irwin, J., and Williams, M., 1988. "Acid Rain: Chemistry and Transport". *Environmental Pollution,* ***50***, pp. 29–59.

[68] Ivanova, E., Noll, B., and Aigner, M., 2012. "A Numerical Study on the Turbulent Schmidt Numbers in a Jet in Crossflow". In Proceedings of ASME Turbo Expo 2012, GT2012-69294.

[69] Kamotani, Y., and Greber, I., 1972. "Experiments on a Turbulent Jet in a Cross Flow". *AIAA Journal,* ***10***(11), pp. 1425–1429.

[70] Kamotani, Y., and Greber, I., 1974. Experiments on Confined Turbulent Jets in Cross Flow. Tech. Rep. CR-2392, NASA.

[71] Karagozian, A., 1986. "An Analytic Model for the Vorticity Associated with a Transverse Jet". *AIAA Journal,* ***24***(3), pp. 429–436.

[72] Karagozian, A., 2010. "Transverse Jets and Their Control". *Progress in Energy and Combustion Science,* ***36***(5), pp. 531–553.

[73] Kayode Coker, A., 2001. *Modeling of Chemical Kinetics and Reactor Design*. Gulf Professional Publishing.

[74] Kee, R., Grcar, J., Smooke, M., Miller, J., and Meeks, E., 1998. PREMIX: A FORTRAN Programm for Modeling Steady Laminar One-Dimensional Premixed Flames. Tech. rep., Sandia National Laboratories.

[75] Kelso, R., Lim, T., and Perry, A., 1996. "An Experimental Study of Round Jets in Cross-Flow". *Journal of Fluid Mechanics,* ***306***, pp. 111–144.

[76] Kelso, R., and Smits, A., 1995. "Horseshoe Vortex Systems Resulting from the Interaction Between a Laminar Boundary Layer and a Transverse Jet". *Physics of Fluids,* ***7***(1), pp. 153–158.

[77] Kolb, M., Ahrens, D., Hirsch, C., and Sattelmayer, T., 2013. "Quantification of Mixture of a Reacting Jet in Hot Cross Flow Using Mie Scattering". In Fachtagung "Lasermethoden in der Strömungsmesstechnik".

[78] Kolb, M., Ahrens, D., Hirsch, C., and Sattelmayer, T., 2015. "A Model for Predicting the Lift-Off Height of Premixed Jets in Vitiated Cross Flow". In Proceedings of ASME Turbo Expo 2015, GT2015-42225.

[79] Kristensson, E., Araneo, L., Berrocal, E., Manin, J., Richter, M., Alden, M., and Linne, M., 2011. "Analysis of Multiple Scattering Suppresion Using Structured Laser Illumination Planar Imaging in Scattering and Fluorescing Media". *Optics Express,* ***19***(14), pp. 13647–13663.

[80] Kröner, M., 2003. "Einfluss lokaler Löschvorgänge auf den Flammenrückschlag durch verbrennungsinduziertes Wirbelaufplatzen". PhD thesis, Lehrstuhl für Thermodynamik, Technische Universität München.

[81] Krothapalli, A., Lourenco, L., and Buchlin, J. M., 1990. "Separated Flow Upstream of a Jet in a Crossflow". *AIAA Journal,* ***28***(3), pp. 414–420.

[82] Lacarelle, A., Göke, S., and Paschereit, C. O., 2010. "A Quantitative Link Between Cold-Flow Scalar Unmixedness and NO_x Emissions in a Conical Premixed Burner". In Proceedings of ASME Turbo Expo 2010, GT2010-23132.

[83] Lamont, W., Roa, M., and Lucht, R., 2014. "Application of Artificial Neural Networks for the Prediction of Pollutant Emissions and Outlet Temperature in a Fuel-Staged Gas Turbine Combustion Rig". In Proceedings of ASME Turbo Expo 2014, GT2014-25030.

[84] Lamont, W., Roa, M., Meyer, S., and Lucht, R., 2012. "Emission Measurements and CH* Chemiluminescence of a Staged Combustion Rig for Stationary Gas Turbine Applications". *Journal of Engineering for Gas Turbines and Power,* ***134***(8), pp. 1–7.

[85] Lauer, M., 2011. "Determination of the Heat Release Distribution in Turbulent Flames by Chemiluminescence Imaging". PhD thesis, Lehrstuhl für Thermodynamik, Technische Universität München.

[86] Lechner, C., and Seume, J., eds., 2010. *Stationäre Gasturbinen.* Springer.

[87] Leonard, G., and Stegmaier, J., 1994. "Development of an Aeroderivative Gas Turbine Dry Low Emissions Combustion System". *Journal of Engineering for Gas Turbines and Power,* ***115***(3), p. 5.

[88] Lim, T., New, T., and Luo, S., 2001. "On the Development of Large-Scale Structures of a Jet Normal to a Cross Flow". *Physics of Fluids,* ***13***(3), pp. 770–775.

[89] Liscinsky, D., True, B., and Holdeman, J., 1993. "Experimental Investigation of Crossflow Jet Mixing in a Rectangular Duct". In 29th Joint Propulsion Conference and Exhibit.

[90] Liscinsky, D., True, B., and Holdeman, J., 1995. Effects of Initial Conditions on a Single Jet in Crossflow. Tech. Rep. NASA-TM-107002, AIAA-95-2998, NASA.

[91] Liscinsky, D., True, B., and Holdeman, J., 1996. "Crossflow Mixing of Noncircular Jets". *Journal of Propulsion and Power,* ***12***(2), pp. 225–230.

[92] Mahesh, K., 2013. "The Interaction of Jets with Crossflow". *Annual Review of Fluid Mechanics,* ***45***(1), pp. 379–407.

[93] Major, B., and Powers, B., 1999. Cost Analysis of NO_x Control Alternatives for Stationary Gas Turbines. Tech. rep., ONSITE SYCOM Energy Corporation.

[94] Margason, R., 1993. "Fifty Years of Jet in Cross Flow Research". In Computational and Experimental Assessment of Jets in Cross Flow - AGARD Conference Proceedings, AGARD CP-534, North Atlantic Treaty Organization, pp. 21–61.

[95] Mason, J., 1994. "Acid Rain: Its Effects on Lakes, Streams and Fish". *Renewable Energy,* ***5***(Part II), pp. 1247–1253.

[96] McManus, K., Poinsot, T., and Candel, S., 1993. "A Review of Active Control of Combustion Instabilities". *Progress in Energy and Combustion Science,* ***19***(1), pp. 1–29.

[97] Melling, A., 1997. "Tracer Particles and Seeding for Particle Image Velocimetry". *Measurement Science and Technology,* ***8***, pp. 1406–1416.

[98] Menz, F., and Seip, H., 2004. "Acid Rain in Europe and the United States: An Update". *Environmental Science & Policy,* ***7***(4), pp. 253–265.

[99] Metcalfe, W., Burke, S., Ahmed, S., and Curran, H., 2013. "A Hierarchical and Comparative Kinetic Modeling Study of C1 - C2 Hydrocarbon and Oxygenated Fuels". *International Journal of Chemical Kinetics,* ***45***(10), pp. 638–675.

[100] Meyer, K., Pedersen, J., and Özcan, O., 2007. "A Turbulent Jet in Crossflow Analysed with Proper Orthogonal Decomposition". *Journal of Fluid Mechanics,* ***583***, pp. 199–227.

[101] Miller, J., and Bowman, C., 1989. "Mechanism and Modeling of Nitrogen Chemistry in Combustion". *Progress in Energy and Combustion Science,* ***15***(4), pp. 287–338.

[102] Moussa, Z., Trischka, J., and Eskinazi, S., 1977. "The Near Field in the Mixing of a Round Jet With a Cross-Stream". *Journal of Fluid Mechanics,* ***80***(01), pp. 49–80.

[103] Müller, P., 2012. "Inbetriebnahme des GE LLI Verbrennungsversuchsstandes". Master's thesis, Lehrstuhl für Thermodynamik, Technische Universität München.

[104] Muppidi, S., and Mahesh, K., 2008. "Direct Numerical Simulation of Passive Scalar Transport in Transverse Jets". *Journal of Fluid Mechanics,* ***598***, pp. 335–360.

[105] Narayan, S., and Rajan, S., 98. "Superequilibrium O Concentrations and Prompt NO Formation in Laminar Premixed Methane-Air Flames". *Combustion Science and Technology,* ***139***, pp. 159–171.

[106] Naumann, C., Herzler, J., Griebel, P., Curran, H., Kéromnès, A., Metcalfe, W., and Goswami, M., 2012. Release of Final Best-to-Use Reaction Mechanism for Syngas Combustion Modeling. Tech.

rep., Deutsches Zentrum für Luft- und Raumfahrt e.V., National University Galway and Eindhoven University of Technology.

[107] New, T., Lim, T., and Luo, S., 2003. "Elliptic Jets in Cross-Flow". *Journal of Fluid Mechanics,* ***494***, 10, pp. 119–140.

[108] New, T., Lim, T., and Luo, S., 2006. "Effects of Jet Velocity Profiles on a Round Jet in Cross-Flow". *Experiments in Fluids,* ***40***(6), pp. 859–875.

[109] Norster, E., 1964. Second Report on Jet Penetration and Mixing Studies. Tech. rep., The College of Aeronautics Cranfield.

[110] Pernpeintner, M., Lauer, M., Hirsch, C., and Sattelmayer, T., 2011. "A Method to Obtain Planar Mixture Fraction Statistics in Turbulent Flows Seeded With Tracer Particles". In Proceedings of ASME Turbo Expo 2011, GT2011-46844.

[111] Peters, N., 1986. "Laminar Flamelet Concepts in Turbulent Combustion". *Symposium (International) on Combustion,* ***21***, pp. 1231 – 1250.

[112] Peters, N., 1994. Turbulente Brenngeschwindigkeit. Tech. rep., Abschlussbericht zum Forschungsvorhaben Pe 241/9-2.

[113] Peters, N., 1999. "The Turbulent Burning Velocity for Large-Scale and Small-Scale Turbulence". *Journal of Fluid Mechanics,* ***384***, pp. 107–132.

[114] Peters, N., 2004. *Turbulent Combustion*. Cambridge Monographs on Mechanics. Cambridge University Press.

[115] Petersen, E., Kalitan, D., Simmons, S., Bourque, G., Curran, H., and Simmie, J., 2007. "Methane/Propane Oxidation at High Pressures: Experimental and Detailed Chemical Kinetic Modeling ". *Proceedings of the Combustion Institute,* ***31***(1), pp. 447–454.

[116] PHOTRON EUROPE LIMITED, 2004. *FASTCAM-Ultima APX Hardware Manual*.

[117] Pope, S., 2008. *Turbulent Flows*, fifth ed. Cambridge University Press.

[118] Prathap, C., Galeazzo, F., Kasabov, P., Habisreuther, P., Zarzalis, N., Beck, C., Krebs, W., and Wegner, B., 2012. "Analysis of NO_x Formation in an Axially Staged Combustion System at Elevated Pressure Conditions". *Journal of Engineering for Gas Turbines and Power,* ***134***(3), pp. 1–8.

[119] Pratte, B., and Baines, W., 1967. "Profiles of the Round Turbulent Jet in a Cross Flow". *Journal of the Hydraulics Division,* ***93***(6), pp. 53–64.

[120] Prause, J., Noll, B., and Aigner, M., 2014. "Sensitivity Analysis of Auoignition Simulation at Gas Turbine Operating Conditions". In Proceedings of ASME Turbo Expo 2014, GT2014-25503.

[121] Prière, C., Gicquel, L., Kaufmann, P., Krebs, W., and Poinsot, T., 2004. "Large Eddy Simulation Predictions of Mixing Enhancement for Jets in Cross-Flows". *Journal of Turbulence*, pp. 1–24.

[122] Raffel, M., Willert, C., and Kompenhans, J., 1997. *Particle Image Velocimetry - A Practical Guide*. Springer.

[123] Ramsey, J., and Goldstein, R., 1970. Interaction of a Heated Jet with a Deflecting Stream. Tech. Rep. CR-72613, NASA.

[124] Richards, G., McMillian, M., Gemmen, R., Rogers, W., and Cully, S., 2001. "Issues for Low-Emission, Fuel-Flexible Power Systems". *Progress in Energy and Combustion Science,* ***27***(2), pp. 141–169.

[125] Ricou, F., and Spalding, D., 1961. "Measurements of Entrainment by Axisymmetrical Turbulent Jets". *Journal of Fluid Mechanics,* ***11***(1), pp. 21–32.

[126] Rizk, N., and Mongia, H., 1993. "Three-Dimensional NO_x Model for Rich/Lean Combustor". In 31st Aerospace Sciences Meeting & Exhibit.

[127] Roberts, P., and Webster, D., 2002. "Turbulent Diffusion". In *Environmental Fluid Mechanics - Theories and Applications*, H. Shen, A. Cheng, K.-H. Wang, M. Teng, and C. Liu, eds. American Society of Civil Engineers, pp. 7–45.

[128] Rokke, P., Hustad, J., Rokke, N., and Svendsgaard, O., 2003. "Technology Update on Gas Turbine Dual Fuel, Dry Low Emission Combustion Systems". In Proceedings of ASME Turbo Expo 2003, GT2003-38112.

[129] Rutar, T., and Malte, P., 2002. "NO_x Formation in High-Pressure Jet-Stirred Reactors With Significance to Lean-Premixed Combustion Turbines". *Journal of Engineering for Gas Turbines and Power,* ***124***(4), pp. 776–783.

[130] SAE INTERNATIONAL, AEROSPACE RECOMMENDED PRACTICE, 2013. *Procedure for the Calculation of Gaseous Emissions From Aircraft Turbine Engines*.

[131] Salewski, M., Stankovic, D., and Fuchs, L., 2008. "Mixing in Circular and Non-Circular Jets in Crossflow". *Flow, Turbulence and Combustion,* ***80***(2), pp. 255–283.

[132] Sattelmayer, T., Polifke, W., Winkler, D., and Döbbeling, K., 1998. "NO_x-Abatement Potential of Lean-Premixed GT Combustors". *Journal of Engineering for Gas Turbines and Power,* ***120***(1), pp. 48–59.

[133] Sautet, J., and Stepowski, D., 1994. "Single-Shot Laser Mie Scattering Measurements of the Scalar Profiles in the Near Field of Turbulent Jets with Variable Densities". *Experiments in Fluids,* ***16***(6), pp. 353–367.

[134] Schmitt, D., Kolb, M., Weinzierl, J., Hirsch, C., and Sattelmayer, T., 2013. "Ignition and Flame Stabilization of a Premixed Jet in Hot Cross Flow". In Proceedings of ASME Turbo Expo 2013, GT2013-94763.

[135] Smith, G., Golden, D., Frenklach, M., Moriarty, N., Eiteneer, B., Goldenberg, M., Bowman, C., Hanson, R., Song, S., (Jr.), W. G., Lissianski, V., and Qin, Z., 2014. http://www.me.berkeley.edu/gri_mech/.

[136] Smith, S., and Mungal, M., 1998. "Mixing, Structure and Scaling of the Jet in Crossflow". *Journal of Fluid Mechanics,* ***357***, pp. 83–122.

[137] Spadaccini, L., and Colket, M., 1994. "Ignition Delay Characteristics of Methane Fuels". *Progress in Energy and Combustion Science,* ***20***(5), pp. 431 – 460.

[138] Steinmetz, M., 2013. "Mixture Field Analysis of Reacting Jets in hot Cross Flow". Master's thesis, Lehrstuhl für Thermodynamik, Technische Universität München.

[139] Stepowski, D., and Cabot, G., 1988. "Laser Mie Scattering Measurement of Mean Mixture Fraction Density and Temperature by Conditional Seeding in a Turbulent Diffusion Flame". *Symposium (International) on Combustion,* ***22***, pp. 619–625.

[140] Streb, H., Prade, B. Hahner, T., and Hoffmann, S., 2001. "Advanced Burner Development for the VX4.3A Gas Turbines". In Proceedings of ASME Turbo Expo 2001, GT2001-0077.

[141] SWM SERVICES GMBH, 2012. *Erdgasqualität im Verteilungsnetz des Großraumes München*. http://www.swm.de/dms/swm/dokumente/schulen/downloads/erdgas-qualitaet.pdf, January.

[142] Tachibana, S., Zimmer, L., and Kazuo, S., 2004. "Flame Front Detection and Dynamics Using PIV in a Turbulent Premixed Flame". In 12th International Symposium on Applications of Laser Techniques to Fluid Mechanics.

[143] Tennekes, H., and Lumley, J., 1972. *A First Course in Turbulence*. The MIT Press.

[144] Turns, S., 2006. *An Introduction to Combustion - Concepts and Applications*. McGraw Hill.

[145] Vandervort, C., 2001. "9 ppm NO_x/CO Combustion System for "F" Class Industrial Gas Turbines". *Journal of Engineering for Gas Turbines and Power,* ***123***(2), pp. 317–321.

[146] Vogel, H., 1995. *Gerthsen Physik*, 18th ed. Springer Berlin.

[147] Voigt, P., 1999. "Entwicklung und Einsatz eines Laserlichtschnittverfahrens zur quantitativen Konzentrationsmessung bei Mischungsprozessen". PhD thesis, Institut für Antriebstechnik Köln.

[148] Walker, D., Diehl, L., Strauss, W., and Edse, R., 1969. Investigation of the Ignition Properties of Flowing Combustible Gas Mixtures. Tech. rep., Aeronautical and Astronautical Research Laboratory, The Ohio State University.

[149] Wegner, B., Huai, Y., and Sadiki, A., 2004. "Comparative Study of Turbulent Mixing in Jet in Cross-Flow Configurations Using LES". *International Journal of Heat and Fluid Flow,* ***25***(5), pp. 767–775.

[150] Westenberg, A., 1971. "Kinetics of NO and CO in Lean, Premixed Hydrocarbon-Air Flames". *Combustion Science and Technology,* ***4***, pp. 59–64.

[151] White, F., 2005. *Viscous Fluid Flow*, third ed. McGraw-Hill Mechanical Engineering.

[152] Wünning, J., and Wünning, J., 1997. "Flameless Oxidation to Reduce Thermal NO-Formation". *Progress in Energy and Combustion Science,* ***23***, pp. 81–94.

[153] Yamamoto, T., Shimodaira, K., Kurosawa, Y., and Nakamura, N., 2014. "Effects of Air Jets Through Combustor Liner Holes on Emissions of Lean Staged Combustor". In Proceedings of ASME Turbo Expo 2014, GT2014-25871.

[154] Yingjaroen, T., Pimpin, A., and Bunyajitradulya, A., 2006. "Evolution of Mixing Regions in Jet and Swirling Jet in Crossflow: An Experimental Study". In The 20th Conference of Mechanical Engineering Network of Thailand.

[155] Yuan, L., and Street, R., 1998. "Trajectory and Entrainment of a Round Jet in Crossflow". *Physics of Fluids,* ***10***(9), pp. 2323–2335.

[156] Yuan, L., Street, R., and Ferziger, J., 1999. "Large-Eddy Simulations of a Round Jet in Crossflow". *Journal of Fluid Mechanics,* ***379***, pp. 71–104.

[157] Zabetakis, M., 1965. Flammability Characteristics of Combustible Gases and Vapors. Bulletin 627, Bureau of Mines.

[158] Zeldovitch, J., 1946. "The Oxidation of Nitrogen in Combustion and Explosion". *Acta Physicochimica,* ***21***(1), pp. 577–628.